

**Effects of geophysical parameters on the seismic
expression of the Maghlaq Fault, Malta:
insights from outcrop-based 2D seismic modeling**

Ingvild Gabrielsen Andersen



Master Thesis in Basin and Reservoir Studies

Department of Earth Science

University of Bergen

June, 2020

Abstract

Faults are heterogenous zones comprising highly complex geometries, which can be studied in detail from field outcrops. The internal complexity of a fault zone is however difficult to interpret from seismic images, due to resolution and illumination limitations of the data. To improve the seismic interpretation of subsurface structures, synthetic seismic can be simulated from outcrop-derived geological models. Such seismic modeling reveals the potential seismic expression of structural and stratigraphic features observed in the field. In this study, a 2D Point-Spread Function based modeling approach is applied to investigate the seismic expression of the Maghlaq Fault, Malta, which is a carbonate-hosted normal fault zone comprising complex hanging wall geometries. Geological models of the fault zone are created based on both geological interpretations of virtual outcrop models of the hanging wall of the fault as well as conceptual extrapolations. The geological models are divided into lithostratigraphic units, which are further assigned realistic elastic properties (i.e. seismic velocities and density) in order to create reflectivity models. Pre-stack Depth Migration images are simulated from the seismic modeling, predicting the seismic characteristics of the Maghlaq Fault. The study further analyzes the effects of various geophysical survey parameters on the seismic images, by systematically varying each individual parameter, such as the dominant frequency, level of noise, angle of maximum illumination, incident angle and wavelet type.

The resulting 2D seismic sections generated in this study show that the seismic expression of the Maghlaq Fault differs to some extent for the four different geological models, due to the significant variation in hanging wall geometry of the four geological input models. Nevertheless, some consistent seismic characteristics are found in all seismic images, regardless of the variation in structural and stratigraphic input. Furthermore, the obtained results from the sensitivity analyses highlight the geophysical parameter dependency of both the detectability and the seismic expression of the fault zone. The dominant frequency, noise level and angle of maximum illumination are the parameters which have the greatest impact on the seismic images of the Maghlaq Fault zone. This thesis is a contribution to improve the understanding of seismic imaging of normal fault zones within carbonates, which hopefully can aid seismic interpretation of similar structures in the subsurface.

Acknowledgements

This thesis is part of my MSc degree in Basin and Reservoir Studies at the Department of Earth Science, University of Bergen, and was made possible with the guidance and feedback from several contributors. First and foremost, I would like to express my gratitude to my main supervisor, Atle Rotevatn, for valuable guidance and support the past two years. Thank you for always being encouraging and positive. I would also like to thank my co-supervisor, Isabelle Lecomte, for guidance in SeisRoX, as well as great discussions and constructive reviews of my thesis. Special thanks to my co-supervisor, Vilde Dimmen, for being an excellent field guide during our first week in Malta, for support in the computer lab and feedback on the thesis. In addition to Vilde, I would like to thank Isabel Edmundson, Maria Ordemann, David Sanderson and Atle Rotevatn for great company and guidance during the fieldwork in Malta.

A special thank you to Charles and Anna at Maple Farm B&B for your kindness and hospitality during our weeks of fieldwork in Malta.

Thanks to NORCE for the academic license of the software LIME and to NORSAR Innovation for the use of the academic license of the NORSAR Software Suite/SeisRoX. MathWorks is thanked for the academic license to Matlab.

To my fellow students and friends at the Department of Earth Science, thank you for all the great memories throughout the past five years, although the final semester of our studies did not turn out as we might have wished for due to Covid-19. I would also like to thank Mari Johnsen and my sisters, Vigdis and Katrine, for proof reading of different parts of the thesis. A special thank you goes to my field partner, Mari Prestegård, for excellent company, great discussions and countless good memories both in the field and at the university. These past two years would not have been the same without you.

Finally, I would like to thank my family and Håvard for their unlimited support and for always believing in me.

Ingvild Gabrielsen Andersen

Bergen, June 2020

Contents

1	Introduction	1
1.1	Background and rationale	1
1.2	Aims and objectives	2
1.3	Study area	2
2	Geological Setting	4
2.1	Regional Tectonic setting	4
2.1.1	<i>Tectonic evolution of the Mediterranean</i>	4
2.1.2	<i>The Pantelleria Rift System</i>	5
2.2	The Maltese Islands	6
2.2.1	<i>The Maltese Graben System</i>	6
2.2.2	<i>The Maghlaq Fault zone</i>	7
2.3	Regional stratigraphic setting	8
2.3.1	<i>Pre-rift</i>	8
2.3.2	<i>Early syn-rift</i>	10
2.3.3	<i>Late syn-rift</i>	13
2.3.4	<i>Post-rift</i>	14
3	Theoretical background	15
3.1	Fault zone architecture	15
3.2	Faults in carbonates	17
3.3	Seismic expression and interpretation of faults	18
3.4	Seismic resolution	20
3.5	Seismic modeling	21
3.5.1	<i>Main modeling approaches</i>	22
3.5.2	<i>2(3)D PSF-based convolution modeling</i>	23
4	Data and methodology	28
4.1	Field work	28
4.1.1	<i>Stratigraphical logging</i>	28
4.1.2	<i>Outcrop mapping</i>	29
4.2	From outcrop to geological model	30
4.2.1	<i>Virtual outcrop models from photogrammetry</i>	30
4.2.2	<i>Geological models</i>	32
4.2.3	<i>Elastic Properties</i>	32
4.3	From outcrop to 2D synthetic seismic	34
4.3.1	<i>Sensitivity study</i>	36
5	Results	37
5.1	Geological interpretations of the Maghlaq Fault zone	37
5.1.1	<i>Stratigraphic interpretations</i>	38
5.1.2	<i>Structural interpretations</i>	39
5.2	Seismic modeling results	45
5.2.1	<i>Changing the dominant frequency</i>	45
5.2.2	<i>Adding noise</i>	49
5.2.3	<i>Changing the angle of illumination</i>	51
5.2.4	<i>Changing the angle of incidence</i>	55
5.2.5	<i>Choice of wavelet</i>	58
6	Discussion	62
6.1	Outcrop-based seismic modeling and applications to seismic interpretation	62

6.2	Seismic expression of the Maghlaq Fault.....	64
6.3	Effects of changing the geophysical parameters.....	66
6.3.1	<i>Effects of dominant frequency</i>	66
6.3.2	<i>Noise effects</i>	68
6.3.3	<i>Effects of dip-limited illumination</i>	69
6.3.4	<i>Effects of non-vertical incidence</i>	71
6.3.5	<i>Frequency-band effects</i>	72
6.3.6	<i>Summary of geophysical parameter effects</i>	73
6.4	Uncertainties related to the geological modeling	73
6.4.1	<i>Limitations to geological interpretations</i>	73
6.4.2	<i>Limitations to elastic properties</i>	75
7	Conclusion and further work	77
7.1	Concluding remarks	77
7.2	Suggestions for further work	78
	References	79
	Appendix A	85

1 Introduction

This study is one of two MSc theses investigating the seismic expression of the hanging wall geometry of a carbonate-hosted, large-scale normal fault zone on southwest Malta, by generating 2D synthetic seismic from field outcrops. The main focus of the present thesis is the effects of various geophysical parameters on the seismic expression of the fault zone, whereas the main focus of the sister project (Prestegård, 2020) is the impact of various geometrical complexities and properties of the fault zone on the synthetic seismic.

1.1 Background and rationale

Faults are internally heterogenous zones that have major impact on fluid flow properties in the subsurface. Detailed outcrop studies of variations in properties and internal geometries of a fault zone have improved the understanding of the complexity of faults (Caine et al., 1996; Bonson et al., 2007; Childs et al., 2009; Botter et al., 2014). However, interpreting these features in detail from seismic data is difficult due to resolution and illumination limitations. Although many of the internal structures of fault zones are of sub-seismic scales, seismic data are still a key tool for studying and understanding faults in the subsurface. Generating synthetic seismic data of outcrop analogues can improve seismic interpretation of structures in the subsurface.

Synthetic seismic is generated through seismic modeling, which is a method that enables comparison between detailed geological observations from outcrops and their potential signature in seismic (Falivene et al., 2010). Additionally, seismic modeling provides information on survey parameter effects, as well as potential pitfalls related to seismic interpretation (Lecomte et al., 2015; Anell et al., 2016). Synthetic seismic generated from outcrop analogues and conceptual models have previously been studied by several authors (e.g. Falivene et al., 2010; Botter et al., 2014; Osagiede et al., 2014; Lecomte et al., 2015; Anell et al., 2016; Frery et al., 2016; Eide et al., 2018; Lubrano-Lavadera et al., 2018; Rabbel et al., 2018; Grippa et al., 2019; Wrona et al., 2019), but few studies address seismic modeling of normal fault zones within carbonate successions. In this thesis, synthetic seismic generated from virtual outcrop models of the carbonate-dominated extensional fault zone of the Maghlaq Fault is studied in detail. Moreover, sensitivity analyses involving different geophysical survey parameters are carried out in order to investigate their effects on the simulated 2D seismic.

The following workflow was applied to obtain 2D synthetic seismic images of the Maghlaq Fault: 1) creation of virtual outcrop models from photogrammetric mapping of the outcropping hanging wall, 2) construction of geological models based on interpretations of the virtual outcrop models, 3) assignment of elastic properties to the geological models, 4) generation of synthetic seismic images by the use of 2D Point-Spread Function-based convolution modeling, and 5) variation of geophysical parameters. Controlling the geophysical survey parameters demonstrates how the seismic expression of the Maghlaq Fault changes as a result of various dominant frequencies, levels of noise, maximum illumination angles, incident angles and wavelet types. The resulting synthetic seismic images can help predict the level of structural and stratigraphic details which potentially will be resolved in 2D seismic. This could aid the seismic interpretation of fault zones in similar geological settings in the subsurface.

1.2 Aims and objectives

The main aims of this study are to improve the understanding of seismic imaging of carbonate-hosted normal fault zones and to investigate the impact of geophysical parameters on faults in seismic. These primary aims are achieved through a case study of the carbonate-bearing, extensional Maghlaq Fault with the following objectives:

- Create realistic geological models of the Maghlaq Fault zone based on virtual outcrop models of its hanging wall.
- Predict the 2D seismic expression and detectability of the fault zone by generating 2D synthetic seismic images.
- Through sensitivity analyses on these images, determine the effects of geophysical parameters, i.e. dominant frequency, level of noise, angle of maximum illumination, incident angle and wavelet type, on the seismic expression of the fault.

1.3 Study area

The study area is located on the southwestern coast of Malta, which is the largest island of the Maltese archipelago (Fig. 1.1). The archipelago is situated in the Central Mediterranean, 90 km south of Sicily and 300 km east of Tunisia. The Maltese Islands, which rise up to 253 m above sea level, form the northern flank of the Pelagian Platform – a shallow shelf platform connecting Europe and Africa (Illies, 1981; Pedley, 1989; Bonson et al., 2007; Micallef et al., 2013). The Oligocene-Miocene carbonate succession of Malta is cut by two main sets of extensional faults, oriented ENE-WSW and ESE-WNW. The Maghlaq Fault, which is

considered as the northernmost extent of the Pantelleria Rift System, is the only major fault on Malta trending ESE-WNW (Bonson et al., 2007). The coastline in the southwest of Malta provides excellent outcrops of the Maghlaq Fault's slip surface and hanging wall geometries. The hanging wall frequently crops out for a total of 2.5 km along the 4 km long exposure of the fault, forming great targets for outcrop mapping. Key outcrops in this study are the following: 1) Ix-Xaqqa, 2) Ras Hanzir, 3) Il-Miqtub, and 4) In-Neffiet (Fig. 1.1c).

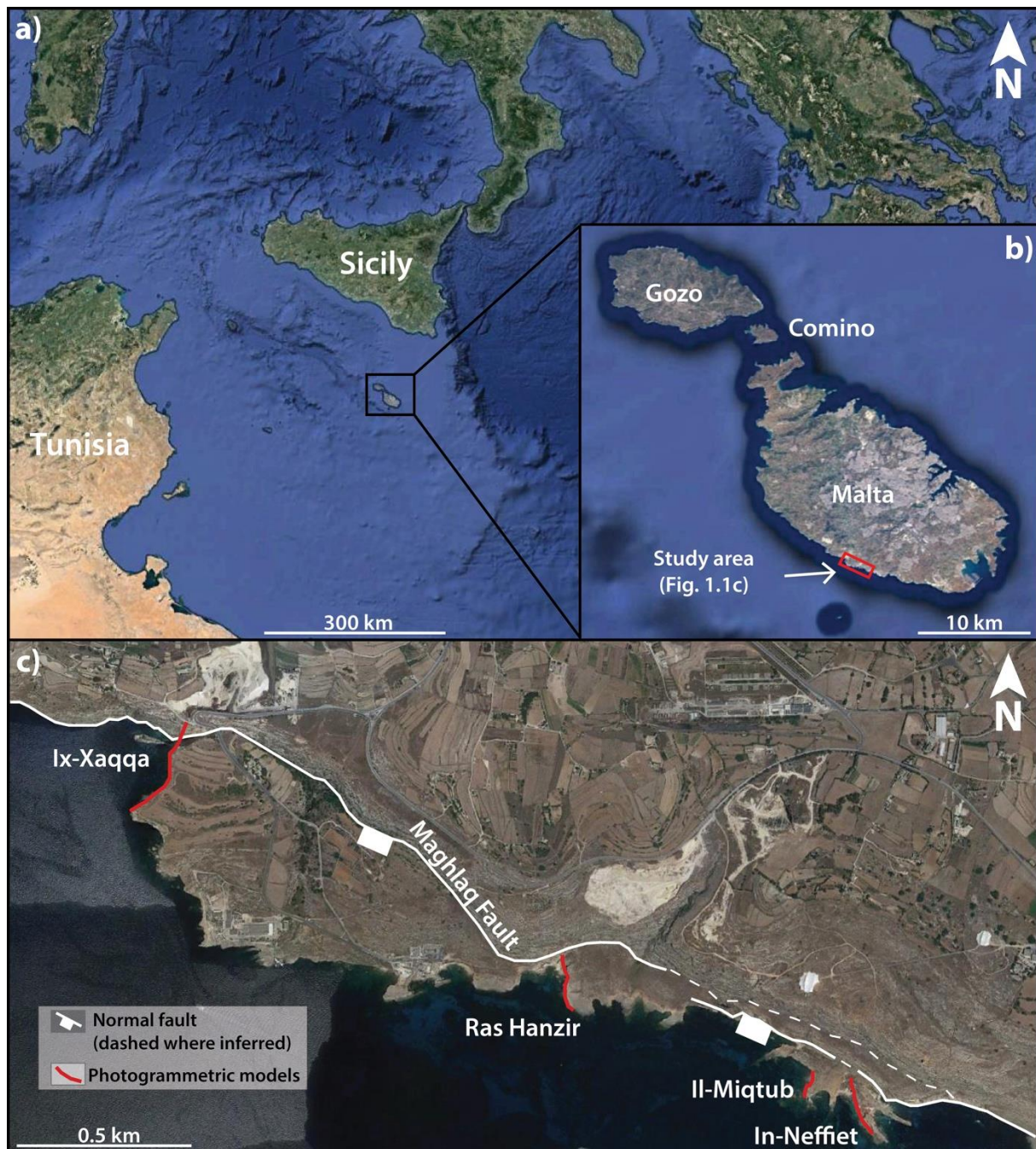


Figure 1.1: a) Location of the Maltese archipelago in the Central Mediterranean. b) The Maltese Islands, pointing out the study area along the Maghlaq Fault on the southwestern coast of Malta. c) Overview of the study area and key outcrops of the hanging wall of the fault. Satellite photos from Google Earth (2020).

2 Geological Setting

This chapter introduces the geological framework of the study area in terms of tectonic evolution, with focus on the Maltese Graben System within the Pantelleria Rift System. Furthermore, an overview of the stratigraphic framework of the carbonate-dominated succession on the Maltese Archipelago is provided.

2.1 Regional Tectonic setting

2.1.1 Tectonic evolution of the Mediterranean

The present-day geological configuration of the Mediterranean domain is a result of a tectonically complex evolution including both compressional and extensional events over a span of time (Rosenbaum and Lister, 2002; Cavazza and Wezel, 2003; Di Bucci et al., 2010). The evolution of the Mediterranean region has been dominated by the opening and closing of the Neotethys and Paleotethys oceans and the convergence between the African and Eurasian plates since Late Cretaceous times (Gueguen et al., 1998; Rosenbaum et al., 2002; Cavazza and Wezel, 2003; Di Bucci et al., 2010). This succession of convergent and extensional events has resulted in a system of connected fold-and-thrust belts and related foreland and back-arc basins, which all vary in terms of internal architecture and timing (Cavazza and Wezel, 2003).

The basins of the western to central Mediterranean are progressively younger from west to east – from Late Oligocene-Early Miocene in the west (Alboran Sea, Valencia Through and Provençal Basin), through Middle-Late Miocene eastward (Balearic and Algerian basins) and to Late Miocene and Plio-Pleistocene in the central part of the Mediterranean (Tyrrhenian Basin) (Kastens et al., 1988; Roca and Desegaulx, 1992; Gueguen et al., 1998). Two main orogenic belts are separating the basins of the Mediterranean – the Alpine-Betic-Dinaride mountain chain in the northwest and the Apennine-Maghrebide-Carpathian mountain chain in the east (Carminati et al., 2012). The associated extensional basins developed due to the back-arc extension which resulted from rollback of the Adriatic slab in the eastward retreating Apennines-Maghrebides subduction zone (Argnani, 1990; Gueguen et al., 1998; Rosenbaum and Lister, 2002).

The eastern part of the Mediterranean domain most likely comprises Mesozoic Neotethyan oceanic crust, overlain by a thick sedimentary package that reaches a maximum thickness of 12-14 km (Robertson and Dixon, 1984; Ben-Avraham et al., 2002; Rosenbaum et al., 2002; Carminati et al., 2012). The western Mediterranean, on the contrary, does not comprise Mesozoic crust, yet ophiolitic complexes can be found within the adjacent fold-and thrust belts, indicating the presence of older oceanic crust (Rosenbaum et al., 2002).

2.1.2 The Pantelleria Rift System

The Maltese Archipelago is located on the northeastern shoulder of the ESE-WNW striking Pantelleria Rift System, which is underlain by the Pelagian Platform (Fig. 2.1) (Reuther and Eisbacher, 1985). The Pelagian Platform is connecting southern Sicily to northwestern Libya and eastern Tunisia through a shallow shelf platform of African provenance with water depths of less than 400 m (Illies, 1981; Finetti, 1984; Reuther and Eisbacher, 1985; Micallef et al., 2013). The platform consists of continental crystalline basement overlain by Meso-Cenozoic carbonates and volcanics (Reuther and Eisbacher, 1985). Morphology and structures can be used to characterize four different zones within the Pelagian Platform: (i) the Malta Plateau, (ii) the Malta Escarpment, (iii) the fold and thrust belt of the Apennine-Maghrebian orogen and (iv) the Pantelleria Rift System (Fig. 2.1a) (Micallef et al., 2013).

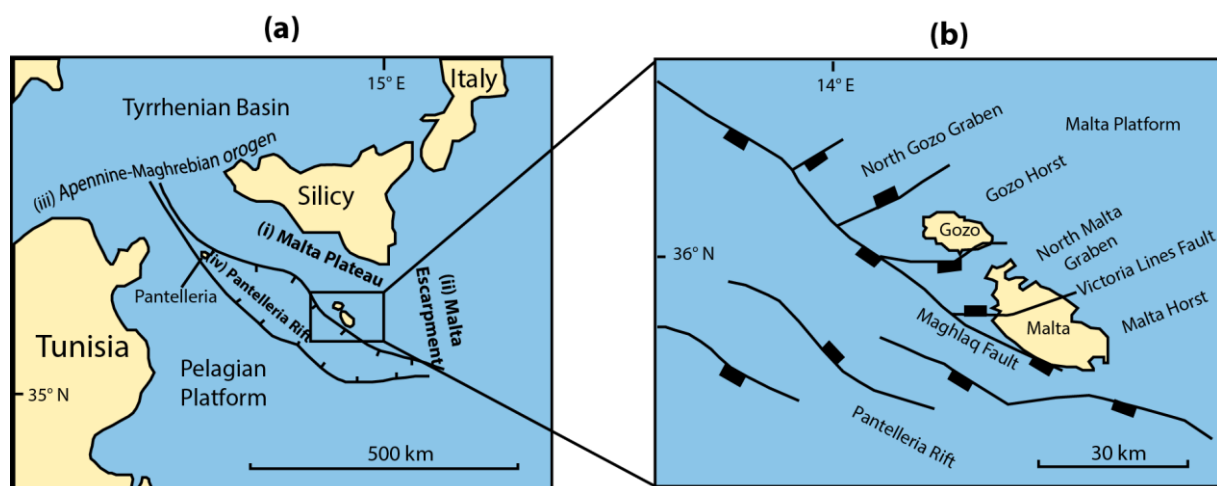


Figure 2.1: The Maltese Islands are located on the northeastern shoulder of the Pantelleria Rift, on the Pelagian Platform, which is connecting southern Sicily and eastern Tunisia (Reuther and Eisbacher, 1985; Micallef et al., 2013). (a) Four structural zones are characterized within the Pelagian Platform: (i) the Malta Plateau, (ii) the Malta Escarpment, (iii) the Apennine-Maghrebian orogen and (iv) the Pantelleria Rift System. (b) Main extensional fault systems comprising the structural framework of the Maltese Islands. Modified from Missenard et al. (2014) after (a) Bonson et al. (2007) and (b) Jongsma et al. (1987); Dart et al. (1993).

The Pantelleria Rift System, also known as the Strait of Sicily Rift (Finetti, 1982; Bonson et al., 2007), is a fault-controlled through representing the foreland of the Silician Neogene Apennine-Maghrebian fold and thrust belt (Argnani, 1990; Dart et al., 1993; Bonson et al., 2007). The rift system is composed of three throughs of depths of more than 1 km: the Pantelleria, Linosa and Malta grabens, which are all partially filled with Plio-Quaternary deposits (Dart et al., 1993). An uplifted, structurally inverted volcanic belt, oriented north-south, separates the Pantelleria Graben to the northwest from the Malta and Linosa grabens to the southeast (Argnani, 1990). The largely submarine rift system of Pantelleria is only exposed on the Maltese Islands, allowing studies of the Oligocene-Miocene syn-rift and Plio-Quaternary post-rift successions onshore (Reuther and Eisbacher, 1985).

2.2 The Maltese Islands

2.2.1 The Maltese Graben System

Uplift of the northern flank of the Pantelleria Rift System during Miocene times and onwards, in addition to a falling sea-level, resulted in the emergence of the Maltese Islands during early Messinian times (Pedley et al., 1987; Bonson et al., 2007). The entire pre- to syn-rift succession of the Maltese Islands is cut by two major sets of extensional faults of different ages and trends, constituting the Maltese Graben System (Illies, 1981; Argnani, 1990; Dart et al., 1993). This system is a small part of the Pantelleria Rift System and can be divided into five tectonic units: the North Gozo Graben, the Gozo Horst, the North Malta Graben, the Malta Horst and the Pantelleria Rift (Maghlaq Fault) (Fig. 2.1b) (Dart et al., 1993). The latter represents the youngest set of faults (Illies, 1981).

The first generation of faults, forming the horst-and-graben complex on northwestern Malta, eastern Gozo and Comino, has a NE-SW strike (Illies, 1981). The two grabens in the Malta Graben Systems are approximately 14 km wide, where the North Gozo Graben is the deepest of the two, bounded by a northwestern fault with a displacement of 1.6 km. The Victoria Lines Fault is located within the North Malta Graben and crosses Malta from west to east with a NE-SW strike (Fig. 2.1b) The Victoria Lines Fault holds the greatest displacement in the North Malta Graben of 195 m, however the throw generally decreases along the fault from west to east (Pedley et al., 1976; Dart et al., 1993). To the south of the large fault, the horst-and-graben structure is absent, replaced by extensive normal faulting with displacements of no more than

20 m (Pedley et al., 1976). The North Gozo Graben and the North Malta Graben both intersect the Pantelleria Rift to the west at acute angles of 66 and 32 degrees respectively (Dart et al., 1993). The Maghlaq Fault is situated on the periphery of the Pantelleria Rift and is the only major fault exposed on the Islands of Malta that has a strike parallel to the Pantelleria Rift (Dart et al., 1993; Bonson et al., 2007).

2.2.2 The Maghlaq Fault zone

The Maghlaq Fault is the largest fault on the southwestern coast of the island of Malta, with a minimum displacement of 210 m. It is a left-stepping, ESE-WNW striking normal fault cutting the pre- to syn-rift carbonates and clays on Malta (Fig. 2.2) (Dart et al., 1993; Bonson et al., 2007). The fault is well exposed along the cliffs over a distance of 4 km, and the hanging wall is preserved for a total distance of 2.5 km. The downthrown stratigraphic sequence is inclined at a high angle and can be studied in several cross sections along the coastline (Pedley et al., 1976; Bonson et al., 2007). The seaward-facing fault surface of the Maghlaq Fault is dominated by smooth slickensides, with some lenses of footwall rock smeared onto the plane structure (Pedley et al., 1976).

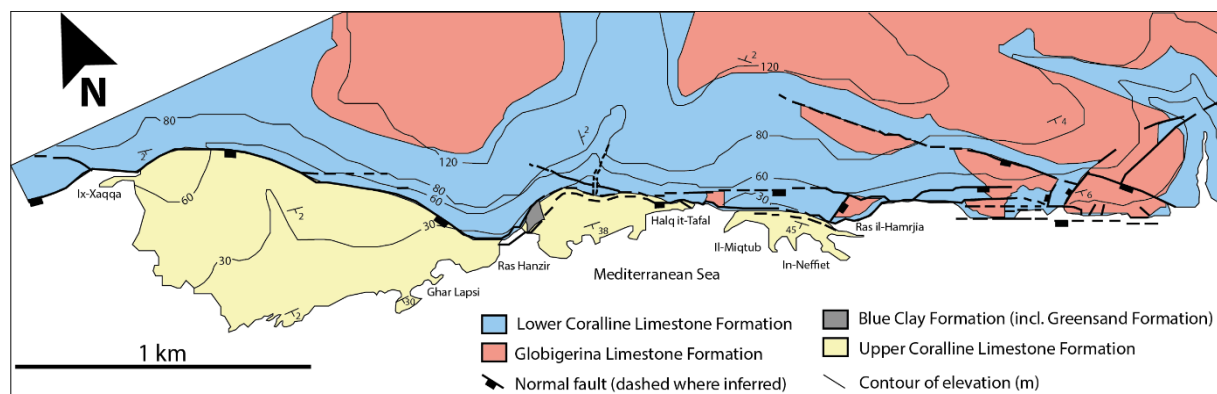


Figure 2.2: Geological map of the Maghlaq Fault, located along the southwestern coastline of the Island of Malta. Modified from Bonson et al. (2007).

Bonson et al. (2007) describes the characteristics of the Maghlaq Fault in detail, which is summarized as follows: The Maghlaq Fault is an en echelon normal fault array with 1-2 km long fault segments which are dipping 60-75 degrees to the S/SW. The tips of the segments are bent, causing short sections of the fault to strike E-W or ENE-WSW and resulting in fault linkage. The Maghlaq Fault has a 5-40 m thick prominent damage zone of very deformed rocks, which separates the less deformed hanging wall from the fault scarp. Between Ix-Xaqqa and

Ghar Lapsi (Fig. 2.2), the strata of the hanging wall are dipping 10-20 degrees to the S. Towards the east, drag folding of partially lithified carbonates has resulted in a steeper dip with up to 40 degrees to the S.

2.3 Regional stratigraphic setting

The onshore Maltese stratigraphy is dominated by shallow marine carbonates and consists of five formations that are easily traced across the islands (Fig. 2.3) (Pedley et al., 1976; Dart et al., 1993). The succession on Malta is underlain by non-exposed strata of Cretaceous times consisting of 3000 m of limestones, marls and dolomites (Pedley et al., 1976). The onshore carbonate succession of the Maltese archipelago is pre- to syn-rift deposits of Oligocene-Miocene age (Bonson et al., 2007). This includes, from oldest to youngest: pre-rift (>21 Ma) Lower Coralline Limestone Formation, pre-rift and early syn-rift (21-6 Ma) Globigerina Limestone Formation, early syn-rift Blue Clay Formation and Greensand Formation, and early to late syn-rift (<5 Ma) Upper Coralline Limestone Formation (Dart et al., 1993). The succeeding layers are post-rift (<1.5 Ma) sediments of Pliocene-Quaternary age, including fluvial, coastal and aeolian silts, cave deposits and tufa. Present-day deposition on the Malta Plateau is dominated by pelagic and hemipelagic sediments (Micallef et al., 2013). The characteristics of the five main carbonate formations on the Maltese Islands and the representative subdivision of phases, with respect to the Pantelleria rifting, are described in the following sections.

2.3.1 Pre-rift

Lower Coralline Limestone Formation

The oldest succession of the islands is the Chattian Lower Coralline Limestone Formation, which consists of shallow marine and massive platform carbonates in form of biosparites and biomicrites (Pedley, 1975; Dart et al., 1993). Only the top 140 m out of the 300-1000 m thick succession is exposed onshore along the western coasts of Malta and Gozo (Dart et al., 1993; Micallef et al., 2013). This limestone formation forms the extensive and steep cliffs on the west coast of the archipelago and crops out nicely in cliff-sections around the Maghlaq Fault in the southwest of the main island. The Lower Coralline Limestone Formation is stratified, consisting of layers of variable thicknesses from half a meter up to 3 meters (Felix, 1973).

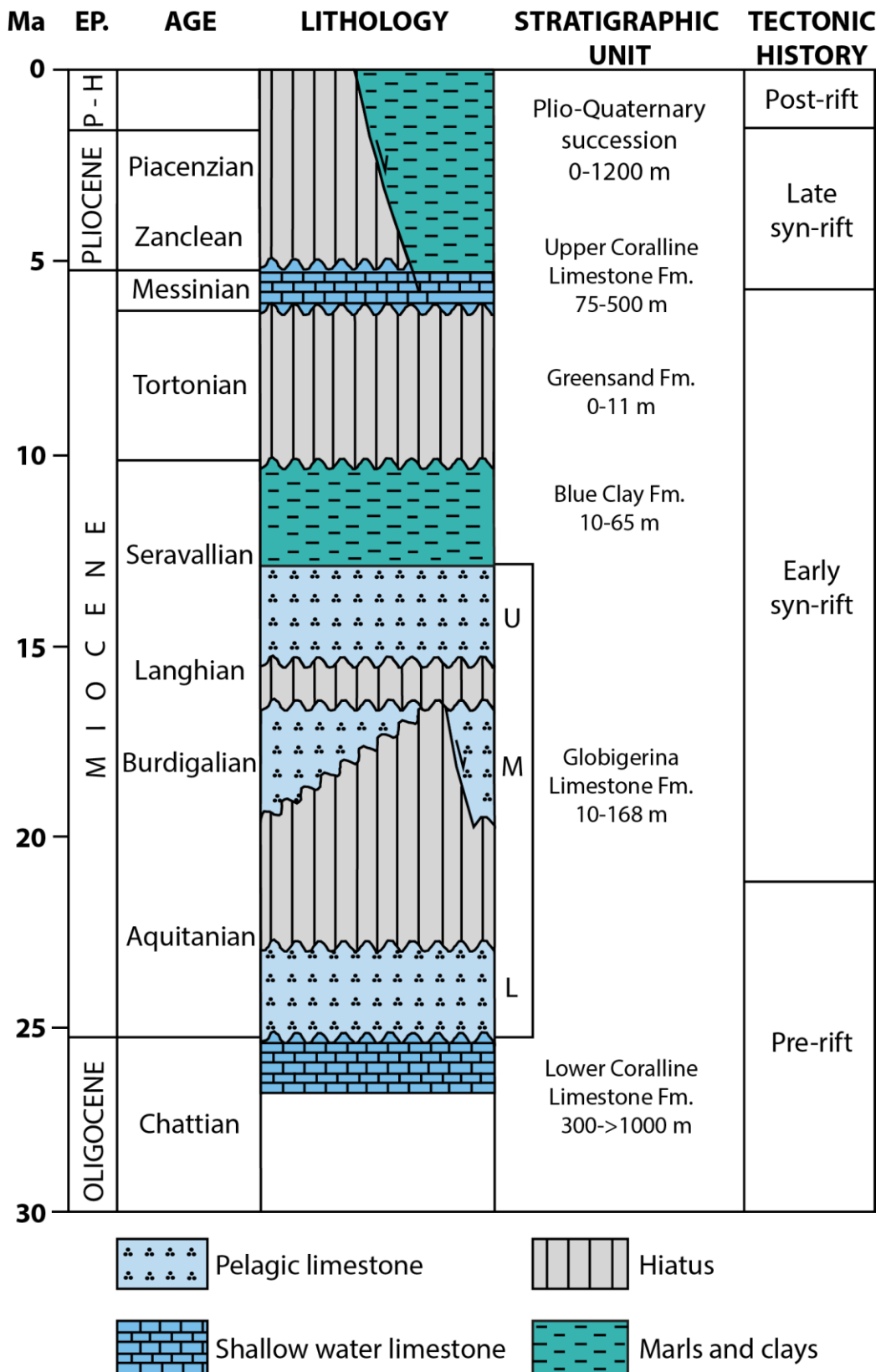


Figure 2.3: Tectono-stratigraphic log of the pre-, syn- and post-rift sedimentary successions of Oligocene-Quaternary age of the Maltese archipelago. Modified after Dart et al. (1993).

The lowermost part of the exposed section is consisting of benthic foraminifer-rich yellow biomicrites, conformably overlain by massive, pale-grey coralline algal limestones. Patch reefs developed in the western parts of Malta have caused the local absence of fossils other than rhodolitic algal. The top 10 m of the formation is composed of coarse bioclastic limestones (Pedley et al., 1976). The uppermost part of the formation is marked by a scutella bed which is rich in *Scutella subrotunda*, or, where the scutella bed is absent, the top is marked by a chocolate-brown hardground or a bed of pebbles (Pedley, 1975; Felix, 1973). The depositional environment of the Lower Coralline Limestone Formation was at first a shallow marine gulf favoring the deposit of detrital and algal limestones. The coarser and well bedded strata above indicate open marine conditions including wave action (Felix, 1973; Pedley et al., 1976).

Lower Globigerina Limestone Member

Above the Lower Coralline Limestone Formation, a 0-20 m thick cream-coloured, fine-grained biomicritic sequence of the Lower Globigerina Limestone Member of Aquitanian age is located (Pedley et al., 1976; Micallef et al., 2013). The Lower Globigerina Limestone Member is the earliest member of three subdivisions of the 23-207 m thick Globigerina Limestone Formation (Reuther, 1984). The subdivision of the formation is based on two interbedded phosphorite levels (Pedley, 1975). The Globigerina Limestone Formation is well exposed all over the Maltese Islands with various thicknesses, and characteristically weathers to form honeycomb patterns (Felix, 1973; Pedley et al., 1976). The upper limit of the Lower Globigerina Limestone Member is marked by one of the phosphorite conglomerate beds, which is above a well-developed hardground (Dart et al., 1993; Bonson et al., 2007). The top of the Lower Globigerina Limestone Member is cut by Neptunian dykes, indicating the start of the early rifting phase (Dart et al., 1993). The predominant planktonic lithology of the member indicates increased water depths during deposition (Pedley and Bennett, 1985; Dart et al., 1993).

2.3.2 Early syn-rift

The syn-rift successions of the Maltese islands can be subdivided into an early rifting phase and a late rifting phase with respect to the Pantelleria Rift System. Stratigraphic layers included in the early syn-rift phase are Middle and Upper Globigerina Limestone Members, Blue Clay Formation, Greensand Formation and the lower part of the Upper Coralline Limestone Formation (Pedley et al., 1976; Dart et al., 1993). Characteristically for the early syn-rift phase,

lasting from 21-6 Ma, are thickness variations of the strata related to minor faulting. The thicknesses of the syn-rift Globigerina Limestone Formation and Blue Clay Formation are significantly greater within the offshore Pantelleria Rift and North Gozo Graben relative to the equivalent interval onshore, as revealed from depth-converted seismic sections of the area (Dart et al., 1993; Bonson et al., 2007).

Middle Globigerina Limestone Member

The first part of the syn-rift succession is the 100 m thick Middle Globigerina Limestone Member of Burdigalian age. The lithology of the member is similar to the Lower Globigerina Limestone Member, and comprises white to grey, predominantly coccolithic limestone with local seams of pebbles, chert and lenses of clay (Felix, 1973; Pedley and Bennett, 1985). Similarly to the Lower Globigerina Limestone Member, this member also varies in thickness across the islands, and is partly to fully eroded in central Malta and eastern Gozo (Dart et al., 1993). Bivalves and echinoids are commonly occurring in the biomicrite of Middle Globigerina Limestone Member (Pedley et al., 1976). The top of the Middle Globigerina Limestone Member is marked by the upper main phosphorite conglomerate bed, which can be traced across both Malta and Gozo (Pedley et al., 1976; Pedley and Bennett, 1985; Dart et al., 1993).

Upper Globigerina Limestone Member

The final member of the Globigerina Limestone Formation is the 14-18 m thick Upper Globigerina Limestone Member, consisting of a pale-grey marly biomicrite overlain by a pale-yellow globigerinid biomicrite (Pedley et al., 1976). It is Langhian in age and the member contains fossils restricted to echinoids and gastropods (Pedley et al., 1976). The uppermost part of the member is poorly exposed along the coast of the islands. It is a transitional layer from marly limestone of the Globigerina Limestone Formation into clay of the Blue Clay Formation (Felix, 1973). Felix (1973) suggests that the presence of hardgrounds and beds of conglomerate in the Globigerina Limestone Formation indicates that the deposition of sediments was at or close to sea-level at times. He further suggests that most of the limestones of the formation were deposited in shallow water depths of 40-150 m, whereas the upper part of the formation seems to have been more open marine, which is evident from the occurrence of planktonic foraminifera.

Blue Clay Formation

The Serravilian Blue Clay Formation is conformably overlying the Globigerina Limestone Formation. The up to 65 m thick formation is composed of slightly consolidated, blueish, hemipelagic clays and alternating beds of dark and light grey marls (Pedley et al., 1976; Micallef et al., 2013). The internal color change of the marls is caused by the carbonate content, which never exceeds more than 30 percent (Pedley et al., 1976). The formation is exposed on Gozo, Malta and possibly also at the base of the cliffs of Filfla, the island located at the western coast of Malta. The upper limit is characterized by an increase in the content of glauconite in the clay, as the Blue Clay Formation gradually transitions into the succeeding Greensand Formation. The clay becomes darker as the glauconite content increases, and the color changes from bluish-grey to greyish-green (Felix, 1973). The Blue Clay Formation was deposited in an open, muddy marine environment with abundant supply of terrigenous material deposited from suspension (Felix, 1973; Pedley et al., 1976).

Greensand Formation

The Tortonian Greensand Formation is only 1-12 m thick, and consists of poorly cemented, greenish, glauconitic biosparite and biomicrite (Pedley, 1975; Dart et al., 1993). The Greensand Formation is found on both Malta and Gozo. There are two types of the formation; the lower, more clay-rich sediment and the upper, calcareous type (Felix, 1973). There is a gradual transition from the top of the Greensand Formation to the base of the Upper Coralline Limestone Formation above due to abundant bioturbation, which indicates a shallow marine depositional environment (Pedley et al., 1976).

Upper Coralline Limestone Formation

The youngest formation on the Maltese archipelago is the Upper Coralline Limestone Formation, which is Late Tortonian to Messinian in age and is present all over the archipelago (Bonson et al., 2007). The formation is similar in lithology to the Lower Coralline Limestone Formation, composed of a shallow water reef complex with a maximum thickness of 162 m (Pedley et al., 1976; Micallef et al., 2013). The formation weathers into steep cliffs and karst topography such as caves and sink holes from subaerial exposure (Pedley, 1975; Pedley et al., 1976). The sequence is mainly consisting of coralline algae that indicates a shallow marine

depositional environment (Felix, 1973). The Upper Coralline Limestone Formation can be divided into three divisions based on the time of deposition. The two earliest lithologies were deposited during the early syn-rift phase, whereas the youngest layer was deposited during the late stage of the syn-rift phase (Dart et al., 1993).

Depositional phases 1 and 2

Depositional phase 1 comprises brown biosparites to the west of Malta and white to cream-colored biomicrites to the east, separated by coralline algal bioherm in between (Pedley, 1978). The younger depositional sequence 2 consists of coarse-grained bioclastic and oolitic limestones rich in coralline algae, as well as coral and algal patch reef deposits in western parts of the islands (Pedley et al., 1976; Dart et al., 1993). In southwestern Malta, the depositional sequence 2 thickens from the footwall to the hanging wall of the Maghlaq Fault from 12 to 35 m, respectively, indicating creation of accommodation space by the growing fault (Dart et al., 1993).

2.3.3 Late syn-rift

Upper Coralline Limestone Formation

Depositional phase 3

The uppermost sequence of the Upper Coralline Limestone Formation from the late syn-rift phase is only locally preserved, exposed in northwestern and western Malta. It consists of biomicrites and biosparites with a widespread oosparite at the base (Pedley, 1978). These deposits indicate a platform and slope environment (Bosence and Pedley, 1982). The Upper Coralline Limestone Formation show distinct changes in both thickness and facies across the Maghlaq Fault, and thus represents the main syn-faulting sequence (Bonson et al., 2007). For instance, across the fault close by Ras Hanzir (Fig. 2.2) to the southwest of Malta, the thickness of the Upper Coralline Limestone Formation's depositional phase 3 is 30 m thicker in the hanging wall, than in the footwall (Dart et al., 1993).

Plio-Quaternary succession

The Upper Coralline Limestone Formation is overlain by a succession of Plio-Quaternary age, consisting of marls and carbonate mudstones (Dart et al., 1993). The succession was deposited during the Zanclean reflooding of the central Mediterranean. Due to the significant relief of the area, sedimentation only occurred in the Pantelleria Rift and in the North Gozo Graben (Dart et al., 1993).

2.3.4 Post-rift

Insignificant amounts of seismic activity and no fault movement suggest that present day deposition occurs in the post-rift phase, although there is a diffuse transition between syn-rift and post-rift deposits (Jongsma et al; 1984; Dart et al., 1993). The onshore post-rift deposits are discontinuous and form infillings in caves and fissures (Pedley et al., 1976; Micallef et al., 2013). Several animal bone deposits of Pleistocene age occur in caves and surface depressions. All these bone deposits indicate a more temperate climate than on present day Malta, and it is reasonable to think that a connection of land between Malta and Sicily could have been present at this time (Pedley et al., 1976). The youngest deposits on the islands of Quaternary age, consist of tufa, fluvial gravels, calcretes, cave deposits and terra rossa (Pedley, 1975; Pedley et al., 1976).

3 Theoretical background

This chapter provides a review of the theoretical background on which this thesis builds. It is divided into three main parts: the first part describes the fault zone architecture, both in a general aspect and specific to carbonate rocks, the second part presents the seismic expression and interpretation of faults, and the third part outlines the theory behind seismic modeling.

3.1 Fault zone architecture

Fault zones are lithologically and structurally heterogeneous, comprising two primary architectural components: a fault core and an associated damage zone, which are surrounded by undeformed protolith (Fig. 3.1) (Caine et al., 1996; Shipton and Cowie, 2001; Childs et al., 2009). The core of the fault is a zone of intense deformation, where most of the displacement is accommodated, consisting of one or several slip surfaces, fault rocks, i.e. fault gouge, breccias and cataclasites, and lenses of host or fault rock (Bastesen et al., 2009; Childs et al., 2009; Bastesen and Braathen, 2010; Michie et al., 2014). The core is surrounded by a footwall and a hanging wall damage zone on each side (Bastesen et al., 2009).

The damage zone is defined by Kim et al. (2004) as the volume of deformed wall rocks around a fault surface that results from the initiation, propagation, interaction and displacement accumulation along a slip surface. Discrete structures such as fractures and deformation bands are characteristic for the damage zone (Shipton and Cowie, 2001; Braathen et al., 2009). Lithology, the dip of strata relative to the slip direction of the fault and stress systems are factors that control the nature of a damage zone (Kim et al., 2004). The width of the damage zone generally increases as offset is accumulated and the fault continues to propagate (Shipton and Cowie, 2001, 2003; Riley et al., 2010). The development of fault zone geometries provides information on growth and propagation of the fault (McGrath and Davison, 1995; Kim et al., 2004), which can further provide a better understanding of the petrophysical properties of the fault zone and its influence on fluid flow (Michie et al., 2014).

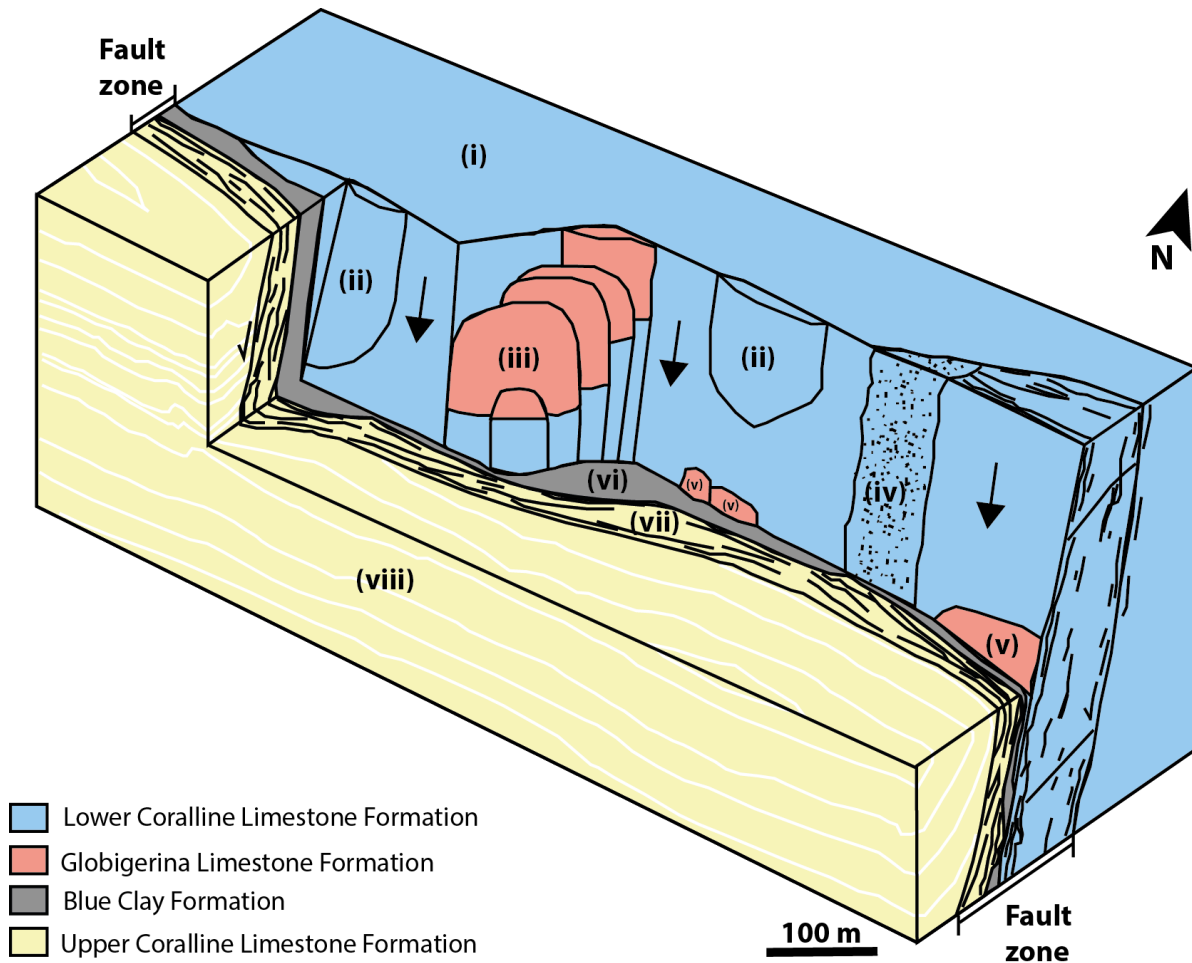


Figure 3.1: Illustration of the characteristic fault zone architecture of the Maghlaq Fault. (i) The footwall comprises undeformed protolith of Lower Coralline Limestone Formation. (ii) Host rock lenses of Lower Coralline Limestone Formation, (iii) overlapping lenses of Lower Coralline Limestone Formation and Globigerina Limestone Formation, (iv) breccia of Lower Coralline Limestone Formation and (v) lenses of Globigerina Limestone Formation are present on the fault surface. (vi) A continuous layer of Blue Clay Formation with highly variable thickness. (vii) A continuous hanging wall shear zone and (viii) dipping layers comprised of Upper Coralline Limestone Formation. Modified after Bonson et al. (2007).

The internal complexity of a fault zone, e.g. juxtaposition and fault properties, is important when considering fluid flow, as a fault can act as a barrier, a conduit or a combination of the two, in the subsurface (Caine et al., 1996; Evans et al., 1997; Childs et al., 2009; Rotevatn and Fossen, 2011; Michie et al., 2014). The combination often includes sealing effects for across-fault flow and conduits for along-fault flow (Rotevatn and Fossen, 2011). In terms of the permeability architecture of a fault zone, the core typically forms a zone of low permeability, whereas the damage zone forms a zone of high permeability, due to the presence of fault-related fractures. (Caine et al., 1996; Billi et al., 2003). A high density of vertically extensive fractures in the damage zone can act as important fluid flow conduits, and commonly occurs in a segment linkage fault such as the Maghlaq Fault (Bonson et al., 2007).

3.2 Faults in carbonates

The evolution and propagation of faults in carbonates occur over a wide range of scales and are primarily controlled by the lithofacies of the rock (Putz-Perrier and Sanderson, 2010; Michie et al., 2014). The strength and texture of the protolith exert strong controls on the deformation style and the type of fault rocks produced. Pressure solution is a deformation process that plays an important role during fault nucleation and growth in carbonates (Peacock et al., 1998; Graham et al., 2003; Bonson et al., 2007), and forms pressure solution seams, which impacts the distribution of slip surfaces (Willemse et al., 1997; Peacock et al., 1998). The heterogeneity of fault rocks in the core is largely controlled by the variation in juxtaposition of lithofacies along the fault surface, and may increase with greater displacement (Bastesen and Braathen, 2010; Michie, 2015). Studies of carbonate-dominated fault zones' internal geometry and distribution of deformation structures allows for a better understanding of their influence on fluid flow in a fault system (Caine et al., 1996; Childs et al., 1997; Bonson et al., 2007; Bastesen et al., 2009).

Michie et al. (2014) carried out a detailed study of the relationship between the carbonate facies and fault zone architecture on Malta, whereby some general observations and conclusions were made for faults in carbonate rocks. The lithologies of the fault zones comprise Lower Coralline Limestone overlain by a succession of Globigerina Limestone Formation. The Lower Coralline Limestone, which is heterogenous and grain-dominated, composed of coarse and rigid grains, has a high rock strength which localizes the deformation, resulting in a classic fault zone architecture including a core and a surrounding damage zone. Protocatasites, cataclasites and breccia form in response to deformation on the grain-scale (Fig. 3.2a), and, if cementation occurs, they can act as barriers for fluid flow (Michie et al., 2014; Michie, 2015). The Globigerina Limestone, which is homogenous and micrite-dominated, is on the contrary weaker, as it consists of very fine particles in a micritic matrix, and will deform by intense through-going fracturing (Fig. 3.2b), forming networks that can create dilation breccias. Fault rocks created from the micrite-dominated facies can be recrystallized, which may result in the formation of a barrier to fluid flow (Michie et al., 2014; Michie, 2015).

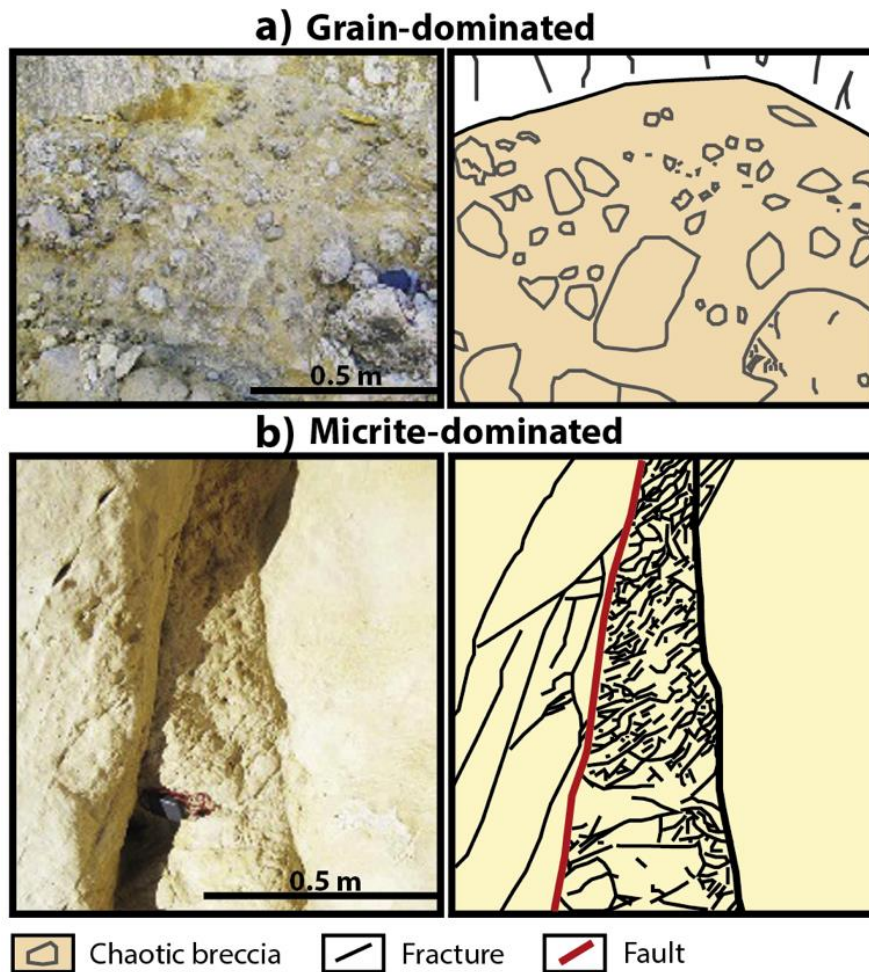


Figure 3.2: Field examples and corresponding sketches of the deformation styles dominating two low displacement fault zones (11.7 m in a) and 5 m in b)) on the southwestern coast of Malta. a) The deformed grain-dominated Lower Coralline Limestone forms chaotic breccia, whereas b) the deformed micrite-dominated Globigerina Limestone forms fracture networks. Modified after Michie et al. (2015).

3.3 Seismic expression and interpretation of faults

In nature, most faults and some fault-related structures are too steep to be illuminated with their true dips in seismic (Rotevatn and Fossen, 2011; Alaei, 2012; Saffarzadeh et al., 2019). This issue is related to dip-limited illumination in the seismic and/or lack of contrast in acoustic impedance between the fault surface and the surrounding rocks. A weak, or no, contrast in acoustic impedance results in a weak or absent reflectivity, and hence no seismic reflection representing the plane structure of the fault. However, the seismic expression of a fault can be recognized from reflection geometries surrounding it. Faults in seismic generally show a distinct displacement pattern across the surface of the fault, and are commonly identified by discontinuous, displaced reflection events (Freeman et al., 1990; Rotevatn and Fossen, 2011). Furthermore, they can be identified not only from discontinuous reflectors, but also from seismic diffraction patterns. Diffractions are scattered waves, which are generated by geological

discontinuities, such as unconformities, fractures and faults (Hilterman, 1970; Landa, 2012). Although diffractions are essentially weaker than the reflected energy and may even be further weakened during seismic migration, they do give valuable indications of structural features in the subsurface (Khaidukov et al., 2004; Landa, 2012). Moreover, seismic data are a combination of seismic signals and various noise, which reduces the quality of the data (Sheriff, 1978; Hesthammer et al., 2001). Noise appears in the seismic data as a result of several different sources, e.g. acquisition and processing. Faults commonly cause chaotic seismic images, which is related to the complexity of the structure as well as limitations to both resolution and illumination in the seismic (Hesthammer et al., 2001; Rotevatn and Fossen, 2011).

Faults in seismic are commonly subdivided into two types: seismically resolvable faults and sub-seismic faults (Gauthier and Lake, 1993; Townsend et al., 1998). The resolvability and detectability of faults in seismic is in addition to the acoustic impedance contrast, also controlled by the seismic resolution and signal-to-noise ratio of the seismic (Zhang and Castagna, 2011; Simm and Bacon, 2014; Grippa et al., 2019). Moreover, faults in seismic are often interpreted as simple 2D plane surfaces, when in reality they are zones of complex 3D volumes with heterogenous rocks and structures (Fig. 3.3) (Botter et al., 2014). Internal structures within the core and damage zone of seismic-scale faults are usually below seismic resolution, although it is possible for small-scale structures to be detectable without being fully resolved. This can happen if they have higher amplitudes than the background geology. Such small-scale structures can have a great impact on the connectivity across faults (Childs et al., 1997; Walsh et al., 1998). This is important information that is seldom included in a faulted reservoir model due to lack of time and financial resources, resulting in less realistic fluid flow simulations (Townsend et al., 1998). Including geometric heterogeneity in a three-dimensional way when interpreting faults in seismic can have a major impact on hydrocarbon exploration and production, CO₂-storage as well as hydrogeological and geothermal systems (Wibberley et al., 2008; Botter et al., 2014).

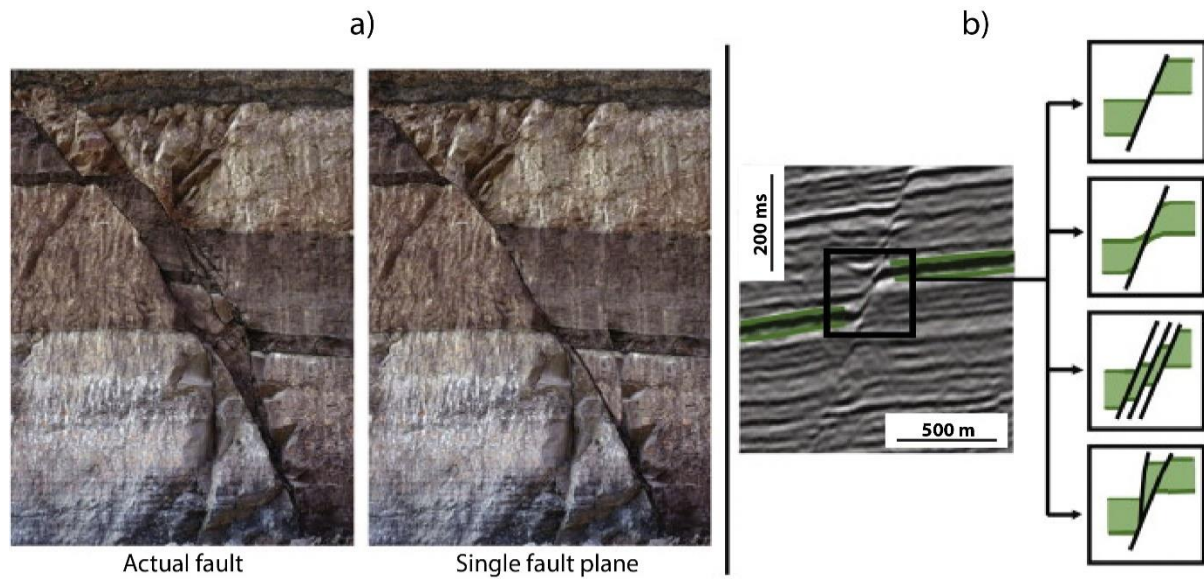


Figure 3.3: a) An outcrop example of a complex fault zone with several slip surfaces (left) and how it is often interpreted in seismic if the complexities of the core is not resolved (right). b) A plane structure of a fault in a 2D seismic section (left) and four different interpretations of the case (right). Modified after Botter et al. (2014).

3.4 Seismic resolution

The seismic resolution decides the resolving power of the seismic data, as well as the level of structural and stratigraphic details that can be observed in seismic images of the subsurface (Herron, 2011). The resolution of a seismic dataset is determined by the dominating wavelength, λ , given by:

$$\lambda = \frac{v}{f} \quad (\text{Eq. 3.1})$$

where v is the seismic velocity and f is the dominant frequency. Generally, with an increase in depth, the frequency will decrease and the velocity increase, resulting in an overall decrease in the seismic resolution (Rafaelsen, 2006; Simm and Bacon, 2014). Seismic resolution in the vertical direction is indicated by the tuning thickness, which, as a rule of thumb, is equal to a quarter of the wavelength (Simm and Bacon, 2014). Despite this indication, the resolution may vary across a resolved area due to variations in the vertical and lateral velocity and the dominant frequency in the subsurface (Herron, 2011).

The lateral resolution is described by the Fresnel zone, which is defined as the area of the wavefront from which the dominant part of the reflection originates. (Herron, 2011; Simm and Bacon, 2014). The size of the Fresnel zone is significant when considering lateral changes in a seismic profile, e.g. facies changes, channel cuts and stratigraphic wedges (Lindsey, 1989). Migration, the process where reflection events are reconstructed and moved to a correct lateral

position and vertical time or depth (Kearey and Brooks, 1991), has a focusing effect on the energy distributed across the Fresnel zone. The Fresnel zone effect therefore differs for pre- and post-migrated data (Sheriff, 1996; Thore and Juliard, 1999). Seismic objects that are smaller than the Fresnel zone will not be distinguished from each other on the seismic image (Simm and Bacon, 2014). As the seismic migration collapses the Fresnel zone, the lateral resolution of the seismic data increases. As illustrated in Fig. 3.4, if the data are 2D, the Fresnel zone is reduced in one dimension, forming an ellipse. Whereas for 3D seismic, the Fresnel zone shrinks to a small circle with a diameter of $\lambda/2$ (Kearey and Brooks, 1991; Sheriff, 1996; Rafaelsen, 2006; Herron, 2011).

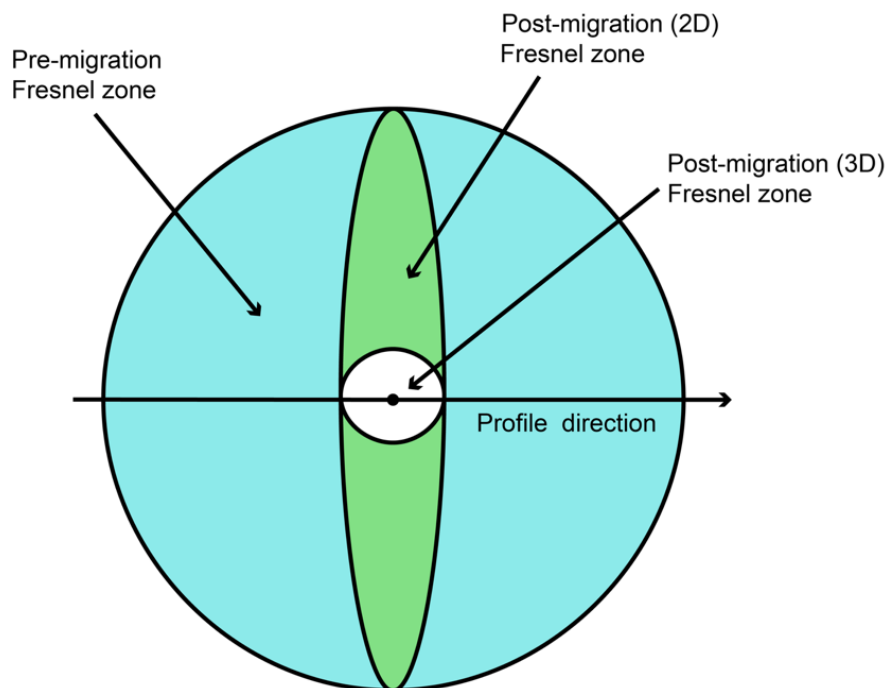


Figure 3.4: Seismic migration collapses the Fresnel zone in one dimension to an elliptical form for 2D seismic and reduces it to a small circle for 3D seismic. Modified after Simm and Bacon (2014).

3.5 Seismic modeling

Seismic modeling is a way of understanding elastic wave propagation in the subsurface (Lecomte et al., 2016). Seismic modeling can be performed on a realistic geological model in order to generate synthetic seismic images, which can help bridge the gap between field observations and seismic interpretation. This method gives the numerical computation of seismic responses for an earth model by simulating elastic wave propagation in the model (Carcione et al., 2002; Alaei, 2012). Adequate seismic modeling techniques, suitable elastic properties and detailed structural input, e.g. from virtual outcrop models of field analogues, are necessary for realistic seismic modeling that can aid the understanding of seismic imaging of the subsurface (Rabbal et al., 2018).

Seismic modeling techniques further provide a better understanding of the resolution, scale and details in real seismic data (Anell et al., 2016; Rabbel et al., 2018). In addition, the synthetic seismic holds valuable information on potential pitfalls and limitations of seismic data, e.g. seismic resolution issues and illumination limitations (the ability to image dipping structures) (Lecomte et al., 2015; Anell et al., 2016). The evaluation and design of the geophysical parameters used in a seismic survey can also be improved from seismic modeling (Carcione et al., 2002; Anell et al., 2016).

3.5.1 Main modeling approaches

Three main approaches are frequently used for seismic modeling: 1D convolution modeling, 2(3)D full-wavefield modeling and 2(3)D ray-based modeling (Lecomte et al., 2015). The 1D convolution modeling approach is used for horizontally stratified structures where lateral velocity variations are absent (Lecomte, 2008; Lecomte et al., 2015). This method is commonly used in seismic for, e.g., well-tie analysis in order to link the geological beds in a well to the corresponding seismic response (Alaei, 2012). As the geological input models to seismic modeling are improving, due to more detailed digital outcrop mapping, the 1D convolution method becomes too simplistic compared to 2(3)D modeling (Lecomte et al., 2016).

The first of the two main 2(3)D modeling approaches is the full-wavefield seismic modeling, which is more efficient, yet resource expensive compared to the 1D convolution modeling. The full-wavefield method generates complete synthetic seismograms based on numerical solutions to the wave equation. This approach is considered an ideal seismic modeling strategy where the synthetic seismic data can be processed like done with real seismic data (Lecomte et al., 2015, 2016). The second main 2(3)D modeling approach is the ray-based approach, for which the full-wavefield is not taken into account (Carcione et al., 2002). Ray-based modeling is a flexible approach that allows for changes and analysis of various parameters affecting the resolution and illumination of the seismic data (Lecomte et al., 2015, 2016). This approach is more cost- and time-effective compared to the full-wavefield method and is hence applied more frequently, despite limitations when it comes to modeling detailed and complex target structures (Lecomte et al., 2015, 2016).

3.5.2 2(3)D PSF-based convolution modeling

In this thesis, a simplified version of the ray-based modeling method has been applied. This is a 2(3)D convolution method, where a 2(3)D spatial pre-stack convolution operator, a so-called Point-Spread Function (PSF), is used to produce synthetic seismic. This method convolves the reflectivity input model with the PSF to generate Pre-stack Depth Migration (PSDM) seismic images (Lecomte et al., 2015, 2016). PSDM images are seismic images of the subsurface reflectivity generated in the depth domain by seismic processing (Lecomte, 2008; Lecomte et al., 2015). 2(3)D PSF-based convolution is a method that relies on the entire input grid of the model instead of dealing with one column of that grid at a time (Fig. 3.5). PSFs are, amongst other parameters, functions of the seismic survey, the input wavelet and the background velocity (Lecomte, 2008; Lecomte et al., 2015, 2016). PSF-based convolution modeling is beneficial due to its ability to capture detailed structures from virtual from outcrop models and generate more realistic seismic (Lecomte et al., 2016).

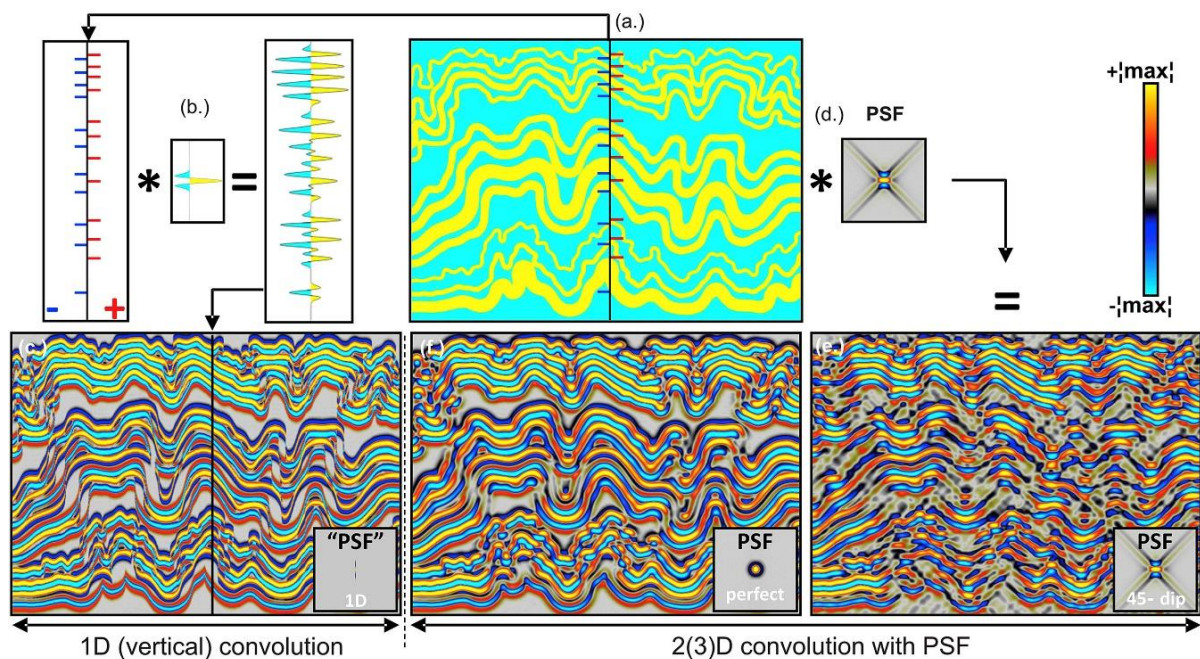


Figure 3.5: Main steps of the 1D and 2(3)D convolution modeling approaches to generate synthetic seismic images of fold structures. a) Model containing the input for acoustic impedance of the folds. b) A reflectivity log is convolved with a wavelet to form a synthetic trace. c) The resulting synthetic seismic of the 1D convolution modeling, shown in the depth domain for ease of comparison between 1D and 2(3)D seismic. d) The Point-Spread Function (PSF) which the reflectivity input model is convolved with in order to perform 2(3)D convolution modeling. e) The resulting synthetic seismic with a maximum illumination angle of 45° and f) perfect illumination (with dips up to 90°). From Anell et al. (2016).

2(3)D convolution modeling should indeed be favored over 1D convolution modeling for geologically complex models, as it allows seismic modeling with realistic illumination and resolution effects (Lecomte et al., 2016). While 1D convolution modeling perfectly images steeply dipping reflectors, the imaging of these structures would be limited by the angle of maximum illumination on real 2(3)D seismic images. Which parts of a geological dipping feature that are imaged is determined by the illumination angle, which also constrains the lateral resolution (Wrona et al., 2019). The PSF-based modeling results in a blurred representation (resolution) of the input model, and possibly missing elements of that model (illumination), which mimics a PSDM image described as in the following (Lecomte, 2008).

Fig. 3.6 briefly explains the steps and parameters included in the 2(3)D PSF-based convolution approach as given by Lecomte et al. (2015, 2016). A key feature in this approach is the illumination vector, I_{SR} (Fig. 3.6a). For a given velocity model and seismic survey with a shot (S) and a receiver (R), an illumination vector can be generated at a reference or target point, P (Lecomte et al., 2015, 2016). I_{SR} is characterized by its orientation and length, which further control the illumination and resolution of PSDM imaging at the target point, P (Lecomte et al., 2016). For instance, a horizontal reflector close to the target point will only be illuminated in the PSDM image if a vertical I_{SR} exists, as shown in Fig. 3.6a (Lecomte et al., 2016). Similarly, a reflector with a geological dip of 45° will only be illuminated in the seismic if an I_{SR} perpendicular to this reflector exists.

The first step in the 2(3)D PSF-based convolution modeling process is generating a PSDM filter by adding parameters such as an angle of maximum illumination (I_{SR} span) (Fig. 3.6b) and a wavelet (Fig. 3.6c). In this thesis, a generic I_{SR} span is used in the seismic modeling. This can be generated if the background velocity and survey information are unknown. The I_{SR} is then defined by an average velocity (V) and an incident angle (θ), where a high velocity and/or incident angle results in a short illumination vector span (Lecomte et al., 2016). The difference between the incident angle and the illumination angle is illustrated in Fig. 3.7.

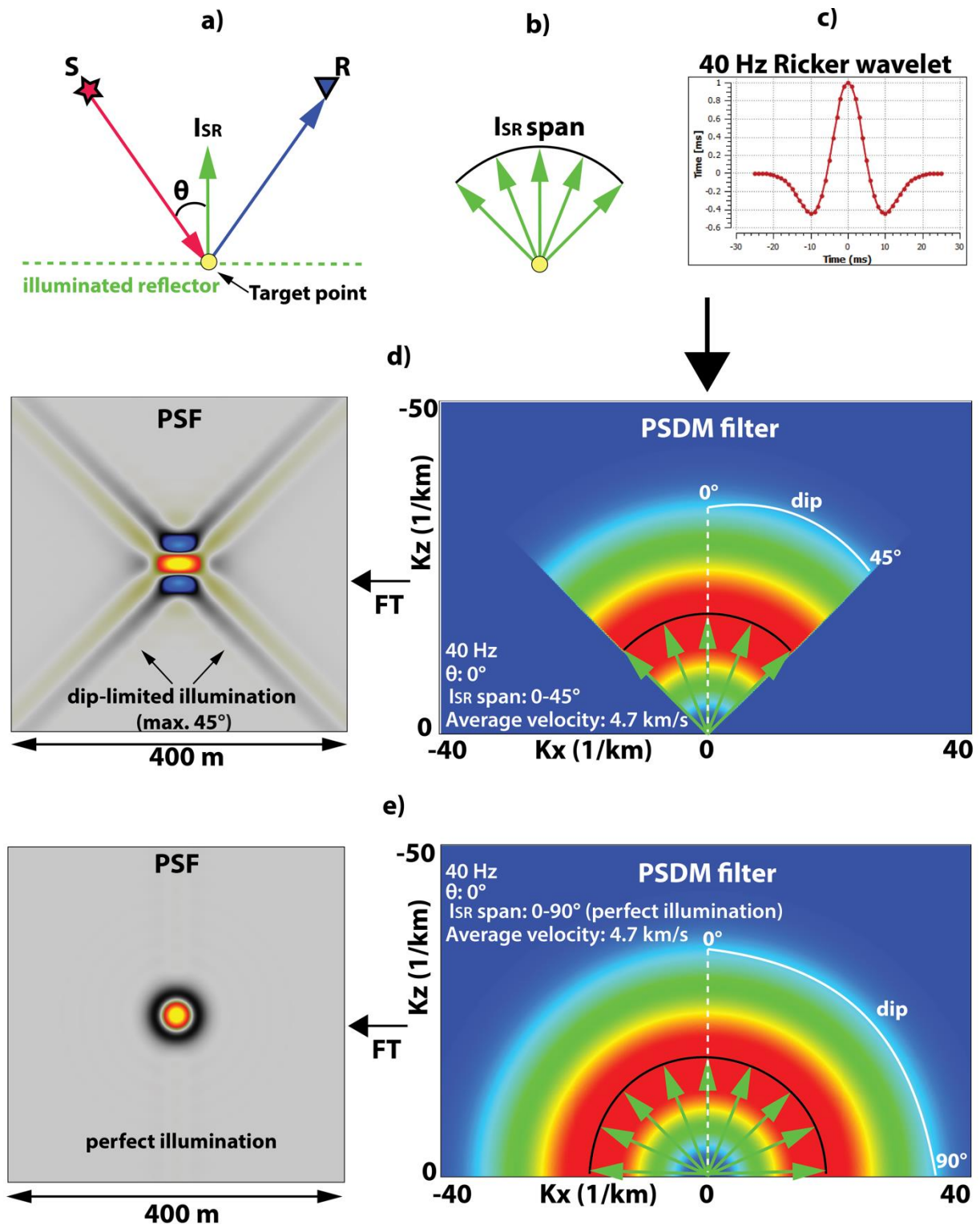


Figure 3.6: The parameters used for generating PSDM images from simulated PSFs. a) For a given velocity model and a) a seismic survey with a shot (S) and a receiver (R), an illumination vector, I_{SR} , at a target point, P, is generated. b) A generic I_{SR} span can also be generated if the velocity model and survey information are unknown. c) Amongst other parameters, the I_{SR} span and a wavelet are added to generate a PSDM filter. A PSF is produced from the PSDM filter by Fourier transform. d) A PSDM filter and the associated PSF which correspond to a maximum illumination angle of 45° . Notice the cross-pattern in the PSF, representing the dip-limited illumination. e) A PSDM filter and the associated PSF corresponding to a perfect illumination of 90° . Modified after Lecomte et al. (2015).

The generated PSDM filter is shown to the right in Fig. 3.6d. The filter corresponds to an angle of maximum illumination of 45° , a Ricker wavelet with a dominant frequency of 40 Hz, an average velocity of 4.7 km/s and an incident angle of 0° (zero-offset). The next step in the process is then to simulate a PSF in the spatial domain from the PSDM filter in the wavenumber domain by Fourier transform. The resulting PSF is illustrated to the left in Fig. 3.6d. The limited I_{SR} span appear as a cross pattern due to truncation effects from the simulated PSF (Lecomte et al., 2016). The PSF is accounting for resolution and illumination effects on PSDM seismic images for all reflectors (Lecomte et al., 2015), which hence results in more realistic synthetic seismic being generated. The seismic resolution induced by the PSF are about $\lambda/4$ vertically and $\lambda/2$ laterally for the 45° maximum illumination angle case.

Another usage of the generic I_{SR} span is defining a perfect illumination case which includes dips up to 90° – in other words “ideal seismic acquisition” (Lecomte et al., 2016). Fig. 3.6e illustrates a perfect illumination case of the PSDM filter and the corresponding PSF. Compared to the PSF corresponding to an angle of maximum illumination of 45° , the PSF representing the perfect illumination does not contain any cross-pattern effects. This is because the illumination is not dip-limited in this case. All reflectors will be illuminated in the resulting seismic when the angle of maximum illumination is 90° . The seismic resolution induced by the this PSF is about $\lambda/4$ both vertically and laterally. However, perfect illumination is not possible to obtain in real seismic. The angle of maximum illumination is seldom more than $40\text{-}50^\circ$, even for 3D seismic. In this study, an I_{SR} span defining a perfect illumination case is applied in the seismic modeling for the sake of comparison between ideal and realistic seismic imaging.

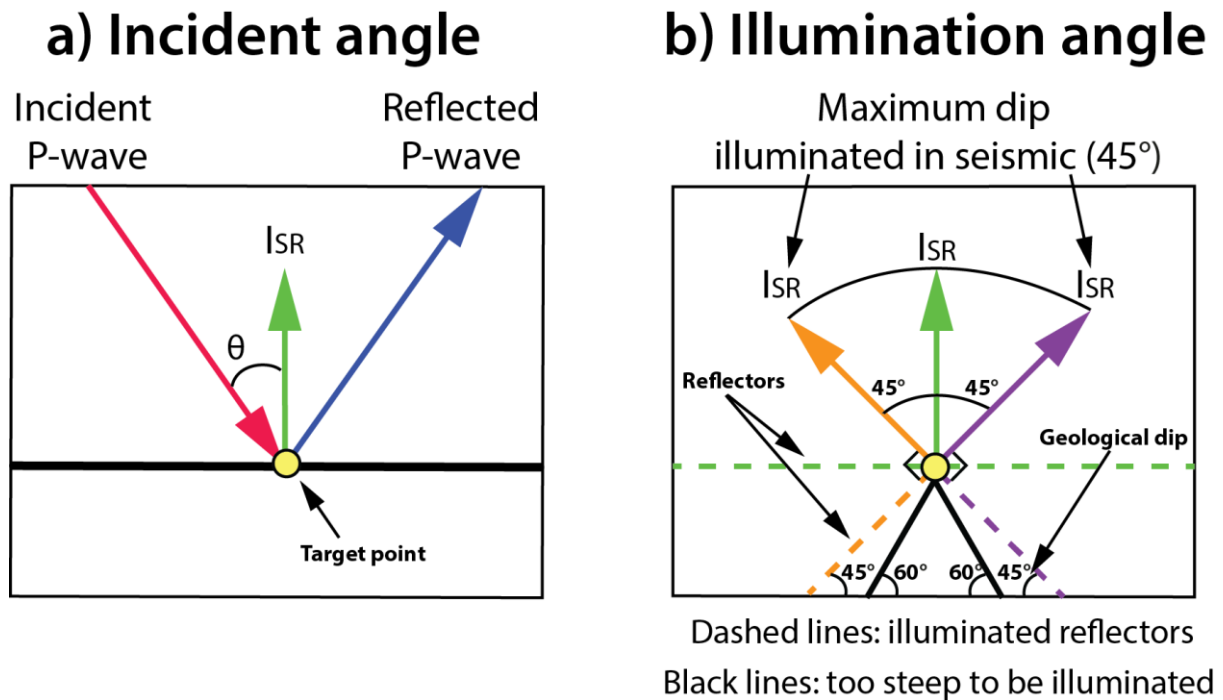


Figure 3.7: Sketches illustrating a) the incident angle (θ) of a seismic wave, and b) the illumination angle. The illumination vector (I_{SR}) span decides the maximum geological dip of reflectors that will be illuminated in the seismic. The case in b) shows a horizontal reflector (green) and four steeper dipping reflectors (orange, purple and black). The reflectors which are oriented perpendicular to one of the illumination vectors will be illuminated in the seismic (dashed lines). However, if the geological dip of the reflector exceeds the angle of maximum illumination, the reflector will not be illuminated in the seismic (black lines).

4 Data and methodology

This chapter gives an outline of the data obtained and methods applied both in the field and in the computer lab, in the process of going from outcrop to 2D synthetic seismic. The synthetic seismic images created in this thesis are built on four well-exposed cross sections of the hanging wall of the Maghlaq Fault, with sizes ranging from 80 m x 12 m to 250 m x 65 m. A workflow including each step in the process from outcrop to synthetic seismic is provided in Fig. 4.3 and Appendix A.

4.1 Field work

The seismic images generated in this study are based on outcrop data collected on the southwestern coast of Malta during a 2-week-period of field work in March 2019. The primary data collected from the four different localities were imagery captured by an unmanned aerial vehicle (UAV, i.e. a drone). The imagery was collected with the aim of building virtual outcrop models (VOMs) from photogrammetry of each hanging wall cross section of the Maghlaq Fault. The VOMs were further geologically interpreted and assigned elastic properties in order to function as input for seismic modeling at a later stage in the process. Other data obtained in the field included orientation measurements of the fault surface and detailed descriptions and sketches of the hanging wall geometry, which aided the geological interpretation of the VOMs. Additionally, lithostratigraphic data were collected at In-Neffiet (Fig. 1.1c) to make a representative stratigraphic log of the study area.

4.1.1 Stratigraphical logging

The cross section of the hanging wall at In-Neffiet was logged as it is the most accessible outcrop to get to by foot along the Maghlaq Fault. Elsewhere along the fault, e.g. Ix-Xaqqa, Ras Hanzir and Il-Miqtub (Fig. 1.1c), the cross sections of the hanging wall form steep cliffs surrounded by the ocean, making them inaccessible for sedimentological logging. The log is based on the classification scheme of Dunham (1962) for carbonate rocks, as well as field observations, i.e. particle size, grain/matrix ratio, fossil content and thickness of the layers, which are further supported by previous work done on the stratigraphy (Pedley et al., 1976; Pedley 1987, Dart et al., 1993). Due to the lack of exposure of the lithology in the footwall of the Maghlaq Fault, other than an inaccessible quarry close by Ix-Xaqqa, the footwall was not

logged, and the lithology used in the geological models for this part is purely based on stratigraphic studies from Pedley et al. (1976), Dart et al. (1993) and Bonson et al. (2007).

4.1.2 Outcrop mapping

Photogrammetric image collection is a useful mapping tool where overlapping photographs of an outcrop can be automatically processed to rapidly extract the relative 3D coordinates of surface points that are present on the overlapping photos (Bemis et al., 2014). Photogrammetric techniques are time- and cost-efficient methods to visualize inaccessible outcrops as 3D models. The only thing required in addition to a digital camera is access to a suitable software that can stitch the photographs together into an outcrop model (Bemis et al., 2014). Photogrammetric techniques and the building of a virtual outcrop model can improve the geological interpretations of an outcrop when time is limited in the field and if structures are too big to observe extensively in the field.

In this study, a DJI Mavic Pro drone was used for aerial photogrammetry to provide input data for building high-resolution 3D virtual outcrop models of the Maghlaq Fault. The drone was remotely controlled from the DJI remote-access application installed on a smartphone, which was attached to the controller. This made it easy to keep track of the distance to the outcrop and make sure the pictures gathered were significantly overlapping. A photographic overlap of 60-80% is the ideal percentage when mapping an outcrop, to get the highest quality possible of the VOM (Bemis et al., 2014). This was obtained by continuously shooting photographs while flying the drone parallel to the outcrop with the camera pointing at a 90° angle to the cross section (Fig. 4.1). The shots were captured with the drone flying at a distance between 20-60 m from the outcrop, depending on the size of the outcrop, to include the top and the bottom of the cross section in the picture frame. Small-scale structural features in the damage zone, such as fault rocks and antithetic and synthetic faults, were photographed more closely in order to obtain high-resolution photographs of these structural inputs for the geological model.

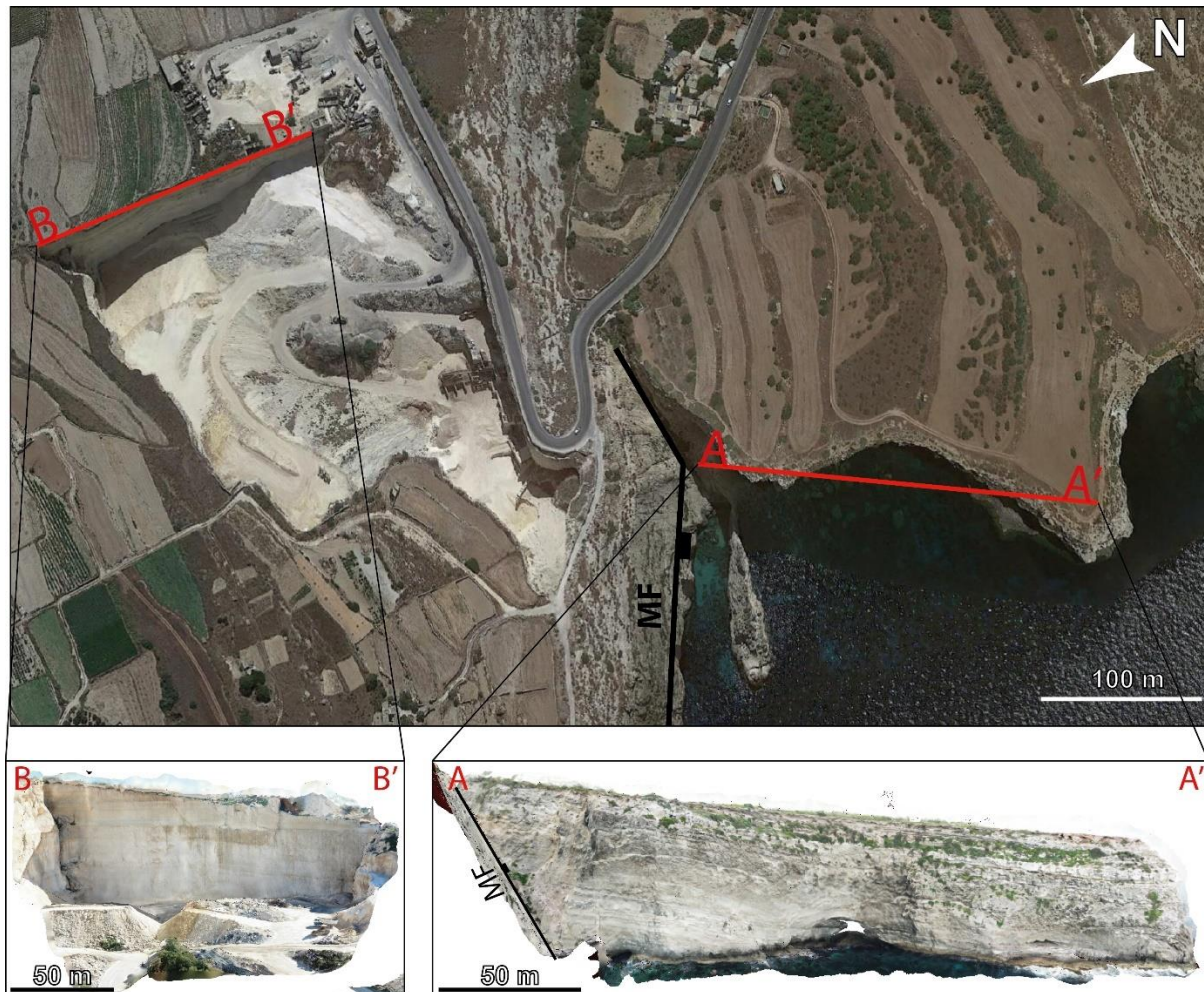


Figure 4.1: Virtual outcrop models of the outcropping footwall (B-B') and hanging wall (A-A') of the Maghlaq Fault (MF) at Ix-Xaqqa. Satellite photo in top image from Google Earth (2019).

4.2 From outcrop to geological model

4.2.1 Virtual outcrop models from photogrammetry

A large amount of georeferenced photographic data was obtained during the period of field work. Following the data collection was filtering of photographs based on quality and relevance for the 3D model. Photographs of poor resolution, poor coverage of the outcrop or bad lightning were manually filtered. The remaining photos were processed in AgiSoft Photoscan to generate a 3D virtual outcrop model, following the workflow in Fig. 4.2. This process was repeated for all photogrammetrically mapped outcrops, resulting in four VOMs of the hanging wall and a single VOM of the footwall.

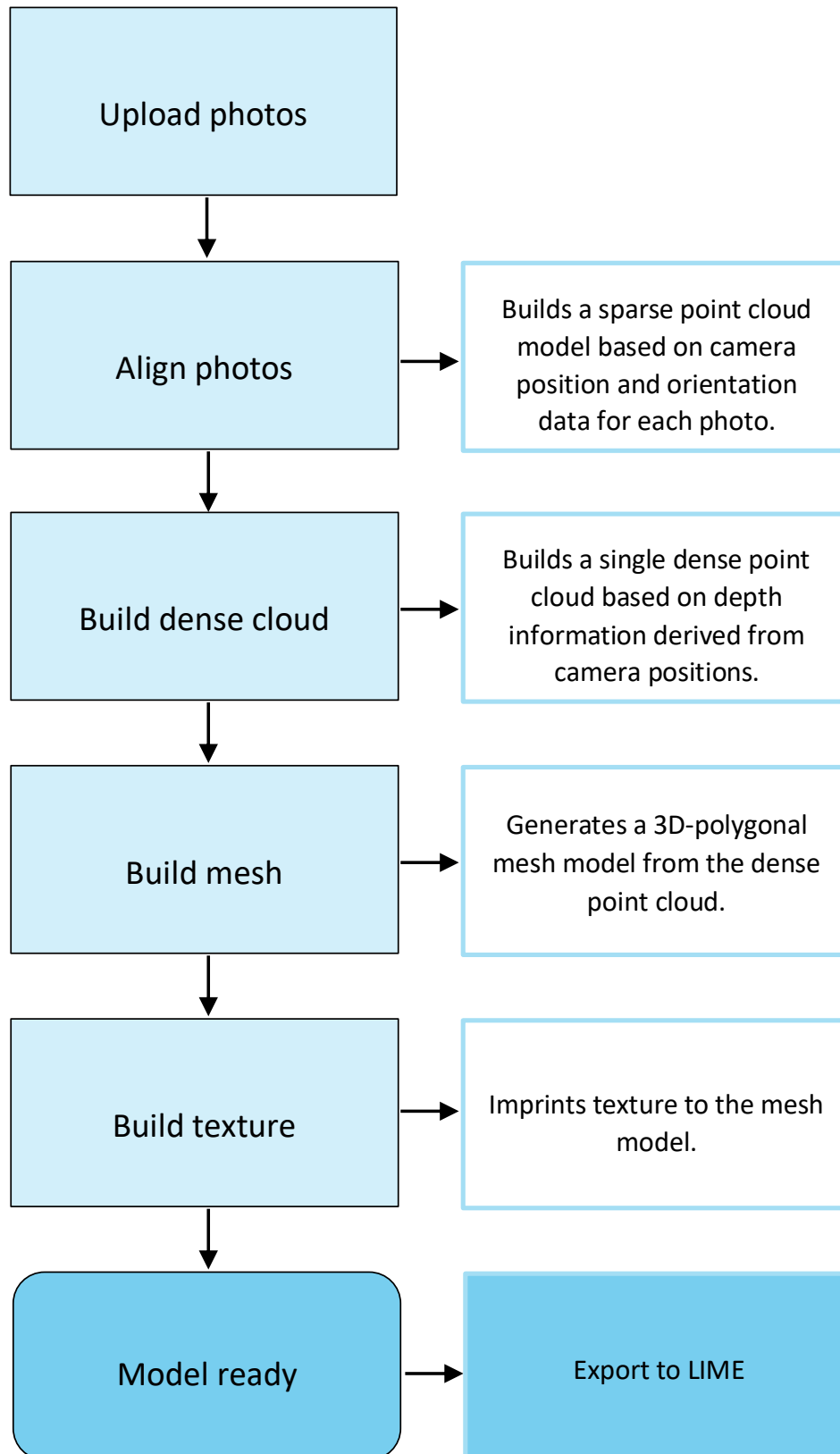


Figure 4.2: Workflow explaining the process for building a virtual outcrop model from photogrammetry in AgiSoft Photoscan.

4.2.2 Geological models

After generating a VOM, the next step in the process included a detailed structural and stratigraphic interpretation of the model, which is required in order to create 2D geological input models for seismic modeling. Geological interpretations of the 3D outcrop models were firstly performed in LIME (Buckley et al., 2019) to identify main structural features and stratigraphic boundaries. The interpretations of the VOMs were supported by outcrop descriptions, external photographs and sketches gathered in the field. The stratigraphic layers were interpreted based on lithology, geometry, color change and degree of weathering observed on the model and the associated photos. The area of greatest interest was the damage zone on the hanging wall side of the fault, as it comprises a chaotic and complex zone containing fault rocks, small-scale synthetic and antithetic faults and drag folding.

The geologically interpreted VOM was further projected onto a 2D panel and exported to a graphics editing software (e.g. Adobe Illustrator CS6 or paint.net) to fill in the geological units with color. A single geological model was created of the footwall of the Maghlaq Fault and duplicated onto the four different hanging wall models, resulting in four complete fault zone models. Furthermore, the fault and stratigraphy were extrapolated to create appropriate-size models for seismic modeling. Over- and underburden strata were added to the geological model based on local and regional stratigraphic information from Dart et al. (1993) (Fig. 2.3), Pedley et al. (1976) and Bonson et al. (2007), which provide age, thicknesses and geometry of the lithostratigraphy in the Malta region.

4.2.3 Elastic Properties

Elastic properties, i.e. seismic velocities and bulk density, determine the seismic reflection of rocks (Brigaud et al., 2010). These properties are highly dependent on the rock's mineral composition as well as texture, porosity, pore fluid content, cementation, depth of burial and the equivalent temperature and pressure at this depth (Gardner et al., 1974; Castagna et al., 1993). Big challenges are associated with building velocity models representing geology of great complexity (Fonseca et al., 2018). The interpreted layers in the footwall and hanging wall of the geological models of the Maghlaq Fault had to be assigned specific elastic properties according to their lithologies in order to do seismic modeling. The properties assigned to the models herein are presented in Table 1, and include density, P-wave and S-wave velocities.

The velocity models created in this study were based on P-wave velocities extracted from studies on seismic velocities for different lithologies, and S-wave velocities derived from geophysical ratios between the P-wave and S-wave velocities. The P-wave velocities for the carbonates, clays, sand and marls in the geological models were based on rock velocities from the studies of Bourbie et al. (1987) and Mavko (2017). The faulted and fractured carbonate rocks comprising the damage zone of the fault were given seismic velocities after the study of Agosta et al. (2007). The S-wave velocities assigned to the layers in the geological models were based on V_p/V_s -ratios, which are indicative for different lithologies. The Lower and Upper Coralline Limestone formations were given V_s -values based on a V_p/V_s -ratio of 1.9 for limestone (Miller, 1992; Castagna et al., 1993). A V_p/V_s -value of 1.7 was used for the Greensand Formation's calcareous sand, after Pickett (1963) and Miller and Stewart (1990). For the Blue Clay Formation, a higher V_p/V_s ratio of 2.13 was applied after Castagna et al. (1993) and Tosaya and Nur (1982). Finally, the S-wave velocity for the post-rift marls and clays was based on a V_p/V_s -ratio of 1.91, after Dvorkin et al. (2001).

Table 1: Input elastic properties to seismic modeling for each formation represented in the geological models of the Maghlaq Fault zone.

<i>Formation</i>	<i>Lithology</i>	V_p (km/s)	V_s (km/s)	V_p/V_s	<i>Density</i> (kg/dm ³)
Lower Coralline Limestone	Limestone	5.5-5.8	2.9-3.05	1.9	2.67-2.71
Globigerina Limestone	Limestone	3.7-4.0	1.95-2.11	1.9	2.42-2.47
Blue Clay	Clay	1.9-2.5	0.89-1.17	2.13	2.05-2.19
Greensand	Calcareous sand	3.0	1.76	1.7	2.29
Upper Coralline Limestone	Limestone	4.7-6.0	2.47-3.16	1.9	2.57-2.73
Plio-Quaternary succession	Marls & clays	2.1-2.7	1.1-1.41	1.91	2.1-2.23
Upper Coralline Limestone	Fault rock	4.3-4.8	2.26-2.53	1.9	2.51-2.58

Although relationships between rock velocities and other elastic properties in carbonates are in general complex, there is a simple and systematic relationship between the P-wave velocity and the density, called Gardner's relation (Eq. 4.1) (Gardner et al., 1974; Miller, 1992; Dey and Stewart, 1997). The density values used in this study were derived from Gardner's relation. The equation given from this relation allows for the acoustic impedance to be estimated from velocity information exclusively, when measured densities are unavailable (Gardner et al., 1974; Miller, 1992).

$$\rho = aV^{1/4} \quad (\text{Eq. 4.1})$$

Where ρ = density in g/cm^3 , $a = 0.31$ and V = P-wave velocity in km/s (Dey and Stewart, 1997; Ursenbach, 2002).

4.3 From outcrop to 2D synthetic seismic

In this study, a 2D PSF-based convolution modeling approach was used to generate synthetic seismic sections of the Maghlaq Fault. The theory behind the 2(3)D PSF-based convolution modeling approach was described in detail in Chapter 3.5.2. The four geological models with associated elastic properties were used as input models for seismic modeling in SeisRoX Pro, NORSAR software Suite 2019. Synthetic PSDM images were generated by using an analytical PSF, which contains the necessary information on geophysical parameter values. A step-by-step explanation of the workflow going from an outcrop model to 2D synthetic seismic images is provided in Fig. 4.3 and in Appendix A.

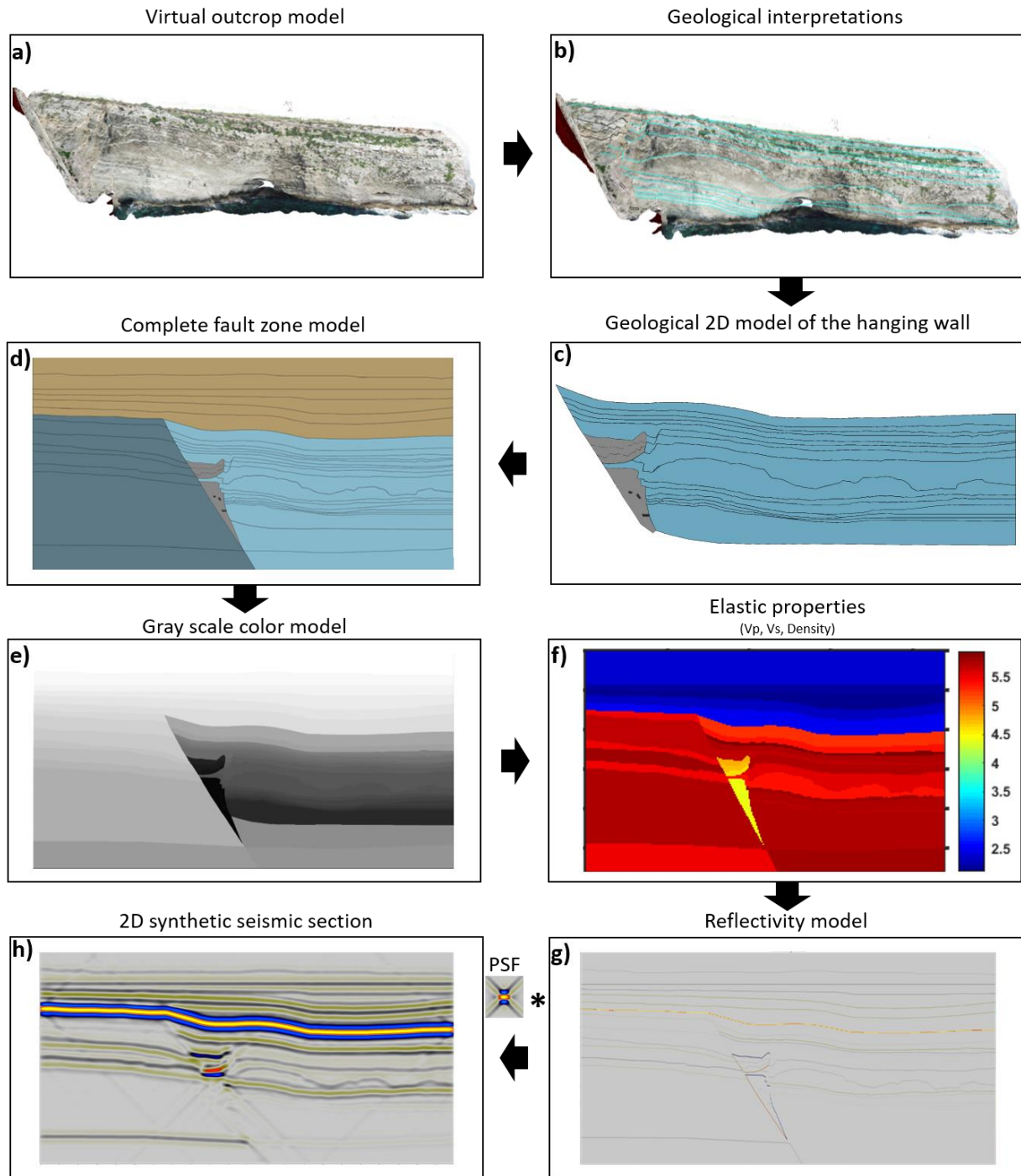


Figure 4.3: A workflow explaining the main steps going from outcrop to 2D synthetic seismic. a) A virtual outcrop model of the hanging wall of the Maghlaq Fault, which the geological model is primarily based on. b) Geological interpretations of the outcrop model performed in LIME. Main stratigraphic and structural features are identified and marked. c) The interpretation is imported into a drawing software, where the units are filled with different colors dependent on lithology. d) The geological model of the hanging wall is merged with the footwall model, and under- and overburden strata are added, resulting in a complete 2D fault zone model. e) Each unit is given a unique gray scale color in order to be mathematically identifiable in Matlab. f) Elastic properties such as P- and S-wave velocities and density are added to each layer in Matlab. Four data files are generated in this process, which are used as input property cubes in the seismic modeling software. g) A reflectivity model is generated and convolved with a Point-Spread Function (PSF) which includes information on wavelet, velocity, illumination angle and incident angle. h) The resulting 2D synthetic seismic.

4.3.1 Sensitivity study

To address the key scientific question of this thesis, a sensitivity study of the resulting synthetic seismic was conducted, investigating the effects of various geophysical parameters. This included the effects of various dominant frequencies, levels of noise, angles of maximum illumination, incident angles and wavelet types (frequency bands) on the seismic expression of the hanging wall geometry of the Maghlaq Fault. The ranges of values for the different parameters included in the sensitivity analyses are listed below. The resulting synthetic seismic sections from the sensitivity study are presented in Chapter 5.

- *Dominant frequencies (Hz):*
10, 20, 30, 40, 60, 100, 150 and 200.
- *Levels of noise (%):*
0, 25, 50 and 100.
- *Angles of maximum illumination (°):*
30, 45, 60 and 90.
- *Incident angles (°):*
0, 10 and 30.
- *Wavelet types:*
Ricker and Ormsby.

5 Results

In this chapter, the results of both the workflow “from outcrop to 2D synthetic seismic” (Chapter 4.3), and the geophysical parameter sensitivity study will be presented. Firstly, the geological interpretations of the virtual outcrop models and the associated 2D geological models are addressed, followed by a presentation of the resulting 2D synthetic seismic images. The seismic modeling results are further divided into subchapters with respect to the geophysical parameter subject to sensitivity testing.

5.1 Geological interpretations of the Maghlaq Fault zone

Five virtual outcrop models (VOMs) of the Maghlaq Fault are included in this study: one footwall model and four hanging wall models. The geological interpretations of each of the VOMs are the base of the geological input models for 2D seismic modeling. The VOMs were interpreted with the aim to identify structural fault geometries and main stratigraphic boundaries in the fault zone. The outcrop models are representative of the outcropping footwall at Ix-Xaqqa, and the hanging wall at the following localities: Ix-Xaqqa, Ras Hanzir, Il-Miqtub and In-Neffiet (Fig. 5.1). The hanging wall models are hereafter referred to as Model 1, Model 2, Model 3 and Model 4, respectively (Figs. 5.3-5.6).

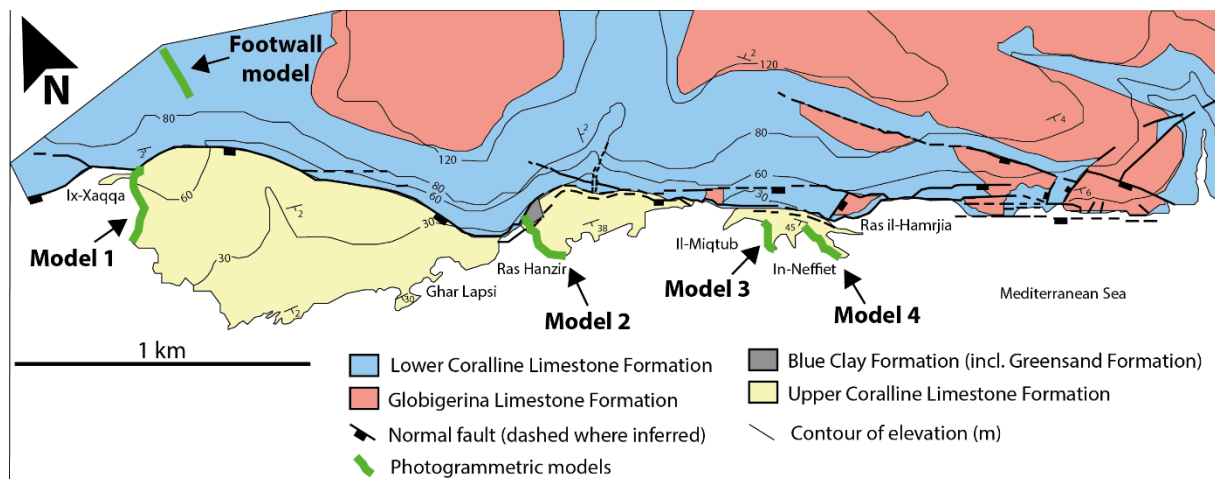


Figure 5.1: Geological map showing the studied area on the southwestern coast of Malta, where the photogrammetrically mapped footwall and hanging wall localities of the Maghlaq Fault are marked. Modified after Bonson et al. (2007).

5.1.1 Stratigraphic interpretations

The stratigraphy presented in the geological models is a combination of stratigraphic interpretations of the VOMs, which are unique for each model, and conceptual stratigraphic interpretations, which are identical for all models. The hanging wall part of the geological models is divided into three parts with respect to the activity of the fault: a pre-rift layer of Lower Coralline Limestone Formation, an early syn-rift succession consisting of Globigerina Limestone Formation, Blue Clay Formation and the occasionally occurring Greensand Formation, a late syn-rift succession of Upper Coralline Limestone Formation and an overburden of post-rift marls and clays. The footwall part of the geological models comprises a thick succession of pre-rift Lower Coralline Limestone overlain by the same overburden as in the hanging wall. The main stratigraphic differences from model to model are:

- (i) Number of stratigraphic layers included.
- (ii) Thickness variations in Globigerina Limestone and Blue Clay in Model 2, 3 and 4.
- (iii) Absence of Greensand in all models except for Model 3.
- (iv) No early syn-rift deposits present in Model 1.

The stratigraphic interpretations of the VOMs are supported by the stratigraphic logs presented in Fig. 5.2. Fig. 5.2a illustrates the overall stratigraphy of the Maltese Islands, whereas Fig. 5.2b presents the log created from the stratigraphical logging performed in the field, on the sub-vertical layers in the hanging wall of Model 4. The latter represents the lithologies, fossil content and units present in the VOM from In-Neffiet (Fig. 5.6a). This stratigraphic log includes, from bottom to top, layers of Upper Globigerina Limestone Member, Blue Clay Formation and Upper Coralline Limestone Formation. The thickness of Upper Coralline Limestone is dominating the stratigraphic log with a total of 64 m, in contrast to the 10 m thick Blue Clay and 2 m thick Upper Globigerina Limestone.

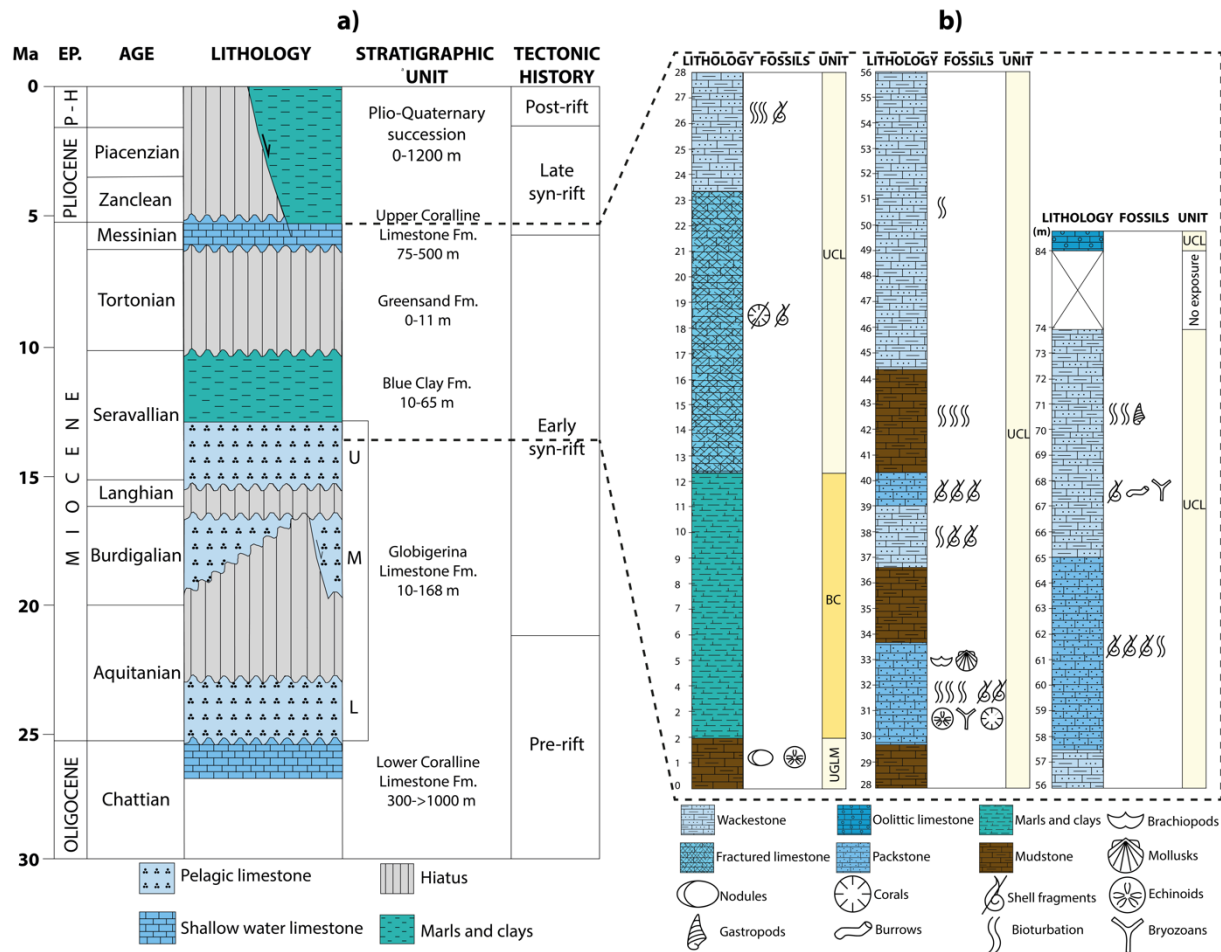


Figure 5.2: a) Lithostratigraphic log of the Maltese Islands modified after Dart et al. (1993). b) Lithostratigraphic log of the Maghlaq Fault’s hanging wall at In-Neffiet (Model 4). This log was created from stratigraphical logging performed during the period of field work on Malta. The sub-vertical layers at the locality comprise a few meters of Upper Globigerina Limestone Member (UGLM), 10 meters of Blue Clay Formation (BC) and a thick succession of Upper Coralline Limestone Formation (UCL).

5.1.2 Structural interpretations

The structural features in the geological models are, similarly to the stratigraphic interpretations, based on interpretations of the VOMs in addition to conceptual extrapolations. A structural simplification was established for all the geological models: the faulted limestone units in both the hanging wall and the footwall are bounded at the top by an unconformity. This unconformity forms a disconformity in Model 1 and angular unconformities in Models 2, 3 and 4.

The hanging wall geometry and the structural dips of the geological models are changing from west to east along the Maghlaq Fault. The VOM in Model 1 (Fig. 5.3), which is the westernmost outcrop in this study, comprises parallel strata that are predominantly oriented sub-horizontally, striking c. NW-SE, with a maximum dip of 10-20° towards S (Fig. 5.3c, right). The hanging

wall outcrop also consists of a chaotic zone of fault rock, including brecciated Upper Coralline Limestone (Fig. 5.3c, left). This zone is further cut by several small-scale antithetic normal faults. The VOM of the footwall of the fault, which is located close to the hanging wall of Model 1 (Fig. 5.1), also comprises sub-horizontal, parallel layers. Since the footwall is in general poorly exposed along the fault, except for at Ix-Xaqqa, no conclusions can be drawn for the structures in the footwall at the other hanging wall localities. As a result, the footwall model from Ix-Xaqqa is used in Models 2, 3 and 4 as well.

Advancing eastward onto the VOM in Model 2 (Fig. 5.4), a significant increase in dip of the strata is noticeable. The layers of Blue Clay and Globigerina Limestone are oriented sub-parallel to the fault's surface, striking c. E-W, with a dip of about 60° towards S, whereas the Upper Coralline Limestone layers are approximately striking E-W, with a dip of c. 40° towards S. The folded strata are occasionally cut by small-scale antithetic reverse faults (Fig. 5.4c, right). Other structural features in this outcrop include host and fault rock lenses that are smeared onto the smooth surface of the fault (Fig. 5.4c, left).

In the VOM of Model 3 (Fig. 5.5), the dip of the strata continues to increase. The layers in Model 3 are oriented parallel to the fault surface, which is striking c. NW-SE, with a dip of about 60° towards SW. The steeply dipping layers in the VOM, as illustrated in Fig. 5.5c (right), were interpreted to be part of a greater fault drag in the final geological model, which flattens out to the SW in the model. Like in the other VOMs, the layers in this model are also cut by some small-scale faults (Fig. 5.5c, left).

Lastly, the VOM in Model 4 (Fig. 5.6), which is the easternmost outcrop in this study, consists of layers with a wide range of dips. The dip of the lowermost part of the succession is similar to the dip of the fault-parallel layers in Model 3, although the dip direction has changed between these two localities, from 60° SSW in Model 3 to 60° S in Model 4. Moreover, the dips of the stratigraphic layers become progressively steeper to the S in the VOM, resulting in sub-vertical to vertical layers in the middle of the geological model (Fig. 5.6c, left). Finally, in the southernmost part of the VOM, there are locally overturned layers (Fig. 5.6c, right), which were drawn as recumbent folds in the final geological model.

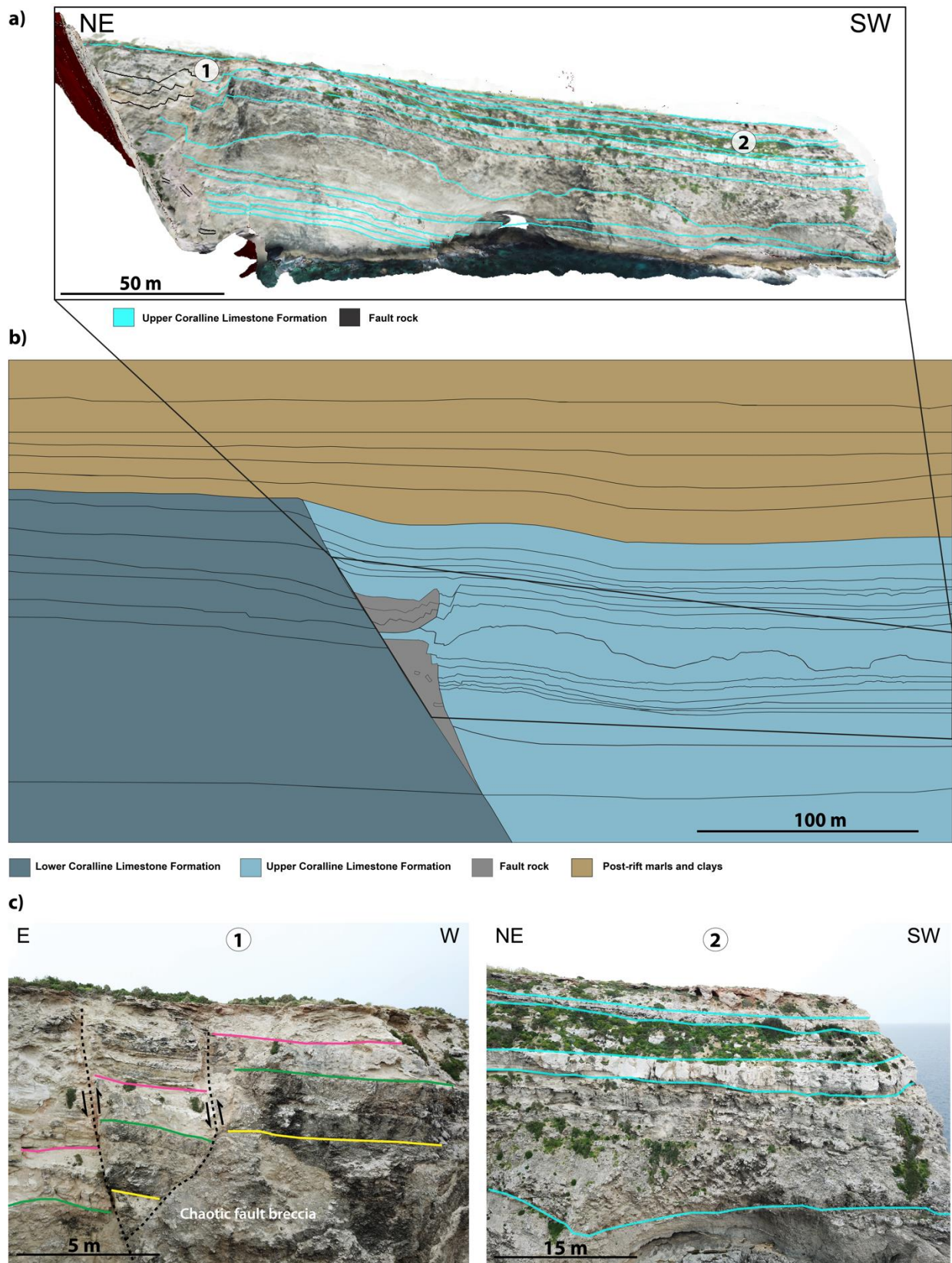


Figure 5.3: a) Virtual outcrop model with geological interpretations of the Maghlaq Fault's hanging wall at Ix-Xaqqa. b) The resulting geological model of Model 1. c) Close-ups of (1) a part of the damage zone, including small-scale faults and fault breccia of Upper Coralline Limestone Formation and (2) parallel, sub-horizontal layers of Upper Coralline Limestone Formation.

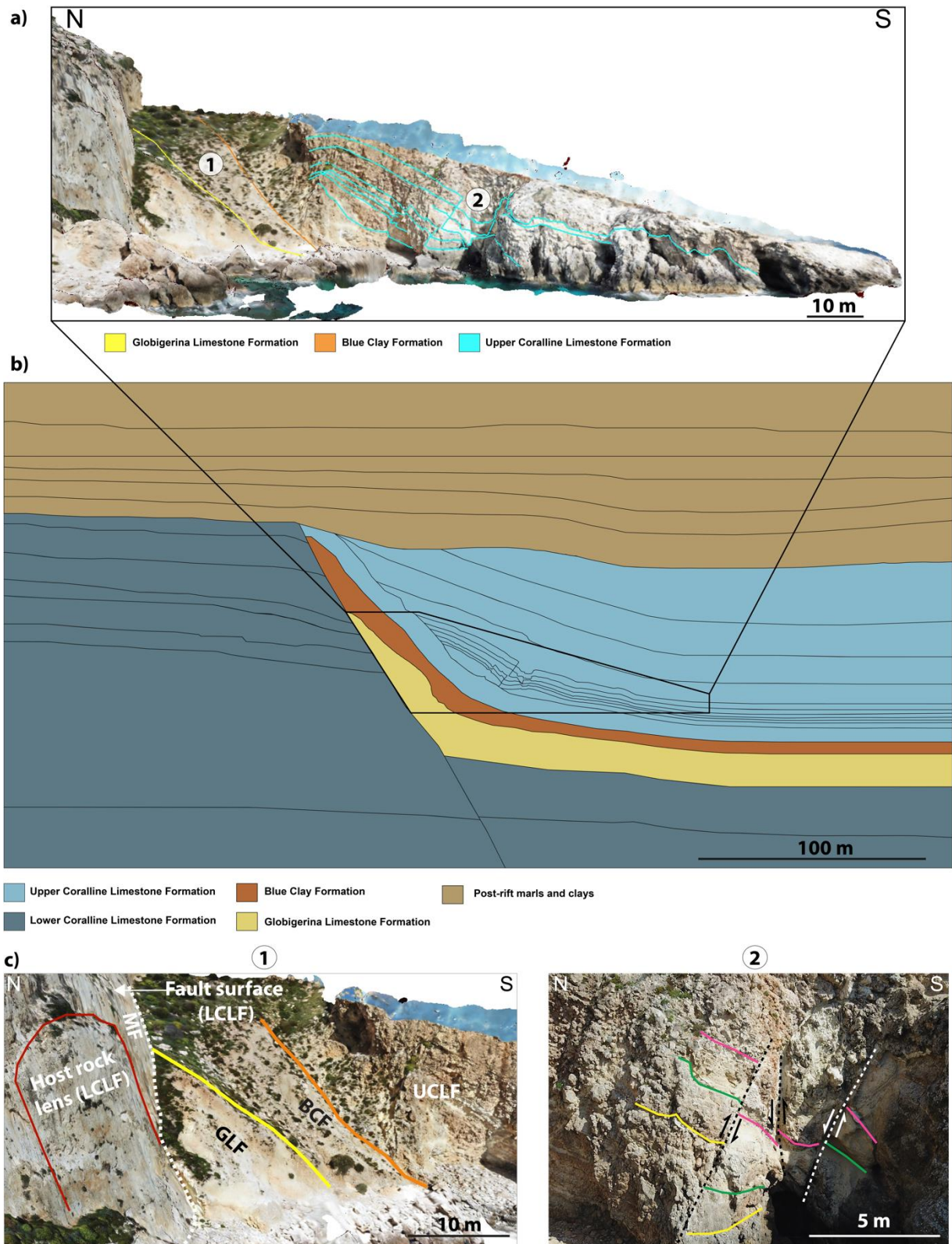


Figure 5.4: a) Virtual outcrop model with geological interpretations of the Maghlaq Fault’s hanging wall at Ras Hanzir. b) The resulting geological model of Model 2. c) Close-ups showing (1) the surface of the Maghlaq Fault (MF), a host rock lens of Lower Coralline Limestone Formation (LCLF) and the fault drag zone comprising Globigerina Limestone Formation (GLF), Blue Clay Formation (BCF) and Upper Coralline Limestone Formation (UCLF). (2) Small-scale synthetic and antithetic faults within the Upper Coralline Limestone Formation.

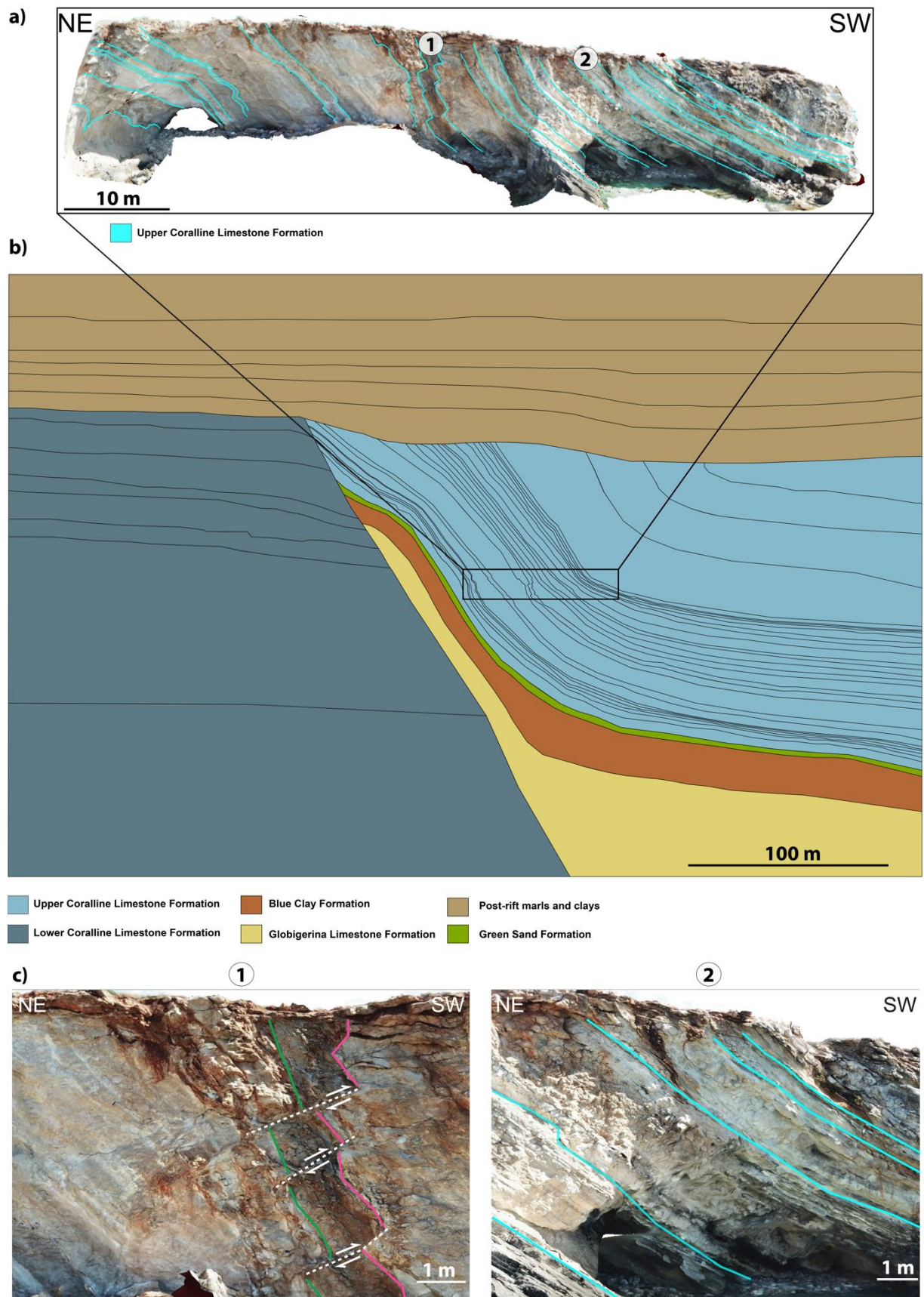


Figure 5.5: a) Virtual outcrop model with geological interpretations of the Maghlaq Fault's hanging wall at Il-Miqtub. b) The resulting geological model of Model 3. c) Close-ups of (1) small-scale faults, and (2) steeply dipping layers of Upper Coralline Limestone Formation.

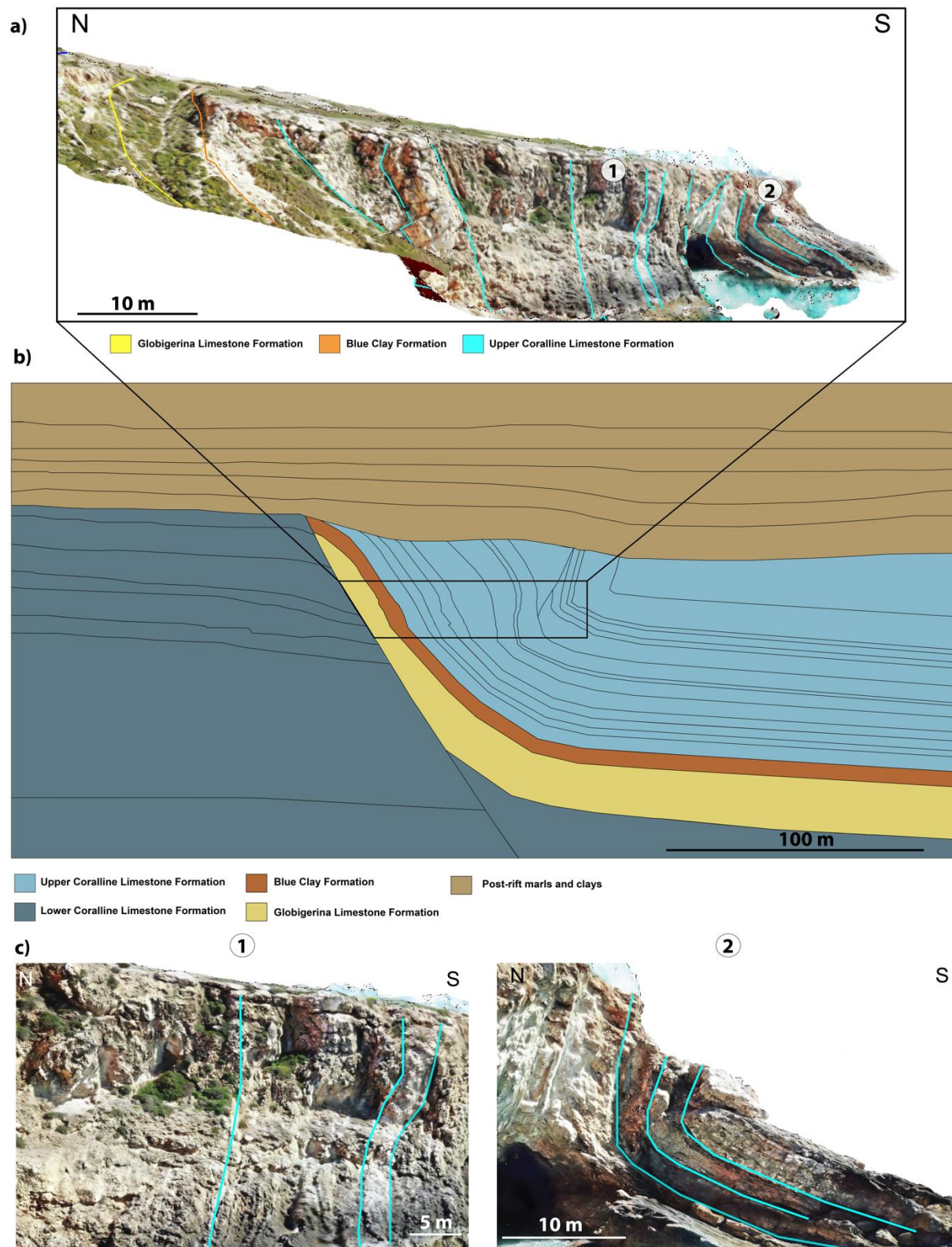


Figure 5.6: a) Virtual outcrop model and geological interpretations of the Maghlaq Fault's hanging wall at In-Neffiet. b) The resulting geological model of Model 4. c) Close-ups of (1) vertical to sub-vertical layers and (2) locally overturned structures forming recumbent folds within the Upper Coralline Limestone Formation.

5.2 Seismic modeling results

The aims of this seismic modeling study are to investigate the seismic signature of a carbonate-dominated fault zone, and to determine the effects of various geophysical parameters on the 2D seismic images of the fault. The 2D PSF-based convolution modeling approach applied in this study is a method that allows for changes and analysis of various parameters affecting the resolution and illumination of the seismic data (Lecomte et al., 2015, 2016). In this subchapter, the generated synthetic seismic sections will be presented, where the sensitivity of the seismic images to the following parameters has been tested:

- i) Dominant frequency
- ii) Level of noise
- iii) Angle of maximum illumination
- iv) Incident angle
- v) Type of wavelet (frequency band)

The majority of the structural and stratigraphic details interpreted from the hanging wall VOMs are of sub-seismic scales and would not be resolved in seismic due to resolution limitations. However, because faults and fault zones are fractal structures (Walsh and Watterson, 1993; Scholz and Aviles, 2013), meaning they appear on a range of scales from mm to km, it is reasonable to enlarge the geological input models for seismic modeling. Accordingly, the geological models were conceptually upscaled five times their original size to replicate a seismic-scale fault zone. Furthermore, for ease of comparison between the input model and the resulting seismic, the synthetic seismic images in the following sections are presented alongside with the geological input model and the associated reflectivity model.

5.2.1 Changing the dominant frequency

The frequency band and spectrum of a seismic wavelet is one of the geophysical parameters primarily controlling the resolution of a seismic image. The frequency band should ideally range from very low to the highest possible frequencies. In this section, Ricker wavelet frequency bands of both conventional-resolution seismic data and high-resolution seismic data were applied. The Ricker wavelet has a narrow frequency band and is hence commonly described by its dominant frequency. This is further described in section 5.2.5, where seismic modeling with an alternative wavelet is presented. TopSeis (Vinje et al., 2017) and high-resolution P-Cable seismic (Planke et al., 2009; Petersen et al., 2010) are examples of seismic

surveys delivering excellent broadband seismic imaging. TopSeis allows for imaging of shallow to intermediate targets (up to 3000 m) using frequencies ranging from 2.5-200 Hz (Vinje et al., 2017), whereas the P-Cable 3D seismic system provides imaging with frequencies from 20-250 Hz (Petersen et al., 2010). Accordingly, the synthetic seismic images in this thesis were modeled with the following as dominant frequencies for the Ricker wavelet: 10, 20, 30, 40, 60, 100, 150 and 200 Hz. 10-30 Hz are considered to be equivalent to conventional-resolution seismic, while 40-200 Hz are considered as the equivalent to high-resolution seismic, e.g. TopSeis and P-Cable seismic data.

Out of the four geological models created in this thesis, Model 1 and Model 2 were used for seismic modeling with various dominant frequencies of the Ricker wavelet. Fig. 5.7 displays the effects of changing the dominant frequency of the Ricker wavelet on a range from 10-100 Hz for synthetic seismic of Model 1. Moreover, Fig. 5.8 presents synthetic seismic of a zoomed-in part of Model 2, modeled with Ricker wavelets with dominant frequencies on a range from 40-200 Hz. For the sake of comparison between the seismic of different dominant frequencies, the maximum illumination angle was set to 45° in all cases, which corresponds to standard seismic illumination (Simm and Bacon, 2014; Rabbel et al., 2018). The angle of incidence was further set to 0° to simplify.

In Fig. 5.7 all the synthetic seismic images contain a coherent, strong reflection in the upper part of the sections. This reflection corresponds to the reflector attached to the boundary between the marls and clays of the overburden and the faulted limestone formations below. This high amplitude results from the high contrast in acoustic impedance between the lithologies, as the seismic velocities and densities change from very low in the overburden, to very high for the faulted limestones (Table 1). In the 10 Hz Ricker wavelet case (Fig. 5.7c), the poor resolution causes the distinct overburden reflection to dominate the seismic image. This makes it hard to detect the surface and damage zone of the Maghlaq Fault. However, the geometry of the fault on seismic changes in response to the increased dominant frequency. As the dominant frequency increases, the seismic resolution improves significantly, and the heterogeneity within the damage zone starts to be resolved in the seismic. The seismic resolution is indicated by the PSF in the bottom left corner of each seismic image. In this case, a Ricker wavelet of at least 20 Hz (Fig. 5.7d) is necessary to resolve some of the internal variations in the fault zone.

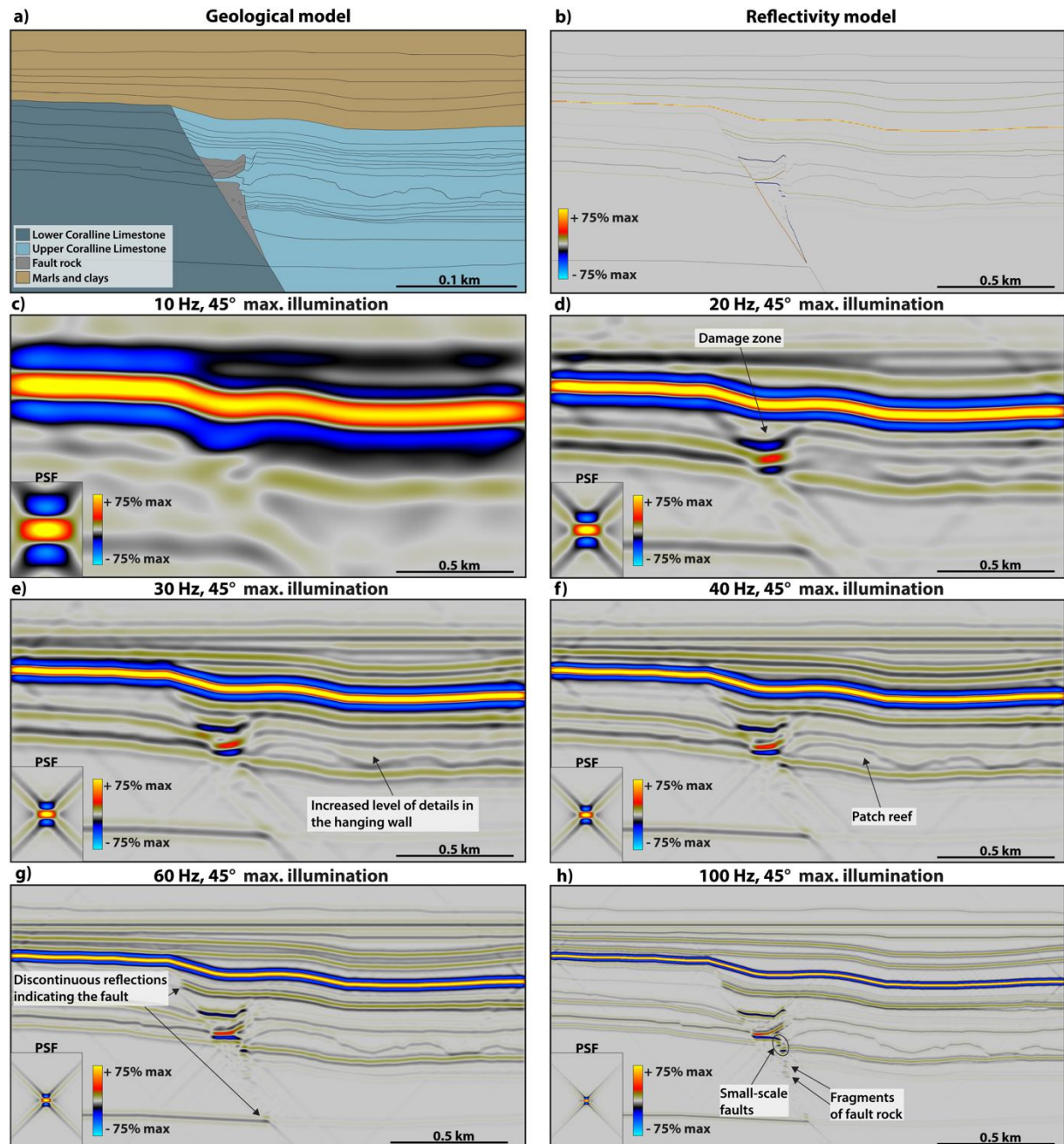


Figure 5.7: Synthetic seismic of Model 1 with different dominant frequencies on a range from 10 - 100 Hz of Ricker wavelets. The PSFs indicate the 2D seismic resolution of the seismic images. The color bar shows the relative color scale of amplitudes where the maximum values are absolute.

When the frequency is further increased to 30 Hz (Fig. 5.7e), the hanging wall geometry is resolved with a higher level of detail. In the 40 Hz seismic image (Fig. 5.7f), internal variations within the formations are easily detectable, such as the uneven layer of patch reef deposits. The level of details resolved in the synthetic seismic continues to increase as the frequencies become higher. Finally, in the seismic images of 60 Hz (Fig. 5.7g) and 100 Hz (Fig. 5.7h), almost all of the stratigraphic layers are resolved in the hanging wall, the footwall and the overburden.

Additionally, small-scale structural features, i.e. antithetic faults (as marked in Fig. 5.3c) and fragments of fault rock, are possible to identify in the synthetic seismic of 100 Hz.

The high-resolution synthetic seismic (40-100 Hz) resolve more details from the geological model than conventional-resolution seismic (10-30 Hz), although not all of the stratigraphic layers included in the geological input model can be identified as individual layers in the high-resolution seismic – not even for the 100 Hz case. Moreover, the surface of the fault forms a strong amplitude in the reflectivity model (Fig. 5.7b), yet it is not visible in the seismic. This is an issue related to the dip-limited illumination angle (maximum 45° in this case), which will be addressed in section 5.2.3. Nevertheless, the fault can be identified by the discontinuous reflections pointed out in Fig. 5.7g. These reflections represent the reflectors corresponding to layers which have been displaced by the fault. The discontinuity of the reflections is detectable with a frequency of minimum 30-40 Hz and becomes more distinct as the dominant frequency is further increased.

Fault imaging in high to very high-resolution seismic data is addressed in Fig. 5.8. This figure illustrates the impacts of an increased dominant frequency on the seismic image of small-scale faults in Model 2. These faults are corresponding to the interpretation displayed to the right in Fig. 5.4c. The dominant frequencies applied in this case include 40, 60, 100, 150 and 200 Hz of Ricker wavelets. Three small-scale faults are marked in the gray-scale geological input model in Fig. 5.8a, where (1) represents an antithetic reverse fault with a maximum displacement of 4 m, (2) points out an antithetic reverse fault with a displacement of about 1 m, and (3) represents a synthetic normal fault with a displacement of 2 m. As the seismic images are upscaled five times the original size of the geological input model, the actual displacements of the faults in the seismic are: (1) 20 m, (2) 5 m and (3) 10 m.

The numbers indicating the three small-scale faults in the model are added to the seismic images when the corresponding faults are resolved in the synthetic seismic as the dominant frequency increases. In Fig. 5.8b, where a frequency of 40 Hz was used, fault (1) is detectable from the small offset of the positive reflection in the center of the image. When the frequency is increased to 60 Hz (Fig. 5.8c), the same reflection is further downthrown by the fault. As the frequency continuously increases and more reflectors are resolved, the offset from fault (3) appears in the synthetic seismic modeled with 100 Hz (Fig. 5.8d) and 150 Hz (Fig. 5.8e). Finally, the seismic image modeled with a dominant frequency of 200 Hz (Fig. 5.8f) provides excellent seismic

resolution, where all three faults are resolved and can be identified from the downthrown reflections.

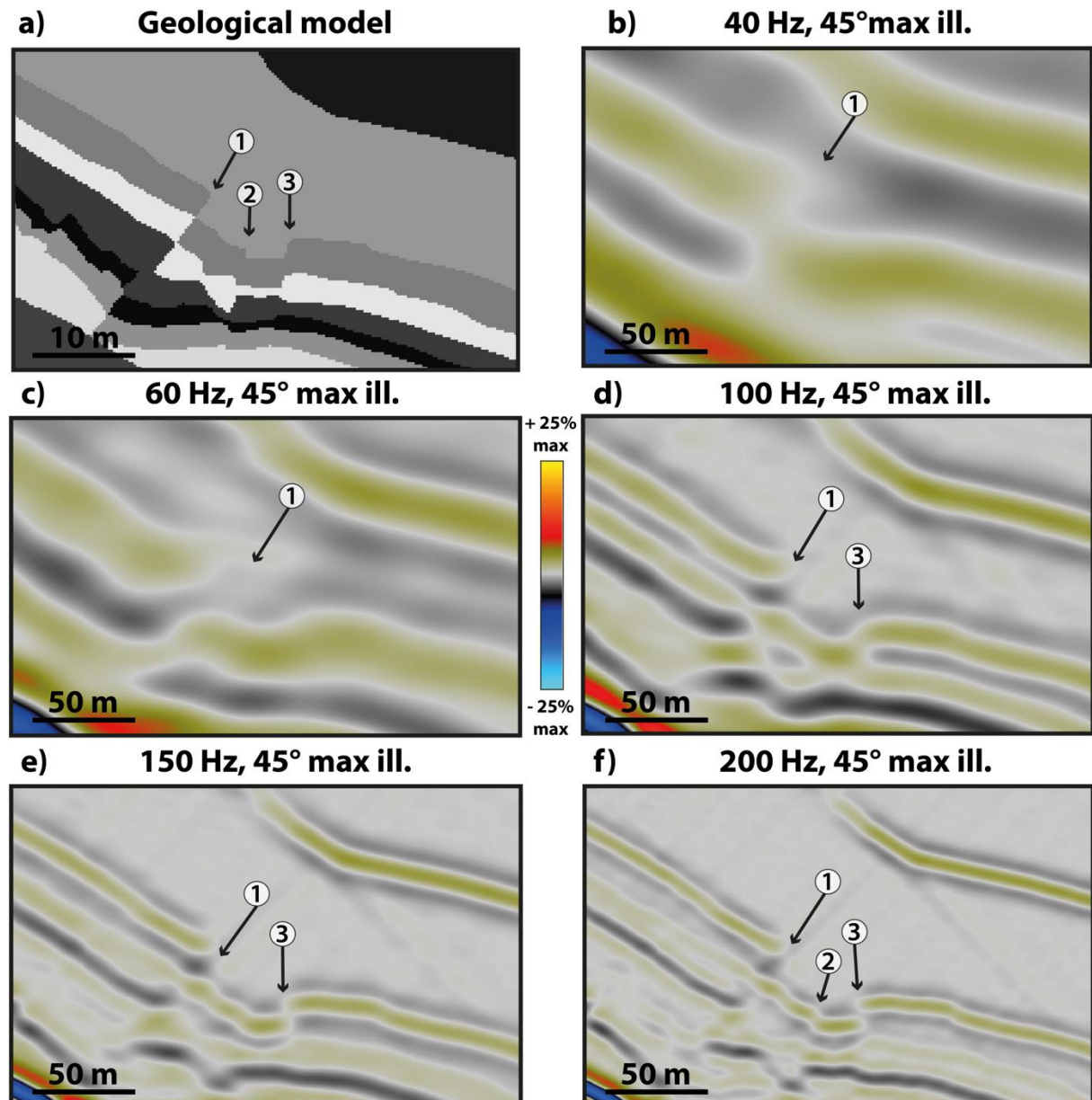


Figure 5.8: Synthetic seismic images of a close-up section of Model 2, showing three small-scale faults with displacements from 5-20 m (1-4 m in a) the original geological model), modeled with different dominant frequencies on a range from 40-200 Hz of Ricker wavelets. The geological input model is presented in gray colors to better visualize the structural input. This zoomed in area of Model 2 is marked in Fig. 5.14, which also provides a legend. The color bar shows the relative color scale of amplitudes where the maximum values are absolute.

5.2.2 Adding noise

Real seismic data contain a combination of signal and noise. For that reason, colored random noise was added to the synthetic seismic image of Model 1, following the same procedure as in Lubrano-Lavadera et al. (2018). The level of noise was systematically increased in the seismic

images to investigate the impact of noise on fault imaging. Including a noise pattern in the models produces synthetic seismic with more realistic seismic effects. In addition, this analysis illustrates the effects of interference between real seismic signals and noise.

Fig. 5.9 displays the reflectivity of the geological model, the reflectivity of the input noise and a combination of the two. When combining these two reflectivity models, it is noticeable that the strong, continuous reflector, representing the formation boundary between the overburden and the underlying limestone fault zone, is not masked by the random noise. On the contrary, the rest of the reflectors in the geological model are completely masked by the reflectivity of the noise. Accordingly, the seismic in Fig. 5.9d, which is corresponding to the reflectivity of the random noise, is considered as a noise level of 100%, even though it will not mask the strongest reflector in the reflectivity model of Model 1.

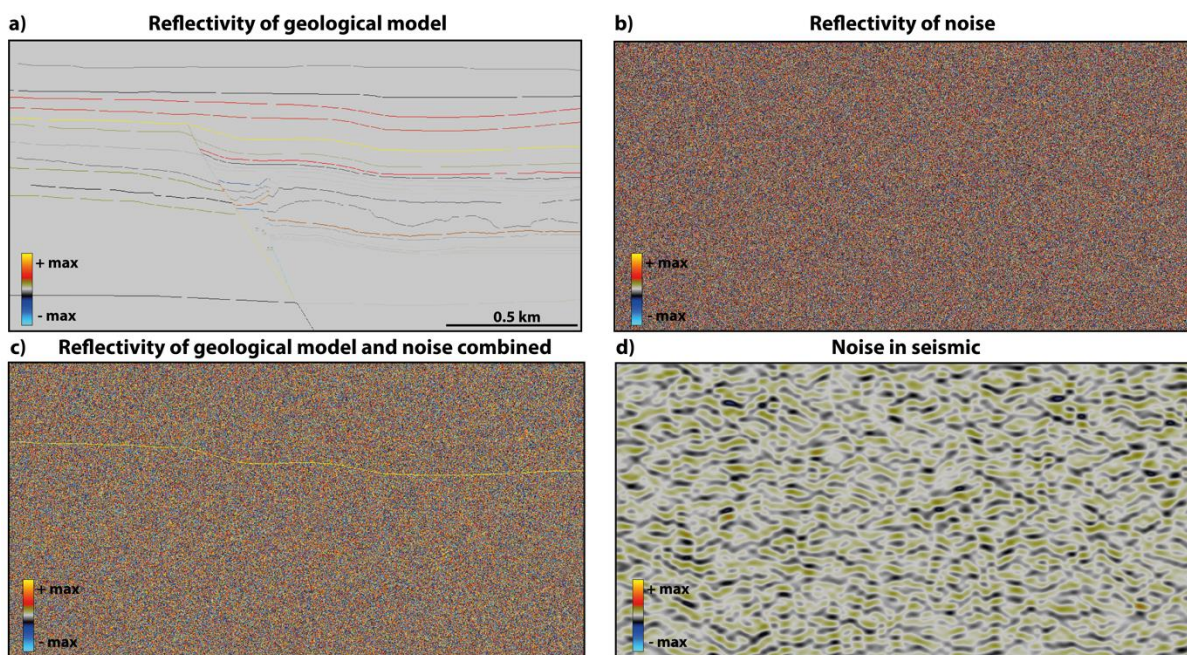


Figure 5.9: Reflectivity models of a) Model 1 and b) colored random noise. c) The reflectivity models in a) and b) combined. d) The seismic image of the input noise, corresponding to the reflectivity in b).

The effect of noise on the synthetic seismic of the Maghlaq Fault is illustrated in Fig. 5.10. The different levels of noise that have been used in this section are the following: 0%, 25%, 50% and 100%, where the latter corresponds to the seismic in Fig. 5.9d. In Fig. 5.10a, the seismic section is displayed without noise and is thus identical to the model presented in 5.6f, which is modeled with a 40 Hz Ricker wavelet, an angle of maximum illumination of 45° and a vertical incident angle. These geophysical parameters are fixed for the other seismic images in Fig. 5.10

as well, in order to clearly illustrate the impact of an increased level of noise on the seismic signature of the fault and the associated damage zone.

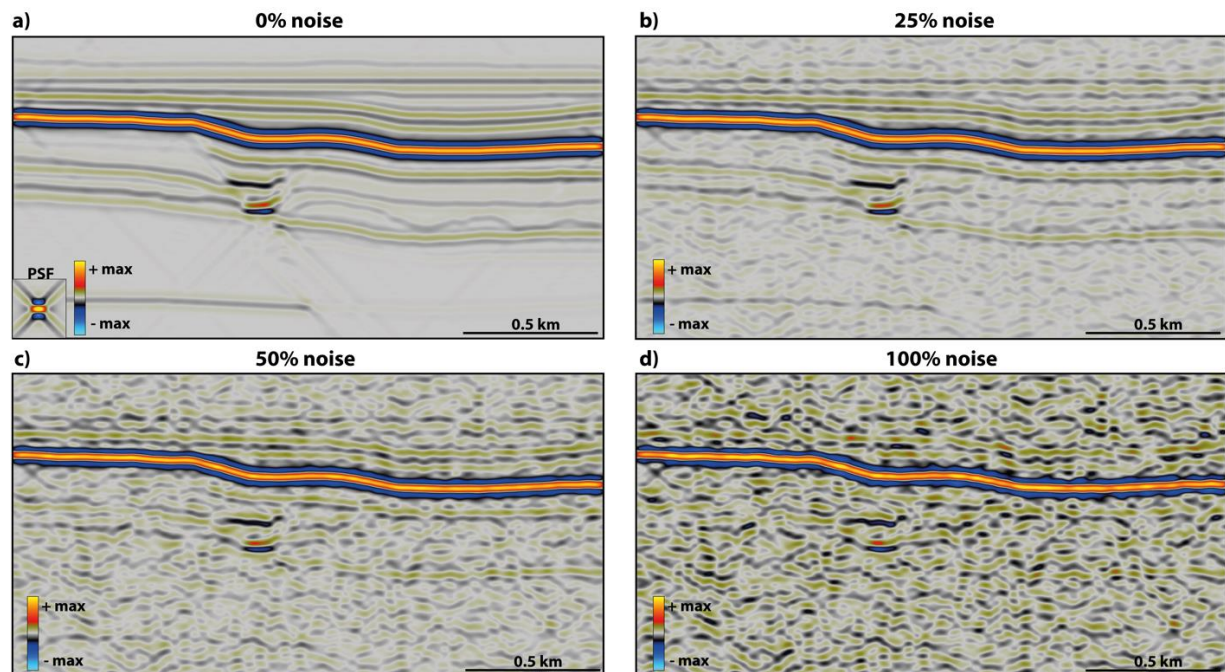


Figure 5.10: Synthetic seismic images of Model 1 where the level of random noise is systematically increased (0%, 25%, 50% and 100%). The geological model is presented in Fig. 5.6, and the reflectivity of Model 1 and the input noise, as well as the seismic of 100% noise, is presented in Fig. 5.9.

The increase of noise in the seismic results in a chaotic seismic signature of the fault zone. Adding 25% of noise to the seismic produces an image where the internal layering in the footwall and hanging wall cannot be identified in detail (Fig. 5.10b). Contrarily, the damage zone in the center of the model, forming strong seismic reflections, remains easily detectable, despite the surrounding noise. In Fig. 5.10c the level of noise is increased to 50%, reducing the distinct seismic expression of the damage zone. Further increasing the noise to 100% results in a chaotic seismic image where internal structures cannot be distinguished from each other at all (Fig. 5.10d).

5.2.3 Changing the angle of illumination

The Maghlaq Fault and some of its fault-related structures, i.e. fault drag and small-scale antithetic and synthetic faults, have steep dips which are difficult to image in seismic. The detectability of these structures is determined by their reflectivity and the maximum illumination angle of the seismic data. In seismic modeling, the latter is defined by the span of the illumination vector (I_{SR}), which is included in the PSF. The aim of this sensitivity analysis is to investigate the correlation between the maximum angle of illumination of the seismic

survey and the maximum geological dip in the fault zone that can be imaged in the seismic data. Models 3 and 4 were used for this analysis, as they comprise steeply dipping features with dips ranging from of 60-85°.

Maximum illumination angles applied in this study include 30, 45, 60 and 90°, which are considered as low, intermediate (corresponding to a standard seismic illumination), high and perfect illumination, respectively. The majority of layers in the hanging wall of Model 3 are oriented parallel to the fault surface, which has a dip of 60° towards SSW. Consequently, these features are not expected to be illuminated in the seismic images generated with a dip-limited illumination angle of 30 and 45°. Similarly to the other sensitivity analyses, the other geophysical parameters in this case are fixed to simplify, including a dominant frequency of 40 Hz Ricker wavelet and a vertical incidence.

The resulting synthetic seismic of Model 3, modeled with a maximum illumination angle from 30-90°, are presented in Fig. 5.11. The true dips of the fault and the geological units are represented by the geological model (Fig. 5.11a). As expected, the Maghlaq Fault shows great variations in seismic signature as the angle of maximum illumination increases. The primary changes in the seismic from the increased illumination capacity are an improved lateral resolution, and thus also more visible features in the fault zone. Furthermore, the geometrical appearance of the fault, its surface and hanging wall geometry is significantly changing.

Firstly, the seismic section modeled with a low illumination of 30° does not contain the surface of the fault (Fig. 5.11c), although the location of the fault can be traced from the discontinuity in seismic reflections in the footwall. (1), (2) and (3) in the figure point out discontinuous reflections in the footwall that are cut off by the more steeply dipping layers in the hanging wall. Contrarily to the fault surface, the folded layers in the hanging wall are partly illuminated, although the orientation deviates from the true dip of the layers, as a consequence of the dip-limited illumination with its impact on the lateral resolution and the specific cross-pattern. For instance, the seismic reflection of the reflector corresponding to the boundary between Upper Coralline Limestone and Greensand is highly discontinuous, forming two separate reflections, both marked with (4) in the figure. These two reflections would most likely not be interpreted as the same formation boundary due to the difference in their seismic signatures. In addition, interference is generated between the reflection of the very thin layer of Greensand and the thicker layer of Blue Clay below, increasing the likelihood of seismic misinterpretations.

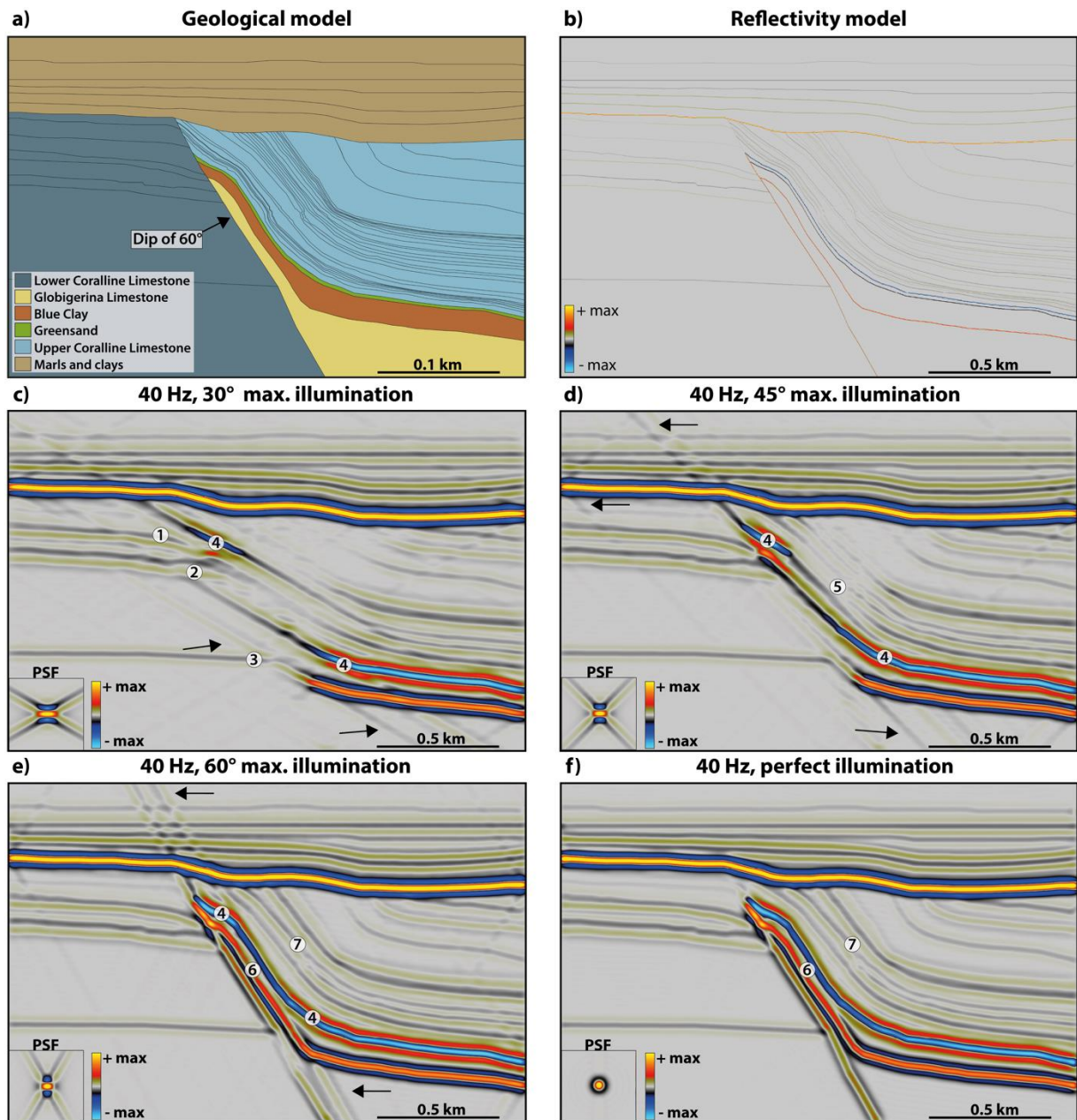


Figure 5.11: Synthetic seismic of Model 3, showing the effect of a varying angle of maximum illumination from 30-90°. The true geological dips of the fault and the steepest part of the folds are 60°, which are indicated in a) the geological model. b) shows the reflectivity model, and c)-f) display the resulting seismic images. The numbers in the seismic images point to features which are described in the text, whereas the black arrows point to seismic artefacts resulting from the dip-limited illumination.

The illumination of the folded layers in the hanging wall is moderately improved with an increase in maximum illumination angle up to 45° (Fig. 5.11d). This intermediate illumination is a good approximation to standard seismic illumination. Therefore, this synthetic seismic image possibly illustrates more realistic seismic effects than the other illumination cases. Similarly to the low illumination case, the fault is not illuminated with its true dip in this case either, as the dip of the surface (60°) exceeds the angle of maximum illumination (45°).

Moreover, in the 45° maximum illumination angle case, more layers in the hanging wall are resolved (5) than in the 30° maximum illumination case, though still not with their true dips. The formation boundary between Upper Coralline Limestone and Greensand is still illuminated as two separate reflections in this model (4).

Finally, in the synthetic seismic modeled with a high (60°) and perfect (90°) illumination (Figs. 5.11e and f, respectively), the surface of the fault and the steeply dipping layers in the hanging wall are imaged with their true dips, as marked by (6) and (7). However, not all the reflectors in the hanging wall, corresponding to the drag folded geological layers, are detectable in the resulting seismic section. This is primarily a seismic resolution issue, which was addressed earlier in this chapter.

All the seismic sections, except for the perfect illumination case, contain seismic artefacts in the form of cross-patterns, as pointed out with black arrows in Figs. 5.11c-e. These seismic artefacts are resulting from truncations effects from the dip-limited maximum illumination, which appear as cross-patterns when the PSDM filter is converted into a PSF (as described in subchapter 3.5.2). The cross-patterns for each dip-limited I_{SR} span are indicated by the PSFs, and appear on the synthetic seismic from the convolution between the PSF and the reflectivity model. This artefact appears not only in synthetic seismic images, but also in real seismic data, though it might be stronger than in reality for the synthetic seismic due to the lack of noise. In Fig. 5.11, the cross-pattern effects are especially emphasized because of the lack of structural details in some parts of the model.

Fig. 5.12 shows the effects of a dip-limited illumination on the synthetic seismic of a zoomed-in part of Model 4. This part of the model is structurally interesting, comprising folded layers with dips ranging from 45 to 85°. The seismic section in Fig. 5.12b illustrates that the fault surface, the overturned layer, and the recumbent folds are not illuminated when the maximum illumination angle is 45°. When the illumination angle is further increased to 60° it is possible to identify both the surface of the fault and the locally overturned structure, as pointed out in Fig. 5.12c. In a perfect illumination case, as illustrated by Fig. 5.12d, the recumbent folds are finally illuminated. In other words, the features which are only visible in seismic when the illumination is perfect would not be possible to identify from real seismic data with a standard maximum illumination angle of 40-50°.

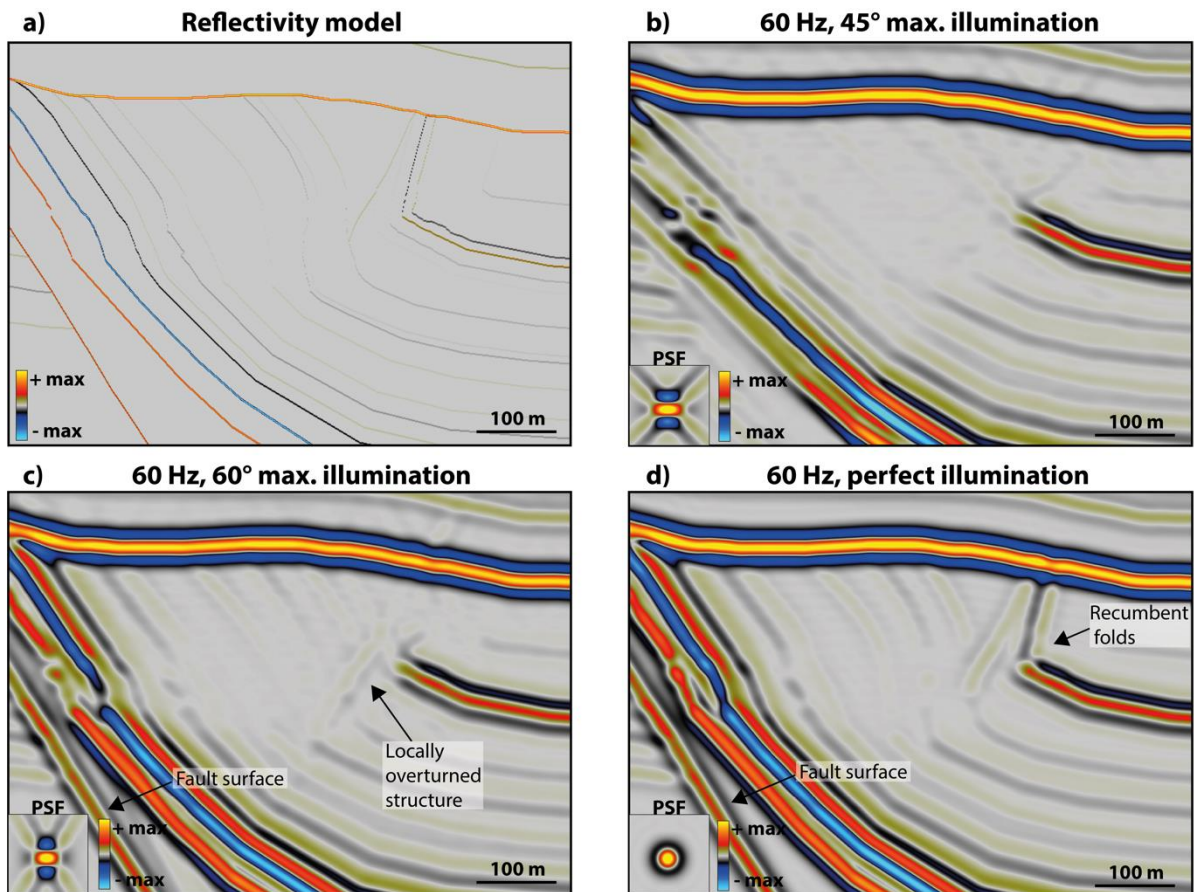


Figure 5.12: Synthetic seismic of a zoomed-in part of Model 4 (Fig. 5.6), where the maximum illumination angle is varied from 45°, via 60° to 90° (perfect illumination). The PSF is indicating the 2D seismic resolution and dip-limited illumination. A Ricker wavelet of 60 Hz and vertical incidence are applied in all cases.

5.2.4 Changing the angle of incidence

Both the reflectivity and seismic resolution are dependent on the angle of incidence of the seismic ray. Consequently, the PSDM seismic images are also incident angle-dependent, because they result from a combination of the reflectivity and the resolution (Lecomte, 2008; Rabbel et al., 2018). The effect of a non-vertical incident angle is also referred to as amplitude versus offset/angle (AVO/AVA) (Lecomte, 2008). Fig. 5.13 illustrates the AVO/AVA effect, where the reflectivity of a reflector changes as a response to an increasing angle of incidence. The presented reflectivity is described by the acoustic impedance contrast, or change in elastic properties (velocity and density), between the geological layers above and below the reflector. The reflector in the figure below corresponds to the boundary between the marls and clays in the overburden and the massive limestones of the fault zone in Model 2.

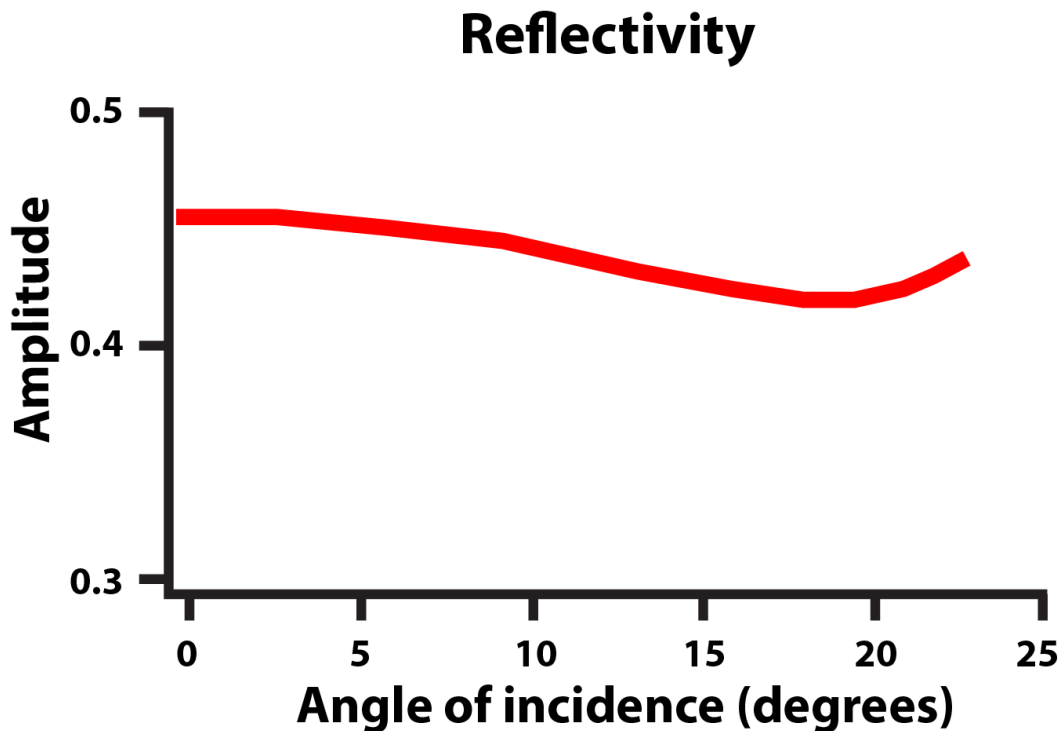


Figure 5.13: The effect of an increased angle of incidence on the reflectivity. The reflector represented in this plot corresponds to the boundary between of the low-velocity marls and clays in the overburden (V_p of 2.5 km/s) and the high-velocity limestones below (V_p of 5.5 km/s) in Model 2.

In this seismic modeling case, incident angles of 0, 10 and 30° were applied, to illustrate the changes in seismic resolution as a function of the angle of incidence. Fig. 5.14 presents the synthetic seismic of Model 2, modeled with these various incident angles. A 40 Hz Ricker wavelet and a maximum illumination of 45° were used for all cases. The resulting synthetic seismic show that the reflector geometry of the fault zone is overall very similar in all images despite the differences in incident angle. However, there are some minor changes in the seismic as a result of the varied incident angle. As the angle of incidence increases from 0° or 10° to 30°, the seismic resolution decreases both vertically and laterally. This is recognizable from both the synthetic seismic images and the PSFs. When comparing the zero-offset case in Fig. 5.14b to the 30° incident angle case in Fig. 5.14d, the lateral resolution in the zone of drag folding adjacent to the fault plane is to some degree poorer. The reduced resolution in the vertical direction is further noticeable from both the thickening and the disappearance of some horizontal reflections, as pointed out by black arrows in the 30° incident angle case.

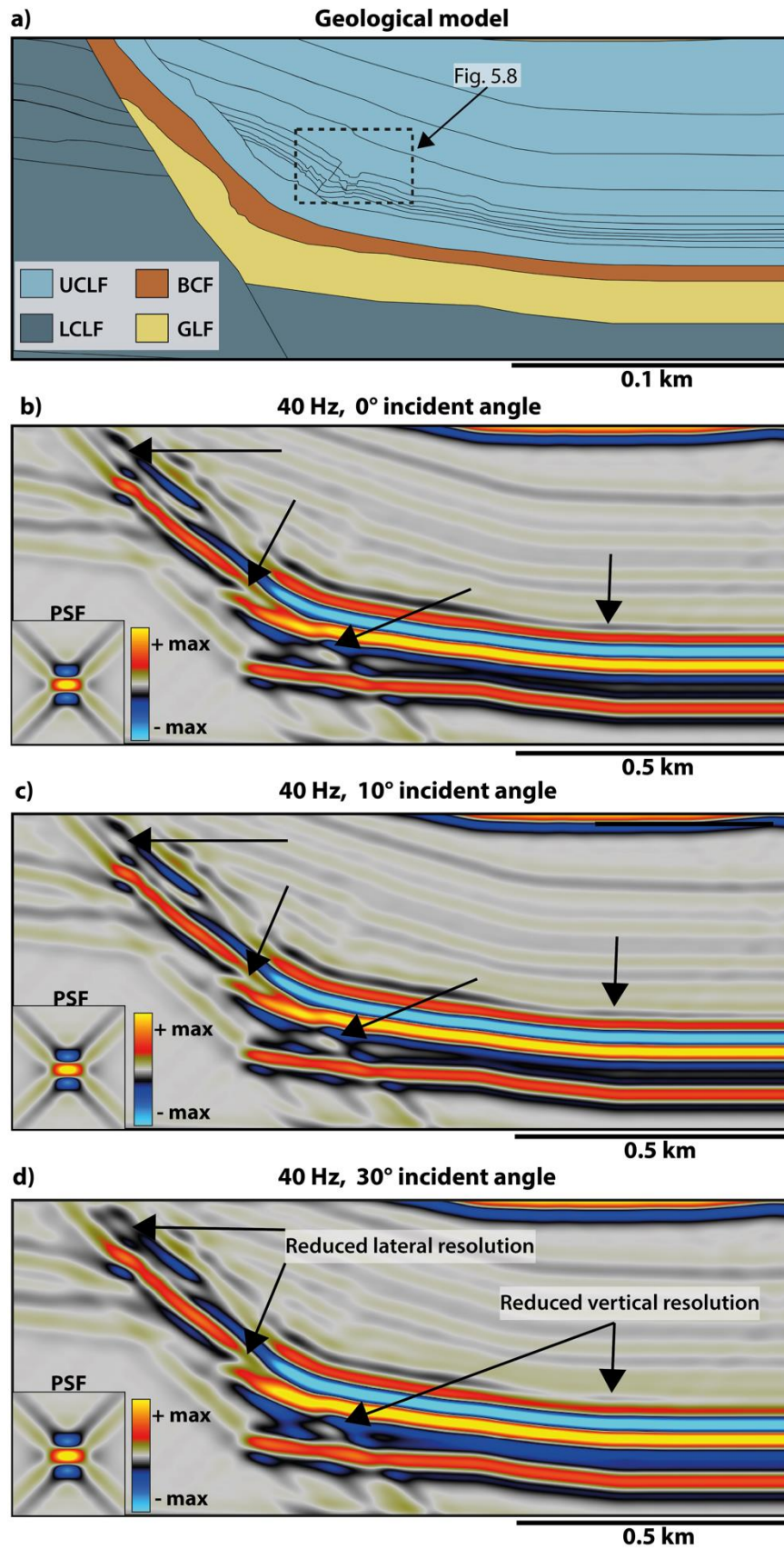


Figure 5.14: Effects of varying the angle of incidence on the synthetic seismic of Model 2. a) Represents the geological model, whereas the rest of the images represents the synthetic seismic with different incident angles: b) 0°, c) 10°, d) 30°. The PSF is representing the 2D seismic resolution. Changes in the seismic images are pointed out by black arrows.

5.2.5 Choice of wavelet

In this section, an alternative type of wavelet, the Ormsby wavelet, was used to generate synthetic seismic images of Model 4. Prior to modeling, the input wavelet has to be assigned specific parameters which define the shape and frequency spectrum of the wavelet (Ryan, 1994). Ormsby wavelets are zero-phase wavelets, which have numerous small side lobes and are often the type of wavelets directly extracted from actual seismic after processing at well ties. Four frequencies, a low-cut frequency, a low-pass frequency, a high-pass frequency and a high-cut frequency, have to be defined to specify an Ormsby wavelet (Ryan, 1994; Micenko, 2016). The Ricker wavelet, which has been applied in this study up till this point, is also a zero-phase wavelet, but an ideal one often used in seismic modeling, though not that representative of actual seismic. It differs from the Ormsby wavelet by only containing two small side lobes and being defined by a single parameter, which is the dominant frequency (Ryan, 1994). The differences in shape and frequency spectrum of the two wavelets are presented in Fig. 5.15: the Ormsby wavelet has a flat frequency band around 25 Hz, which is the dominant frequency of the Ricker wavelet. The extra side lobes come from the sharper frequency-band cuts around 10 Hz and 40 Hz and are similar truncation effects observed in the PSFs for limited illumination ranges: the sharper the transitions are, the stronger the side-lobe effect is.

Three different Ormsby wavelets, defined by the following low-cut, low-pass, high-pass and high-cut frequencies, were applied in this study:

- (i) 5-10-40-45 Hz
- (ii) 5-10-60-90 Hz
- (iii) 2-5-100-160 Hz

These frequencies of the Ormsby wavelet are reasonable correspondents to the following Ricker wavelet dominant frequencies:

- (i) 25 Hz
- (ii) 40 Hz
- (iii) 60 Hz

A comparison of the resulting synthetic seismic modeled with Ormsby wavelets and the corresponding Ricker wavelets is presented in Fig. 5.16. Similarly to the other sensitivity analyses, the maximum illumination angle is 45° and the angle of incidence is 0° for all cases. This was done with the aim to investigate the impacts of the wavelet type on the seismic.

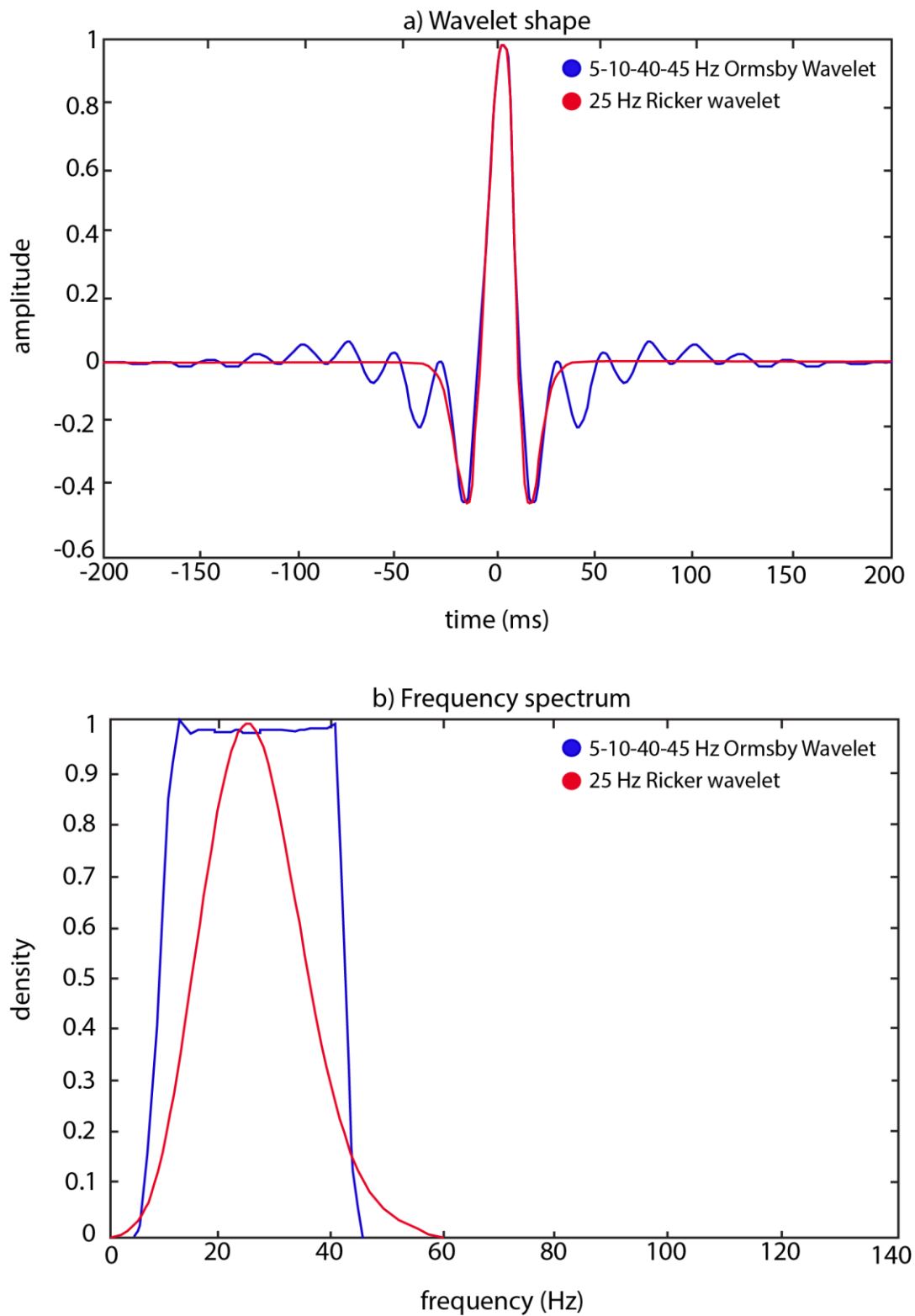


Figure 5.15: The (a) wavelet shape and (b) corresponding frequency spectrum of a 25 Hz Ricker wavelet and a 5-10-40-45 Hz Ormsby wavelet. Modified after Ryan (1994).

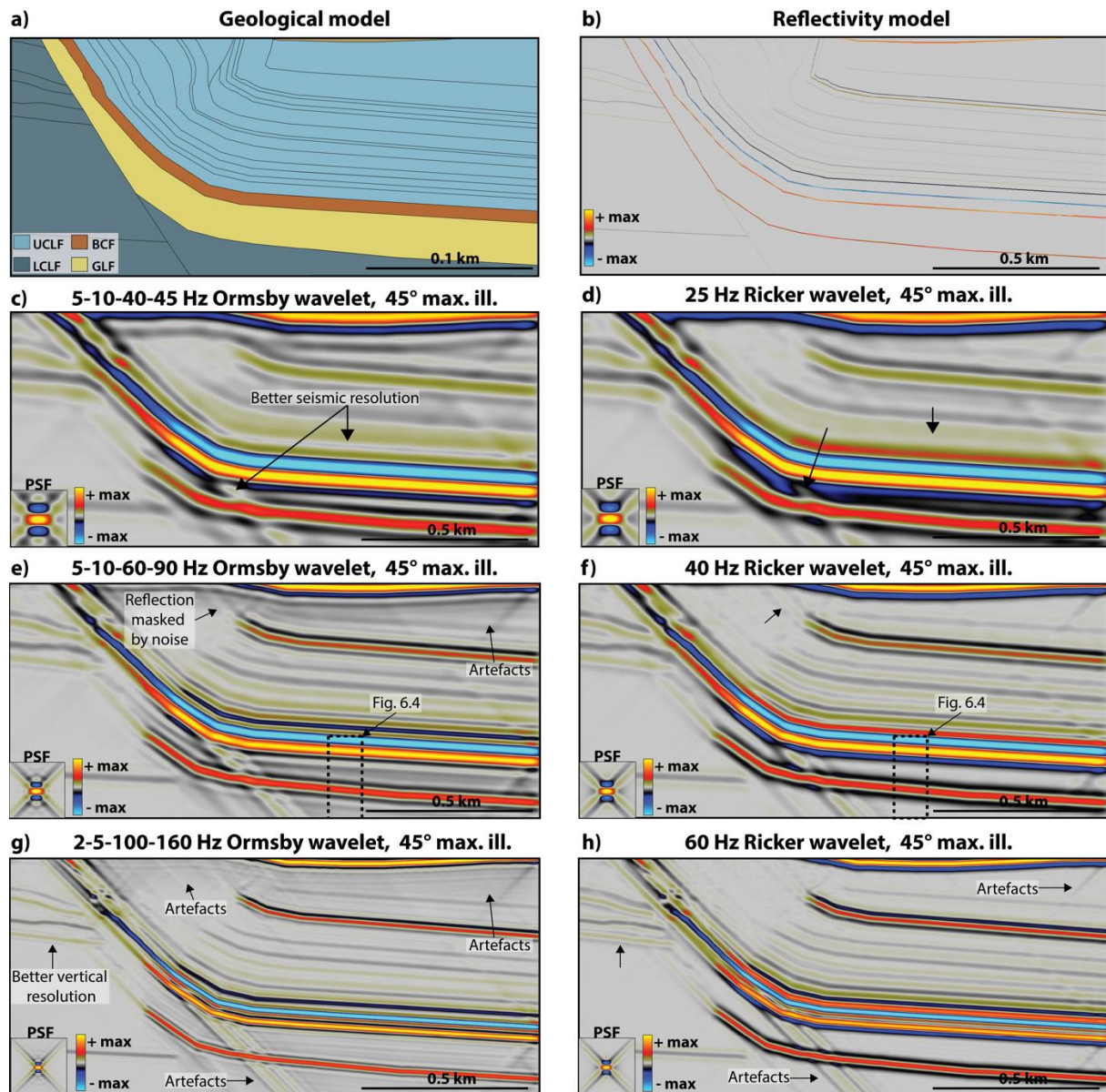


Figure 5.16: A comparison of the resulting synthetic seismic sections modeled with Ormsby wavelets of c) 5-10-40-45 Hz, e) 5-10-60-90 Hz and g) 2-5-100-160 Hz, and the corresponding dominant frequencies of the Ricker wavelet of d) 25 Hz, f) 40 Hz and h) 60 Hz. The black arrows point to features in the seismic that differs between the two wavelets.

The resulting seismic images of the two different types of wavelets show little variation in the seismic expression of the Maghlaq Fault at the different frequencies. Nonetheless, there are some differences worth noting (pointed out by black arrows in Fig. 5.16), which include changes in: (i) seismic resolution and (ii) level of imaging noise in the seismic. In general, the seismic resolution is slightly better for the Ormsby wavelet's synthetic seismic, although the differences are not very distinct. Small changes in vertical and lateral seismic resolution are noticeable in the middle of the seismic images, for the reflectors representing the very drag folded layers closest to the fault surface (Fig. 5.16 c versus d). The small variation in vertical

resolution is also noticeable from the reflections in the footwall (Fig. 5.16 g versus h). The other difference between the seismic images is the increase of noise from the Ricker wavelet to the Ormsby wavelet. This is controlled by the truncation effects from the simulated PSFs, which are different for the Ricker and Ormsby wavelets (Fig. 5.17). The PSF of the Ricker wavelet contains a cross-pattern, as seen in the previous modeling results, whereas the PSF of the Ormsby wavelet contains circular seismic artefacts in addition to the cross-pattern. The effect of these additional seismic artefacts for the Ormsby wavelet is particularly evident in the uppermost part in the synthetic seismic images of 5-10-60-90 Hz and 2-5-100-160 Hz (Figs. 5.16 e and g).

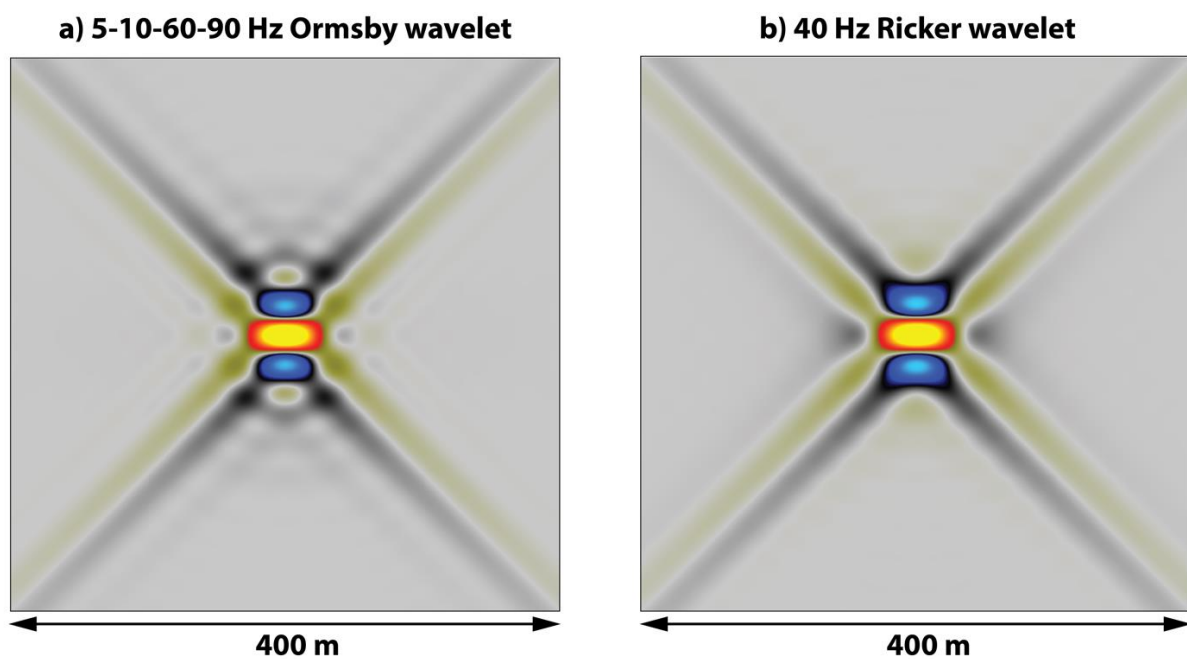


Figure 5.17: PSF of a) the 5-10-60-90 Hz Ormsby wavelet, and b) the corresponding Ricker wavelet of 40 Hz. Notice the difference in seismic artefacts between the two PSFs. The Ormsby wavelet generates a cross-pattern and circular artefacts, whereas the Ricker wavelet only generates a cross-pattern from the dip-limited illumination (here 45°).

6 Discussion

This thesis presents a synthetic workflow including 2D seismic modeling of outcrop-based geological models of the Maghlaq Fault zone. The resulting seismic images will be discussed in this chapter. Firstly, the importance of seismic modeling of outcrop analogues, and how this can aid seismic interpretation, will be addressed. Then, based on the aims of this study, two main questions will be discussed: (i) what is the seismic expression of the Maghlaq Fault zone? And (ii) what effect does each individual geophysical parameter have on the seismic images of the fault zone? Finally, the reliability of the geological models and the associated elastic properties are taken into consideration.

6.1 Outcrop-based seismic modeling and applications to seismic interpretation

Studying outcrop analogues is a key tool for improving the understanding of subsurface reservoirs, i.e. their geometries, structures, lithologies and associated potential for fluid flow (Pringle et al., 2006; Howell et al., 2014). Outcrop analogues provide valuable information on seismic and sub-seismic features in 3D, which can be compared to subsurface systems of similar geological settings studied in seismic (Pringle et al., 2006). Simulating synthetic seismic sections of outcrop-based geological models predicts the seismic response of stratigraphic and structural features from the outcrop. The synthetic seismic images reveal the level of details from the geological input model which can be identified in actual seismic data. Fig. 6.1 illustrates the details imaged in seismic of the damage zone of the Maghlaq Fault. The information from the outcrop and the synthetic seismic image combined can aid seismic interpretation of subsurface reservoirs by providing a link between onshore and offshore data (Anell et al., 2016). Not only can this potentially lead to more confident interpretations (Bond et al., 2007; Alcalde et al., 2017), but it can also improve the understanding of limitations in seismic datasets as well as the potential pitfalls when interpreting the data (Anell et al., 2016).

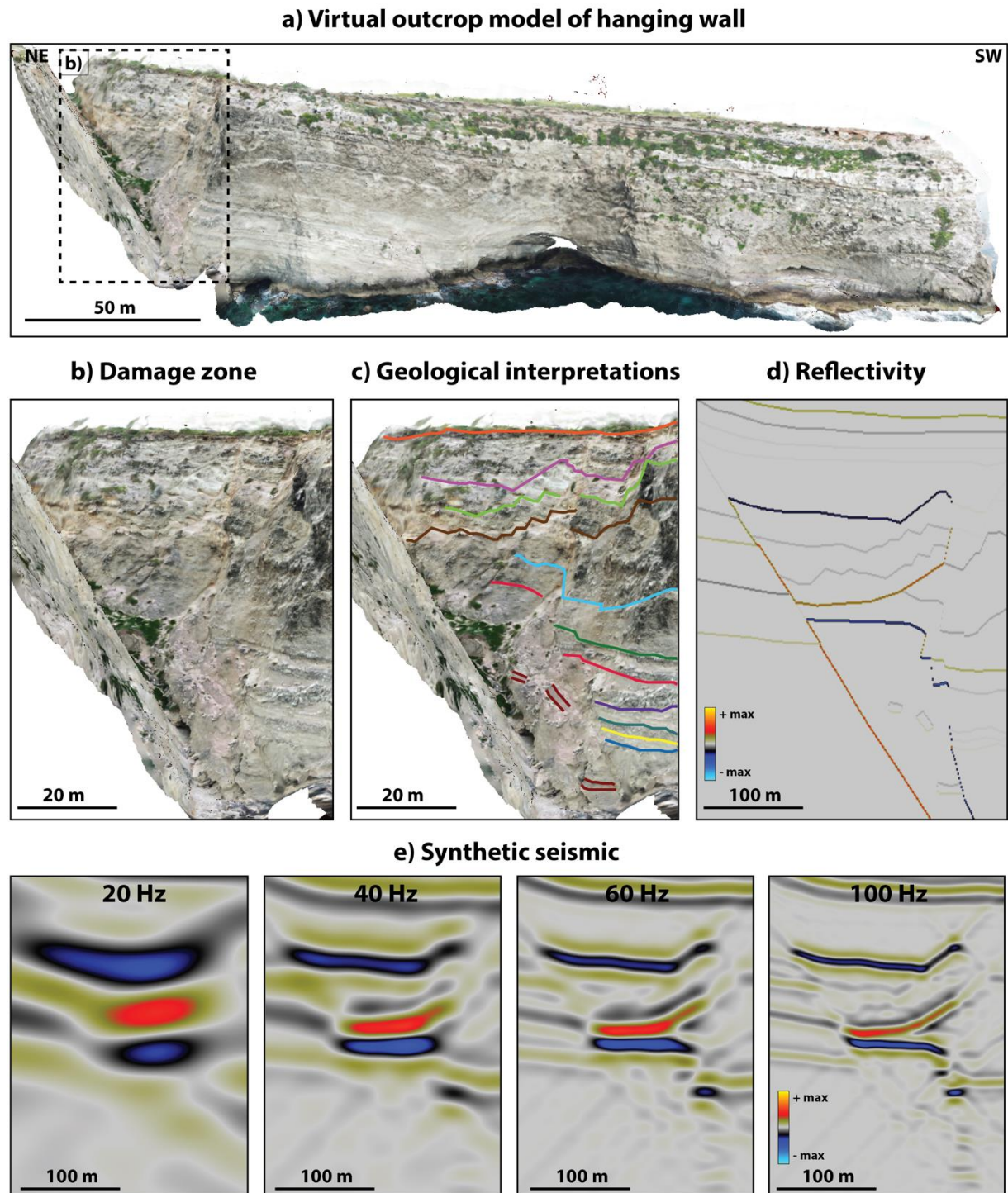


Figure 6.1: a) The virtual outcrop model of the hanging wall in Model 1. b) A close-up of the damage zone. c) Geological interpretations of structures and lithological layers within the zone. d) The corresponding reflectivity model, upscaled five times the original size of the geological model. e) Resulting synthetic seismic images at different dominant frequencies of the Ricker wavelet.

The Maghlaq Fault is indeed a good outcrop analogue to carbonate reservoirs hosting spatially heterogeneous normal fault zones. The fault zone comprises great internal variety both structurally and lithologically (Bonson et al., 2007). Additionally, it forms excellent 3D outcrop

exposures over a large area, making it a suitable analogue to subsurface reservoirs (Pringle et al., 2006). Seismic modeling of the Maghlaq Fault zone can help seismic interpretation of fault zones with similar rock properties and acoustic impedance contrasts (Table 1) (Falivene et al., 2010). Furthermore, the resulting synthetic seismic images reveal the detectability of the fault zone as function of various geophysical survey parameters. The effects of the varied parameters on the seismic signature of the fault zone also provide valuable information on survey parameters. This can be useful for designing seismic surveys for similar geological settings in the subsurface (Anell et al., 2016; Saffarzadeh et al., 2019).

Several other authors have previously presented synthetic workflows investigating the 2D seismic characterization of various geological features in outcrop analogues or conceptual geological models. Amongst others, these studies include seismic images of fault zones (Botter et al., 2014; Osagiede et al., 2014; Frery et al., 2016; Lubrano-Lavadera et al., 2018), folds (Lecomte et al., 2015), growth faults (Anell et al., 2016), igneous intrusions (Eide et al., 2018; Rabbel et al., 2018; Grippa et al., 2019) and shear zones (Wrona et al., 2019). The majority of these studies also perform sensitivity analyses, testing the impact of various geophysical parameters on the seismic expression and detectability of the geological features.

6.2 Seismic expression of the Maghlaq Fault

The resulting 2D seismic images of the Maghlaq Fault present the seismic signature of the fault zone. Due to the variation in hanging wall geometry in the four different geological models, the seismic expression slightly differs from model to model. However, some consistent seismic characteristics of the fault zone are recognizable in all synthetic seismic images, as pointed out by the numbers in Fig. 6.2:

- (1) Chaotic seismic reflection patterns close to the surface of the fault (representing the damage zone in Model 1 and vertical fault drag in Models 2, 3 and 4).
- (2) Multiple weak reflections in the hanging wall of the fault (representing the internal layering of the Upper Coralline Limestone Formation).
- (3) Discontinuous reflections in the footwall (indicating the location of the fault).
- (4) A coherent, strong reflection in the uppermost part of the models (representing the formation boundary between the overburden and the faulted limestones).

Other seismic characteristics of the Maghlaq Fault zone, which are varying for the different models, are:

(5) Numerous, sub-horizontal reflections in the hanging wall of Model 1 (Fig. 6.2a).

(6) Multiple inclined reflections (with dips ranging between 40 and 85°) in the hanging wall of Models 2, 3 and 4 (Figs. 6.2b-d).

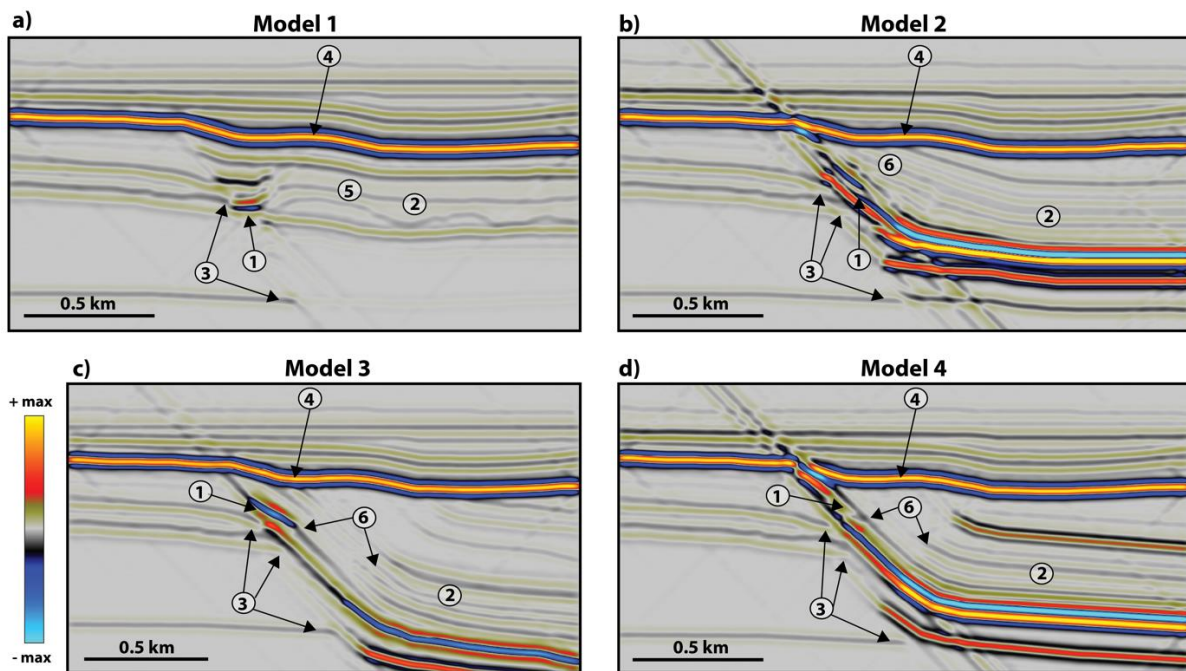


Figure 6.2: Seismic images created from the geological models of the Maghlaq Fault, representing the seismic expression of the normal fault zone. All four seismic images were generated with a 40 Hz Ricker wavelet, a maximum illumination angle of 45° and vertical incidence. The numbers point to seismic characteristics of the Maghlaq Fault zone, which are referred to in the text. a) Model 1 from Ix-Xaqqa, b) Model 2 from Ras Hanzir, c) Model 3 from Il-Miqtub and d) Model 4 from In-Neffiet.

The seismic expression of the carbonate fault zone is the result of a combination of the reflectivity of complex geological features and the impact of the geophysical parameters. Townsend et al. (1998) presents the seismic characterization of a fault as offset of reflection events in addition to a change in dip of the surrounding strata, as a result of fault-related deformation. These characteristics correspond well to the findings of the seismic signature of the Maghlaq Fault (numbers (3) and (6) in Fig. 6.2). The offset reflections allow for recognizing the continuity of the fault surface. Moreover, the chaotic reflection pattern surrounding the surface, including the folded strata, are supporting the interpretation of the fault's existence and its location. However, in real seismic data, deformation of surrounding strata might be masked due to noise (Botter et al., 2017).

6.3 Effects of changing the geophysical parameters

The results of the sensitivity analyses presented in this study provide information on the survey parameters and their individual effect on the seismic expression of the Maghlaq Fault. This information is especially important for investigating the seismic response of structural and stratigraphic details that are near the limit of seismic resolution. The effects on the seismic images of the fault zone from each parameter that has been tested in this study are discussed and compared to relevant studies in the following sections.

6.3.1 Effects of dominant frequency

The synthetic seismic images generated at different dominant frequencies of Ricker wavelets (10, 20, 30, 40, 60, 100, 150 and 200 Hz) demonstrate the effects of an improved seismic resolution on the seismic expression of the Maghlaq Fault (Figs. 5.7 and 5.8). This sensitivity testing reveals the most suitable dominant frequency of the Ricker wavelet for imaging the internal heterogeneities, i.e. structures and stratigraphy, of the fault zone. Firstly, the details of the hanging wall geometry are poorly imaged at the low dominant frequencies of 10 and 20 Hz (Figs. 5.7c and d). The reflections in these seismic images are continuous both vertically and laterally, making it difficult to identify the fault, its damage zone and to distinguish the lithological layers from each other.

The general trend for the seismic images is that the damage zone and hanging wall geometry are easily detectable at dominant frequencies of 30-40 Hz or more. These findings correspond well to the results obtained from the frequency impact analysis of Botter et al. (2014). In their study, the normal fault zone and the layers within the zone are also difficult to interpret at low frequencies (10-20 Hz Ricker wavelets), and easily identified at higher frequencies (30-40 Hz Ricker wavelets). Similar results are presented by Anell et al. (2016), where synthetic seismic images of growth faults, with offsets of around 50-100 m, have been generated. The change in dominant frequency illustrates limited changes in detectability of the faults from 10-20 Hz, but significant improvements at 30 Hz (Anell et al., 2016).

In addition to the frequency, the seismic resolution is also controlled by the seismic velocities of the rocks in the geological model (Rafaelsen, 2006; Herron, 2011). The synthetic data generated in this study include average P-wave velocities from 4.7-5.1 km/s. The very high-velocity limestones (Upper and Lower Coralline Limestone formations) in the foot and hanging

wall of the fault, when combined with a low dominant frequency of the input Ricker wavelet, result in poor imaging of the fault zone. For a dominant frequency of 30 Hz and a tuning thickness of a quarter of the wavelength, this suggests a theoretical vertical resolution of about 39 - 42.5 m (Eq. 3.1), meaning that features of thicknesses below this will not be imaged as separate reflections in the seismic.

Some of the thinnest layers in the hanging wall of the upscaled version of Model 1 are less than 15 m in thickness. To resolve the tightly spaced reflectors representing these layers, a dominant frequency of 80 Hz or more is required (Fig. 5.7h). These findings differ from the observations made in the study of seismic expressions of sill intrusions presented by Rabbel et al. (2018). In their study, a dominant frequency of 40 Hz Ricker wavelet is needed to resolve individual sills of thicknesses from 10-15 m as separate reflections (Rabbel et al., 2018). The large difference in required dominant frequency (80 Hz versus 40 Hz) for imaging approximately the same thicknesses can be explained by the difference in average velocity of the rocks included in the velocity models. A lower average seismic velocity of the geological input results in a shorter wavelength (Eq. 3.1), and thus an improved seismic resolution.

A frequency band centered at 80 Hz, as required for imaging the thinnest layers in Model 1, is however difficult to obtain in conventional-resolution seismic. Broadband seismic, such as TopSeis (Vinje et al., 2017) or P-cable seismic (Petersen et al., 2010), is therefore required in order to provide a wide enough frequency band to produce high-resolution images. However, in seismic acquisition, the effect of absorption in the earth is higher for high frequencies than low frequencies and hence the signal penetration is generally poorer for the high frequencies (ten Kroode et al., 2013).

Identifying small-scale internal heterogeneities in the seismic images of the Maghlaq Fault, i.e. fragmented fault rock (Fig. 5.7h) and small-scale faults (Fig. 5.8), requires a very high resolution as well. The synthetic seismic presented in this study demonstrate that a dominant frequency of at least 100 Hz is necessary to properly image these small-scale structures. Although a sufficiently high resolution is difficult to obtain in seismic data from high velocity lithologies, the small-scale structures that are visible at high dominant frequencies are of great importance to reservoir fluid flow. When considering the fluid flow properties of a fault zone, it can be crucial to include such structures because they can either form conduits or barriers for subsurface fluid flow (Rotevatn and Fossen, 2011).

6.3.2 Noise effects

The signal-to-noise ratio of the seismic is, amongst other parameters, determining the limit of detectability of structures in seismic (Zhang and Castagna, 2011; Simm and Bacon, 2014). The PSF-based convolution method (Lecomte et al., 2015, 2016) provides ideal seismic processing, generating synthetic seismic images with zero noise (Botter et al., 2017), except for imaging noise from the side lobes of the PSF. This simulates seismic responses of the fault zone where the main factors controlling the seismic expression are the reflectivity model and the geophysical survey parameters. To produce a more realistic seismic image, the level of colored random noise was systematically increased as part of the sensitivity testing (Fig. 5.10). The results showed that already at 25% noise, the Maghlaq Fault zone becomes difficult to detect in detail in the synthetic seismic. In the presence of 50% noise or more, the heterogeneities within the fault zone become almost non-detectable.

Wrona et al. (2019) present the synthetic seismic signature of shear zones and investigate how it varies with an increasing level of random noise. Similarly to the present study, the results of this testing show that steeply dipping features are non-detectable at high noise levels (50% or more). However, this is not only a result of the features being masked by the added noise, but also due to illumination limitations. Another study supporting the findings of the noise level testing is the seismic modeling study of Lubrano-Lavadera et al. (2018). In their study, random noise is added to seismic images of normal fault zones. The results demonstrate the interference between seismic signals and noise, and how this disturbs the seismic signature of the fault zone (Lubrano-Lavadera et al., 2018).

The imaging noise occurring in the synthetic seismic of the Maghlaq Fault includes cross-patterns. The cross-pattern effects are particularly evident in the seismic images of the Maghlaq Fault due to lack of noise, and lack of structural and stratigraphic details in some parts of the model, i.e. the footwall and underburden strata. It is important to mention that this is not an artefact of the PSF-based convolution method exclusively, but also an effect in real seismic data. However, because a simplified version of the seismic modeling method is applied in this thesis (analytical PSDM filter), the cross-pattern effect might be stronger than in reality (I Lecomte 2020, pers. comm., 12 May). Nevertheless, these imaging artefacts can potentially result in misinterpretations of the fault's presence, exact location and geometry, which can be crucial to the viability of an exploration prospect (Freeman et al., 1990).

6.3.3 Effects of dip-limited illumination

Seismic imaging of the steeply dipping features within the Maghlaq Fault zone is highly dependent on the angle of maximum illumination of the seismic survey. Although many of the steeply dipping features are represented by strong reflectors in all four reflectivity models presented in this study, they are not visible on all seismic images due to a dip-limited illumination. For instance, the reflectors representing the fault surface and fault-related folds in Model 3 (Fig. 5.11), as well as the overturned structures and recumbent folds in Model 4 (Fig. 5.12), are not imaged in the seismic generated with an angle of maximum illumination of 45° . This is because their geological dips (ranging from 60 to 85°) exceed the illumination vector span of maximum 45° in dip. Contrarily, when the angle of maximum illumination is 60° , the reflectors in Model 3 are very well imaged (Fig. 5.10e). The structures in Model 4, on the other hand, require an almost perfect illumination (90°) to be imaged with their true geological dips (Fig. 5.11d).

Although the steeply dipping features are easiest to detect when the illumination is perfect, it is still possible to identify similar geometries at lower maximum illumination angles. These observations correspond to what Anell et al. (2016) found for the synthetic seismic signature of growth faults. The synthetic seismic was modeled with maximum illumination angles from 20 - 90° and frequencies from 10 - 30 Hz. The results demonstrated that a higher angle of illumination and higher frequencies significantly improve the level of detail imaged in seismic. Nevertheless, the faults in their synthetic seismic still generated an appreciable expression which were somehow similar in all models, regardless of the illumination angle and frequency (Anell et al., 2016).

Fig. 6.3 illustrates the synthetic seismic images of Models 3 and 4, generated with an angle of maximum illumination of 45° , superimposed with the corresponding geological input models. The geological models are presented in gray scale to better visualize the structural input. The superposition highlights the absence of seismic responses of the steeply dipping reflectors, which is due to the dip-limited illumination. In Model 3 (Fig. 6.3a), neither the fault surface nor the fault-related folds are imaged, whereas the formation boundary between Upper Coralline Limestone Formation (UCLF) and Blue Clay/Greensand formations (BCF/GSF) is discontinuous and illuminated with an apparent dip. In Model 4 (Fig. 6.3b), neither the fault surface, the steeply dipping layers, the overturned structures nor the upper fold limb of the

recumbent fold are illuminated at a maximum illumination angle of 45° . A low angle of maximum illumination further leads to a low lateral resolution, which makes it impossible to perfectly image the steeply dipping features.

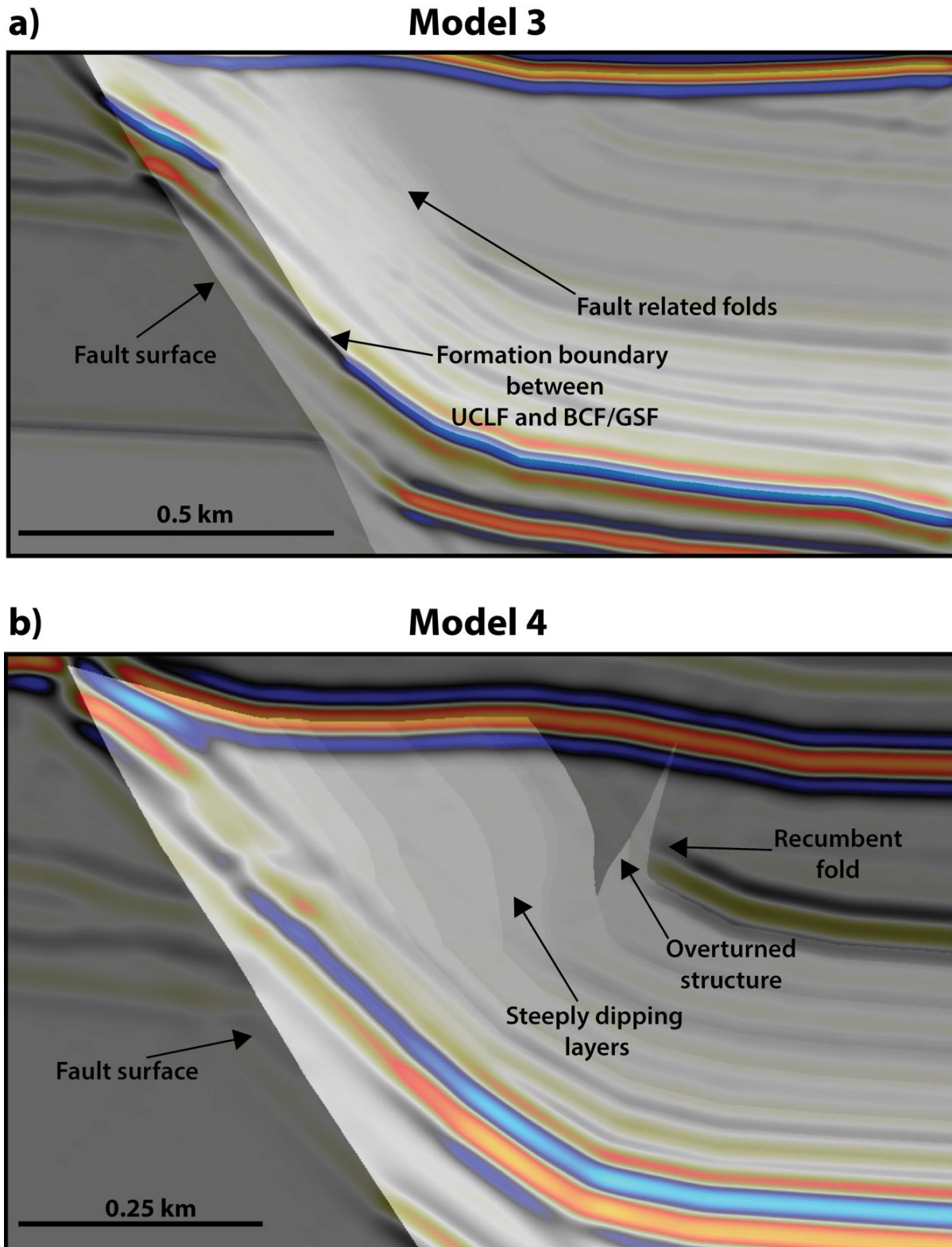


Figure 6.3: Seismic images generated with an angle of maximum illumination of 45° , superimposed with the corresponding geological input model of a) Model 3 and b) Model 4. The black arrows point to geological features in the geological models which are not illuminated in the synthetic seismic.

Other outcrop-based seismic modeling studies show similar results of seismic imaging with a dip-limited illumination. This includes limitations to illuminating near vertical or oblique dikes, presented by Eide et al. (2018), and limited illumination of shear zones with steep dips, presented by Wrona et al. (2019). These findings represent a potential pitfall in interpretation of seismic with a low angle of maximum illumination. The dip-limited illumination increases the likelihood of seismic misinterpretations of steeply dipping features, their existence, exact location, and orientation.

6.3.4 Effects of non-vertical incidence

Both the reflectivity model and the corresponding seismic are affected by the incident angle of the incoming seismic waves. The resolution of the seismic decreases with an increasing incident angle, as demonstrated by both the PSFs and the resulting seismic images (Fig. 5.13). The results of this sensitivity analysis show that the changes in resolution are limited when increasing the incident angle from 0 to 10° (Figs. 5.13b and c), whereas the resolution capacity decreases when further increasing the incident angle to 30° (Fig. 5.13d). However, the effect of the change in resolution in response to an increasing incident angle are in this case insignificant to the general seismic expression of the Maghlaq Fault.

The incident angles applied in this sensitivity analysis are not very wide, due to the high contrast in velocity between the marls and clays of the overburden and the limestones comprising the fault zone. The high velocity contrast limits the range of incident angles which can be applied in the sensitivity testing before the data becomes distorted in the seismic image (Jones, 2013). If the velocity contrast would have been smaller, seismic modeling could have been performed with significantly wider incident angles, which potentially could have a bigger impact on the seismic imaging of the fault. The effect of a large offset on the seismic image of folded structures is presented by Lecomte et al. (2015), which compares the effects of a zero-offset case with a large offset case. The seismic imaging of the folds in the large offset case is significantly poorer, with a decreased illumination and resolution (Lecomte et al., 2015). This result is similar to the result of the incident angle testing of the present study, even though the changes in resolution were not as distinctive.

6.3.5 Frequency-band effects

The last part of the sensitivity study in this thesis compares the impact of two different wavelets (Ricker and Ormsby) and their corresponding frequency bands on the synthetic seismic (Fig. 5.16). Prior to generating synthetic seismic images, a wavelet type and specific parameters to define the wavelet's shape and frequency spectrum have to be decided (Ryan, 1994). The comparison of the resulting seismic images illustrates advantages and disadvantages related to both wavelets. Firstly, the seismic resolution is slightly better in the synthetic seismic generated with an Ormsby wavelet, compared to the images generated with a Ricker wavelet. This can be observed from the small lateral and vertical changes between the synthetic seismic images, as well as from the comparison between the PSFs of the two wavelet types (Fig. 5.17). However, these differences are insignificant to the general seismic expression of the fault zone.

On the contrary, a change of great significance between the seismic images of the two wavelet types is the difference in generated noise. The synthetic seismic simulated with an Ormsby wavelet contains more seismic artefacts than the seismic simulated with a Ricker wavelet. The increased level of noise with the Ormsby wavelet results from truncation effects of the frequency spectrum yielding multiple side lobes around the main peak (Fig. 5.15a). The additional seismic artefacts produced from the multiple side lobes of the Ormsby wavelet lead to an increased number of reflections in the generated seismic. Fig. 6.4 compares the seismic wiggle traces of the 40 Hz Ricker wavelet and the 5-10-60-90 Hz Ormsby wavelet synthetic seismic. The synthetic seismic traces present a small part of the seismic section of Model 4, as pointed out in Figs. 5.16e and f. The wiggle trace of the Ormsby wavelet seismic includes two extra reflections which does not appear in the wiggle trace of the Ricker wavelet seismic (Figs. 6.4c and d). The extra seismic artefacts increase the likelihood of misinterpreting these reflections as corresponding to actual reflectors, instead of noise resulting from truncation effects. Consequently, the results of the frequency-band testing implicate that the Ricker wavelet might be more suitable for seismic modeling.

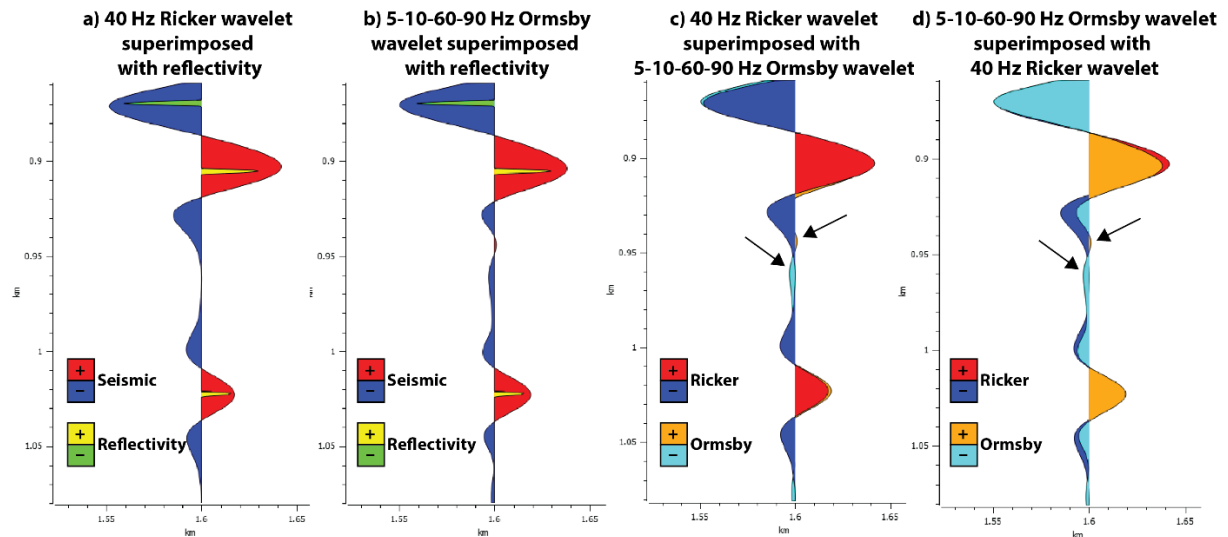


Figure 6.4: Superposition of wiggle traces from the seismic section of Model 4 (Figs. 5.16e and f). The first two plots show the reflectivity superimposed with the corresponding seismic wiggle trace generated with a) a 40 Hz Ricker wavelet and b) a 5-10-40-45 Hz Ormsby wavelet. The two last plots display the seismic wiggle traces in a) and b) superimposed. In c) the Ricker wavelet seismic is the overlying wiggle trace, whereas in d) the Ormsby wavelet seismic is the overlying wiggle trace.

6.3.6 Summary of geophysical parameter effects

The results of the sensitivity study reveal which geophysical parameters that have the largest impact on the seismic signature of the Maghlaq Fault zone. These include the dominant frequency, angle of maximum illumination and level of noise. The sensitivity testing further gives an idea of which geophysical parameters that are most appropriate for better visualizing the fault zone and its internal heterogeneities in seismic. To ideally image the fault's surface, damage zone and steeply dipping hanging wall geometry, the analytical PSDM filter of the convolution method has to include: (i) a Ricker wavelet with a dominant frequency of at least 30 Hz, (ii) a maximum illumination angle of 60° , although geometries in the hanging wall are still recognizable at a maximum illumination angle of 45° , and (iii) an incident angle between 0° and 30° . Lastly, (iv) the level of noise must be no more than 25%. However, these values might not be attainable in actual cases, with an overburden geology and a realistic seismic survey.

6.4 Uncertainties related to the geological modeling

6.4.1 Limitations to geological interpretations

The quality and reliability of the synthetic seismic images are a combination of geological model building and seismic modeling (Alaei, 2012). In other words, the creation of the

geological model is equally important as the generation of synthetic seismic. Creating virtual outcrop models from photogrammetry is a time- and cost-efficient method which can acquire digital models of highly detailed geological input. Even though it is an excellent tool that can expand the field season and possibly improve the geological interpretations, there are some challenges associated with interpreting virtual outcrop models. This includes bad and shifting light and weather conditions (e.g. Fig. 5.4c), as well as the challenge of interpreting 3D structures as 2D cross sections. Faults and the surrounding damage zones are complex 3D volumes that should ideally not be interpreted as 2D structures, because their geometries, distribution of rocks and petrophysical properties affect the connectivity within a reservoir in 3D (Botter et al., 2014). Creating 2D geological models further limits the seismic modeling to only simulate 2D seismic sections, although the modeling method itself is not limited to 2D. However, this study opens the door for creating 3D geological models based on the same virtual outcrop models, and therefore also generation of 3D synthetic seismic of the Maghlaq Fault.

The Maghlaq Fault is indeed a spatially heterogenous zone of complex architecture in terms of structures and rock content. When generating models of such a large-scale fault, it is challenging to extract and include all levels of detail which are present in the complexity of the core and damage zone. Adding microscale structures such as foliation, fractures, cataclasite and breccia in the large-scale model would create a more realistic representation of the Maghlaq Fault. However, it was not possible to identify these small-scale features from the VOMs, which the geological models were built upon. Moreover, microscale structures are well below the limit of seismic resolution, and the absence of these features in the structural input is therefore considered negligible in this case.

The geological models are a combination of interpretations of the VOMs and conceptual extrapolations and interpretations. Using real geology from VOMs as the base for the structural and lithological input reduces simplifications in the models. In addition, the structural features and the lithostratigraphy in the models are supported by field studies conducted by several other authors (Pedley et al., 1976; Dart et al., 1993; Bonson et al., 2007), which further reduces the uncertainties in the models. That being said, the models are still subject to uncertainty, as there are limitations to all geological interpretations and extrapolations. This includes uncertainties regarding the thicknesses of stratigraphic layers, extrapolation of the folding, unconformities, and the choice of overburden lithology. Nonetheless, if the geological models of the Maghlaq Fault are not exact representations of the fault zone, at least they are realistic approximations.

6.4.2 Limitations to elastic properties

The geological models must be assigned elastic properties (V_p , V_s and density) in order to perform seismic modeling. Retrieving realistic values for faulted, deformed and brecciated carbonates are difficult without physical rock property measurements of each of the geological units. The units that were included in the geological models were treated as homogenous and continuous components for the sake of simplification. However, in nature these rock units are highly variable and internally varying both laterally and vertically in terms of elastic properties. Including all different types of structures and fault rock mentioned above (foliation, fractures, cataclasite and breccia) would require numerous realistic values of elastic properties, which ideally should be extracted from physical measurements of the rocks. In the absence of physical measurements of the geological units in the fault zone, the four geological models were assigned purely conceptual elastic properties of values derived from literature studies (Pickett, 1963; Tosaya and Nur, 1982; Bourbie et al., 1987; Miller and Stewart, 1990; Miller, 1992; Castagna et al., 1993; Dvorkin et al., 2001; Agosta et al., 2007; Mavko, 2017).

The elastic properties play a significant role in seismic modeling as they define the reflectivity model. The hard and massive limestones (Upper and Lower Coralline Limestone) were assigned very high seismic velocities (V_p of 4.7-6.0 km/s). The marly biomicrite and coccolithic limestone (Globigerina Limestone) were given intermediate seismic velocities (V_p of 3.7-4.0 km/s), and the soft clay (Blue Clay), calcareous sand (Greensand), and marls (post-rift marls and clays) were assigned low seismic velocities (V_p of 1.9-3.0 km/s). As expected, this resulted in high contrasts in acoustic impedance between:

- (i) The intermediate-velocity layer of Globigerina Limestone and the low-velocity layer of Blue Clay, in Models 2, 3 and 4.
- (ii) The low-velocity layer of Blue Clay/Greensand and the high-velocity layer of Upper Coralline Limestone, in Models 2, 3, and 4.
- (iii) The smeared layers of Globigerina Limestone and Blue Clay and the fault surface of Lower Coralline Limestone, in Models 2, 3 and 4.
- (iv) The high-velocity layers of Upper and Lower Coralline Limestone and the low-velocity layer of post-rift marls and clays in the overburden, in all four models.

The latter constitutes the highest contrast in acoustic impedance, which thereupon corresponds to the highest amplitude of the reflections in the seismic images. Contrarily, the layers of Upper Coralline Limestone, which comprise the hanging wall geometry of the Maghlaq Fault, do not have a high contrast in acoustic impedance. This is due to the very similar values of elastic properties of the layers within the formation. Consequently, this results in weaker amplitudes of the reflections representing the hanging wall, which again leads to the interesting structural features, i.e. steeply dipping layers and small-scale faults, being poorly imaged in the seismic.

Despite the limitations to the geological models and associated elastic properties, the seismic images generated in this thesis give an idea of how geologically complex hanging wall structures in carbonates are imaged in 2D seismic data. The seismic reflection geometry of the fault zone architecture in a specific geological setting, like the carbonate-dominated Maghlaq Fault, can give implications on how similar geometries would be imaged in real seismic data. This is a benefit of using real geology from VOMs as an input for seismic modeling. It also allows for an analysis on both the resolvability of small-scale structures and the illumination of steeply dipping features in fault zones, related to the different geophysical parameters applied. Insights from this study can help bridge the gap between field observations and seismic interpretation.

7 Conclusion and further work

7.1 Concluding remarks

This thesis presents synthetic 2D seismic images generated from geological models of a carbonate-hosted normal fault zone, which are based on virtual outcrop models of the hanging wall of the Maghlaq Fault, Malta. Sensitivity testing of various geophysical parameters were performed on the resulting synthetic seismic to investigate their impact on the seismic expression of the fault zone. The presented results and discussion have led to the following conclusions of this thesis:

1. Outcrop analogues such as the Maghlaq Fault provide important information on both seismic and sub-seismic structural and stratigraphic features, which is comparable to subsurface systems of similar geological settings.
2. Realistic seismic modeling of detailed geological models, based on high-resolution virtual outcrop models, is a key tool for bridging the gap between geological field observations and interpretation of subsurface structures in seismic.
3. The seismic expression of the Maghlaq Fault is differing to some degree for the four different geological models, due to the significant variation in hanging wall geometry from east to west along the fault. Nevertheless, some seismic characteristics are consistent for all seismic images, regardless of the geological input model. The fault zone can generally be identified in seismic from: (1) chaotic seismic reflections close to the fault plane, (2) multiple, weak reflections in the hanging wall, (3) discontinuous reflections in the footwall, and (4) a strong, highly continuous reflection in the upper part of the model.
4. The results of the geophysical parameter sensitivity study revealed that the dominant frequency, the level of noise and the illumination angle are the parameters that have the greatest impact on the seismic images.
5. A fault zone within carbonates, like the Maghlaq Fault, is easily detectable in seismic at a dominant frequency of 30 Hz or more (Ricker wavelet), a noise level of less than 25%, a maximum illumination angle of 60° and an incident angle between 0 and 30°. However, the general seismic characteristics of the fault are still recognizable at less ideal parameter values.

6. Internal heterogeneities and fault-related structures, such as steeply dipping features, small-scale faults (5-20 m displacement) and geological layers of thicknesses of less than 15 m, require ideal values of the geophysical parameters, i.e. a dominant frequency of 80 Hz and an angle of maximum illumination between 60 and 90°, to be perfectly imaged. Such structures are thus unlikely to be imaged in actual seismic data using standard acquisition parameters. This illustrates the difficulties related to both seismic imaging and interpretation of details in fault zones.
7. The findings of this study may however help to improve the seismic interpretation of carbonate-hosted fault zones, as well as to increase the understanding of geophysical parameter dependency of seismic images.

7.2 Suggestions for further work

This thesis is a contribution to improve the understanding of seismic imaging of normal fault zones within carbonates. To reduce the uncertainties related to the input geological models and possibly improve and extend this study, the following ideas are suggested for future work:

- Perform seismic modeling with elastic properties (V_p , V_s and density) derived from physical rock property measurements of the geological formations comprising the Maghlaq Fault zone.
- Alternatively, compare the synthetic seismic images of the high velocity case of the present thesis to synthetic seismic generated from intermediate or low velocity cases.
- Include a higher degree of heterogeneity of rock properties within the individual units of the fault zone.
- Compare the generated synthetic seismic to real seismic data of subsurface carbonate fault zones.
- Create 3D geological models from the virtual outcrop models to generate 3D synthetic seismic of the Maghlaq Fault

References

- Agosta, F., Prasad, M., and Aydin, A., 2007, Physical properties of carbonate fault rocks, fucino basin (Central Italy): Implications for fault seal in platform carbonates: *Geofluids*, 7, 19–32.
- Alaei, B., 2012, Seismic modeling of complex geological structures: *Seismic waves - Research and Analysis*, 11, 213–236.
- Alcalde, J., Bond, C.E., Johnson, G., Butler, R.W.H., Cooper, M.A., and Ellis, J.F., 2017, The importance of structural model availability on seismic interpretation: *Journal of Structural Geology*, 97, 161–171.
- Anell, I., Lecomte, I., Braathen, A., and Buckley, S.J., 2016, Synthetic seismic illumination of small-scale growth faults, paralic deposits and low-angle clinoforms: A case study of the Triassic successions on Edgeøya, NW Barents Shelf: *Marine and Petroleum Geology*, 77, 625–639.
- Argnani, A., 1990, The strait of sicily rift zone: Foreland deformation related to the evolution of a back-arc basin: *Journal of Geodynamics*, 12, 311–331.
- Bastesen, E., and Braathen, A., 2010, Extensional faults in fine grained carbonates - analysis of fault core lithology and thickness-displacement relationships: *Journal of Structural Geology*, 32, 1609–1628.
- Bastesen, E., Braathen, A., Nøttveit, H., Gabrielsen, R.H., and Skar, T., 2009, Extensional fault cores in micritic carbonate - Case studies from the Gulf of Corinth, Greece: *Journal of Structural Geology*, 31, 403–420.
- Bemis, S.P., Micklethwaite, S., Turner, D., James, M.R., Akciz, S., Thiele, S., and Bangash, H.A., 2014, Ground-based and UAV-Based photogrammetry: A multi-scale, high-resolution mapping tool for structural geology and paleoseismology: *Journal of Structural Geology*, 69, 163–178.
- Ben-Avraham, Z., Ginzburg, A., Makris, J., and Eppelbaum, L., 2002, Crustal structure of the Levant Basin, eastern Mediterranean: *Tectonophysics*, 361, 23–43.
- Billi, A., Salvini, F., and Storti, F., 2003, The damage zone-fault core transition in carbonate rocks: Implications for fault growth, structure and permeability: *Journal of Structural Geology*, 25, 1779–1794.
- Bond, C.E., Gibbs, A.D., Shipton, Z.K., and Jones, S., 2007, What do you think this is? “Conceptual uncertainty” In geoscience interpretation: *GSA Today*, 17, 4–10.
- Bonson, C.G., Childs, C., Walsh, J.J., Schöpfer, M.P.J., and Carboni, V., 2007, Geometric and kinematic controls on the internal structure of a large normal fault in massive limestones: The Maghlaq Fault, Malta: *Journal of Structural Geology*, 29, 336–354.
- Bosence, D.W.J., and Pedley, H.M., 1982, Sedimentology and palaeoecology of a Miocene coralline algal biostrome from the Maltese Islands: *Palaeogeography, Palaeoclimatology, Palaeoecology*, 38, 9–43.
- Botter, C., Cardozo, N., Hardy, S., Lecomte, I., and Escalona, A., 2014, From mechanical modeling to seismic imaging of faults: A synthetic workflow to study the impact of faults on seismic: *Marine and Petroleum Geology*, 57, 187–207.
- Botter, C.D., Cardozo, N., Qu, D., Kholuykin, D., and Tveranger, J., 2017, Seismic characterization of fault facies models: *Interpretation*, 5, 9–26.
- Bourbie, T., Coussy, O., and Zinszner, B., 1987, Acoustics of Porous Media: Gulf Publ. Co.
- Braathen, A., Tveranger, J., Fossen, H., Skar, T., Cardozo, N., Semshaug, S.E., Bastesen, E., and Sverdrup, E., 2009, Fault facies and its application to sandstone reservoirs: *AAPG Bulletin*, 93, 891–917.

- Brigaud, B., Vincent, B., Durllet, C., Deconinck, J.-F., Blanc, P., and Trouiller, A., 2010, Acoustic Properties of Ancient Shallow-Marine Carbonates: Effects of Depositional Environments and Diagenetic Processes (Middle Jurassic, Paris Basin, France): *Journal of Sedimentary Research*, 80, 791–807.
- Di Bucci, D., Burrato, P., Vannoli, P., and Valensise, G., 2010, Tectonic evidence for the ongoing Africa-Eurasia convergence in central Mediterranean foreland areas: A journey among long-lived shear zones, large earthquakes, and elusive fault motions: *Journal of Geophysical Research: Solid Earth*, 115.
- Buckley, S.J., Ringdal, K., Naumann, N., Dolva, B., Kurz, T.H., Howell, J.A., and Dewez, T.J.B., 2019, LIME: Software for 3-D visualization, interpretation, and communication of virtual geoscience models: *Geosphere*, 15, 222–235.
- Caine, J.S., Evans, J.P., and Forster, C.B., 1996, Fault zone architecture and permeability structure: *Geology*, 24, 1025–1028.
- Carcione, J.M., Herman, G.C., and ten Kroode, A.P.E., 2002, Seismic modeling: *Geophysics*, 67, 1304–1325.
- Carminati, E., Lustrino, M., and Doglioni, C., 2012, Geodynamic evolution of the central and western Mediterranean: Tectonics vs. igneous petrology constraints: *Tectonophysics*, 579, 173–192.
- Castagna, J.P., Batzle, M.L., Kan, T.K., and Backus, M.M., 1993, Rock Physics - The Link Between Rock Properties and AVO Response: *Offset-Dependent Reflectivity—Theory and Practice of AVO Analysis. SEG*, 8, 135–171.
- Cavazza, W., and Wezel, F.C., 2003, The Mediterranean region- A geological primer: *Episodes*, 26, 160–168.
- Childs, C., Manocchi, T., Walsh, J.J., Bonson, C.G., Nicol, A., and Schöpfer, M.P.J., 2009, A geometric model of fault zone and fault rock thickness variations: *Journal of Structural Geology*, 31, 117–127.
- Childs, C., Walsh, J.J., and Watterson, J., 1997, Complexity in fault zone structure and implications for fault seal prediction: *Norwegian Petroleum Society Special Publications*, 7, 61–72.
- Dart, C.J., Bosence, D.W.J., and McClay, K.R., 1993, Stratigraphy and structure of the Maltese Graben system: *Journal of the Geological Society, London*, 150, 1153–1166.
- Dey, A.K., and Stewart, R.R., 1997, Predicting density using Vs and Gardner's relationship: *CREWES Research Report*, 9, 1–9.
- Dunham, R.J., 1962, Classification of Carbonate Rocks According to Depositional Textures.
- Dvorkin, J., Walls, J.D., and Mavko, G., 2001, Rock physics of marls: In 2001 SEG Annual Meeting, *Society of Exploration Geophysicists*.
- Eide, C.H., Schofield, N., Lecomte, I., Buckley, S.J., and Howell, J.A., 2018, Seismic interpretation of sill complexes in sedimentary basins: Implications for the sub-sill imaging problem: *Journal of the Geological Society*, 175, 193–209.
- Evans, J.P., Forster, C.B., and Goddard, J. V., 1997, Permeability of fault-related rocks, and implications for hydraulic structure of fault zones: *Journal of Structural Geology*, 19, 1393–1404.
- Falivene, O., Arbués, P., Ledo, J., Benjumea, B., Muñoz, J.A., Fernández, O., and Martínez, S., 2010, Synthetic seismic models from outcrop-derived reservoir-scale three-dimensional fades models: The Eocene Ainsa turbidite system (Southern Pyrenees): *AAPG Bulletin*, 94, 317–343.
- Felix, R., 1973, *Oligo-Miocene stratigraphy of Malta and Gozo*: PhD thesis, University of Utrecht.
- Finetti, I., 1982, Structure, stratigraphy and evolution of the central Mediterranean: *Bollettino di Geofisica Teorica ed Applicata*, 24, 247-312.

- Finetti, I., 1984, Geophysical study of the Sicily Channel rift zone: *Bollettino di Geofisica Teorica ed Applicata*, 26, 3-28
- Fonseca, J.S., Teixeira, L., Maul, A., Barros, P., Borges, F., Boechat, J., and González, M., 2018, Modelling geological layers into new velocity models for seismic migration process - a Brazilian pre-salt case, in 1st EAGE/PESGB Workshop on Velocities, *European Association of Geoscientists & Engineers*, 541.
- Freeman, B., Yielding, G., and Badley, M., 1990, Fault correlation during seismic interpretation: *First Break*, 8, 87–95.
- Frery, E., Langhi, L., Strand, J., and Shragge, J., 2016, Seismic modelling of fault zones: *The APPEA Journal*, 56, 599.
- Gardner, G.H.F., Gardner, L.W., and Gregory, A.R., 1974, Formation velocity and density; the diagnostic basics for stratigraphic traps: *Geophysics*, 39, 770–780.
- Gauthier, B.D.M., and Lake, S.D., 1993, Probabilistic modeling of faults below the limit of seismic resolution in Pelican Field, North Sea, offshore United Kingdom: *American Association of Petroleum Geologists Bulletin*, 77, 761–777.
- Graham, B., Antonellini, M., and Aydin, A., 2003, Formation and growth of normal faults in carbonates within a compressive environment: *Geology*, 31, 11–14.
- Grippa, A., Hurst, A., Palladino, G., Iacopini, D., Lecomte, I., and Huuse, M., 2019, Seismic imaging of complex geometry: Forward modeling of sandstone intrusions: *Earth and Planetary Science Letters*, 513, 51–63.
- Gueguen, E., Doglioni, C., and Fernandez, M., 1998, On the post-25 Ma geodynamic evolution of the western Mediterranean: *Tectonophysics*, 298, 259–269.
- Herron, D.A., 2011, *First Steps in Seismic Interpretation* (R. B. Latimer, Ed.): Tulsa, Oklahoma, Society of Exploration Geophysicists.
- Hesthammer, J., Landrø, M., and Fossen, H., 2001, Use and abuse of seismic data in reservoir characterisation: *Marine and Petroleum Geology*, 18, 635–655.
- Hilterman, F.J., 1970, Three-dimensional seismic modeling: *Geophysics*, 35, 1020–1037.
- Howell, J.A., Martinius, A.W., and Good, T.R., 2014, The application of outcrop analogues in geological modelling: a review, present status and future outlook: *Geological Society, London, Special Publications*, 387, 1–25.
- Illies, J.H., 1981, Graben formation: The Maltese Islands – A case history: *Tectonophysics*, 73, 151–168.
- Jones, I.F., 2013, Tutorial: The seismic response to strong vertical velocity change: *First Break*, 31, 79–90.
- Jongsma, D., van Hinte, J., E. and Woodside J., M., 1984, Geologic structure and neotectonics of the North African Continental Margin south of Sicily: *Marine and Petroleum Geology*, 2, 156-179.
- Kastens, K. et al., 1988, ODP Leg 107 in the Tyrrhenian Sea: Insights into passive margin and back-arc basin evolution: *Bulletin of the Geological Society of America*, 100, 1140–1156.
- Kearey, P., and Brooks, M., 1991, *An introduction to geophysical exploration*. 2nd edition: Malden, Massachusetts, Blackwell Science.
- Khaidukov, V., Landa, E., and Moser, T.J., 2004, Diffraction imaging by focusing-defocusing: An outlook on seismic superresolution: *Geophysics*, 69, 1478–1490.
- Kim, Y.S., Peacock, D.C.P., and Sanderson, D.J., 2004, Fault damage zones: *Journal of Structural Geology*, 26, 503–517.
- ten Kroode, F., Bergler, S., Corsten, C., de Maag, J.W., Strijbos, F., and Tjihof, H., 2013, Broadband seismic data-The importance of low frequencies: *Geophysics*,.
- Landa, E., 2012, Seismic diffraction: Where's the value?: In 2012 SEG Annual Meeting, *Society of Exploration Geophysicists*.
- Lecomte, I., 2008, Resolution and illumination analyses in PSDM: A ray-based approach: *The*

- Leading Edge*, 27, 650–663.
- Lecomte, I., Lavadera, P.L., Anell, I., Buckley, S.J., Schmid, D.W., and Heeremans, M., 2015, Ray-based seismic modeling of geologic models: Understanding and analyzing seismic images efficiently: *Interpretation*, 3, 71–89.
- Lecomte, I., Lavadera, P.L., Botter, C., Anell, I., Buckley, S.J., Eide, C.H., Grippa, A., Mascolo, V., and Kjoberg, S., 2016, 2(3)D convolution modelling of complex geological targets beyond – 1D convolution: *First Break*, 34, 99–107.
- Lindsey, J.P., 1989, The Fresnel zone and its interpretive significance: *The Leading Edge*, 8, 33–39.
- Lubrano-Lavadera, P., Senger, K., Lecomte, I., Mulrooney, M.J., and Kühn, D., 2018, Seismic modelling of metre-scale normal faults at a reservoir-cap rock interface in Central Spitsbergen, Svalbard: implications for CO₂ storage: *Norwegian Journal of Geology*, 66, 1180–1200.
- Mavko, G., 2017, Parameters That Influence Seismic Velocity: *Stanford University*.
- McGrath, A.G., and Davison, I., 1995, Damage zone geometry around fault tips: *Journal of Structural Geology*, 17, 1011–1024.
- Micallef, A., Foglini, F., Le Bas, T., Angeletti, L., Maselli, V., Pasuto, A., and Taviani, M., 2013, The submerged paleolandscape of the Maltese Islands: Morphology, evolution and relation to quaternary environmental change: *Marine Geology*, 335, 129–147.
- Micenko, M., 2016, Seismic Window: *Preview*, 184, 32–33.
- Michie, E.A.H., 2015, Influence of host lithofacies on fault rock variation in carbonate fault zones: A case study from the Island of Malta: *Journal of Structural Geology*, 76, 61–79.
- Michie, E.A.H., Haines, T.J., Healy, D., Neilson, J.E., Timms, N.E., and Wibberley, C.A.J., 2014, Influence of carbonate facies on fault zone architecture: *Journal of Structural Geology*, 65, 82–99.
- Miller, S.L.M.M., 1992, Well log analysis of V_p and V_s in carbonates: *CREWES Research Reportvol*, 4, 1–11.
- Miller, S., and Stewart, R., 1990, Effects of lithology, porosity and shaliness on P- and S-wave velocities from sonic logs: *Canadian journal of Exploration Geophysicsjournal of Exploration Geophysics*, 26, 94–103.
- Osagiede, E.E., Duffy, O.B., Jackson, C.A.L., and Wrona, T., 2014, Quantifying the growth history of seismically imaged normal faults: *Journal of Structural Geology*, 66, 382–399.
- Peacock, D.C.P., Fisher, Q.J., Willemse, E.J.M., and Aydin, A., 1998, The relationship between faults and pressure solution seams in carbonate rocks and the implications for fluid flow: *Geological Society Special Publication*, 147, 105–115.
- Pedley, H.M., 1975, Miocene Sea-floor Subsidence and Later Subaerial Solution Subsidence Structures in the Maltese Islands: *Proceedings of the Geologist's Association*, 85, 533–547.
- Pedley, H.M., 1987, Controls on Cenozoic carbonate deposition in the Maltese Islands: review and interpretation: *Memorie della Societa'Geologica Italiana*, 38, 81–94.
- Pedley, H.M., and Bennett, S.M., 1985, Phosphorites, hardgrounds and syndepositional solution subsidence: A palaeoenvironmental model from the miocene of the Maltese Islands: *Sedimentary Geology*, 45, 1–34.
- Pedley, H.M., House, M.R., and Waugh, B., 1976, The geology of Malta and Gozo: *Proceedings of the Geologists' Association*, 87, 325–341.
- Petersen, C.J., Bünz, S., Hustoft, S., Mienert, J., and Klaeschen, D., 2010, High-resolution P-Cable 3D seismic imaging of gas chimney structures in gas hydrated sediments of an Arctic sediment drift: *Marine and Petroleum Geology*, 27, 1981–1994.
- Pickett, G.R., 1963, Acoustic Character Logs and Their Applications in Formation Evaluation: *Journal of Petroleum Technology*, 15, 659–667.

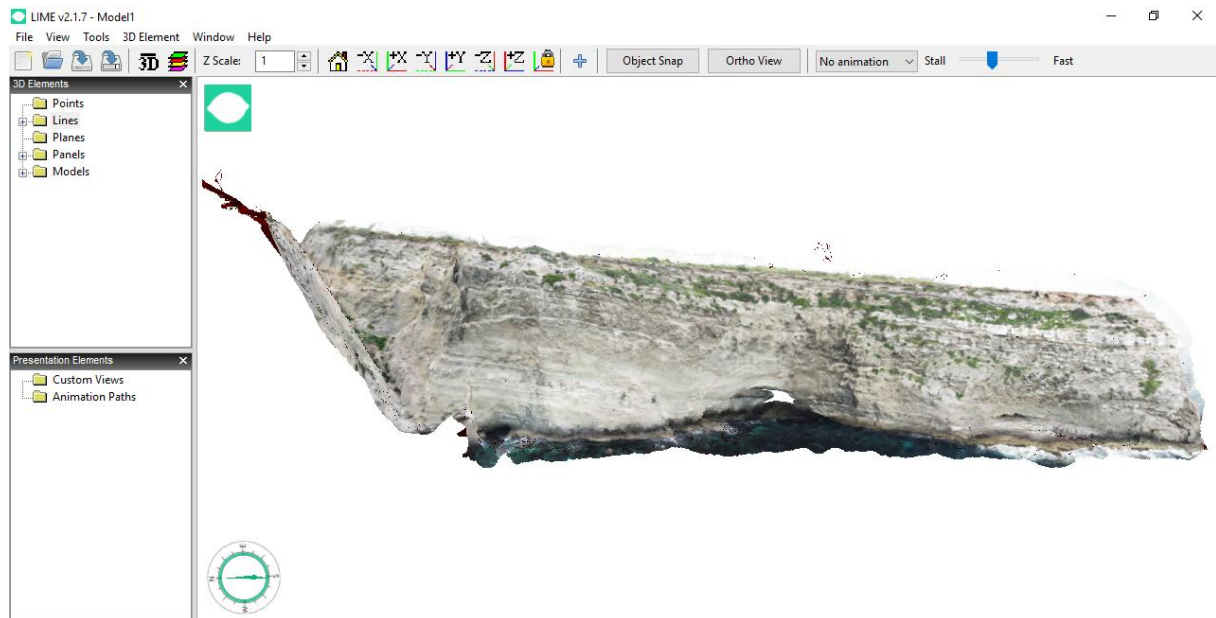
- Planke, S., Eriksen, F.N., Berndt, C., Mienert, J., and Masson, D., 2009, P-Cable high-resolution seismic: *Oceanography*, 22, 85.
- Prestegård, M., 2020, *Controls of fault zone structure on synthetic seismic images of the Maghlaq Fault, Malta*: Master thesis, University of Bergen.
- Pringle, J.K., Howell, J.A., Hodgetts, D., Westerman, A.R., and Hodgson, D.M., 2006, Virtual outcrop models of petroleum reservoir analogues: A review of the current state-of-the-art: *First Break*, 24, 33–42.
- Putz-Perrier, M.W., and Sanderson, D.J., 2010, Distribution of faults and extensional strain in fractured carbonates of the North Malta Graben: *AAPG Bulletin*, 94, 435–456.
- Rabbell, O., Galland, O., Mair, K., Lecomte, I., Senger, K., Spacapan, J.B., and Manceda, R., 2018, From field analogues to realistic seismic modelling: A case study of an oil-producing andesitic sill complex in the Neuquén Basin, Argentina: *Journal of the Geological Society*, 175, 580–593.
- Rafaelsen, B., 2006, Seismic resolution and frequency filtering: *Univ. Tromsø Lecture Series, Tromsø, Norway*.
- Reuther, C.D., 1984, Tectonics of the Maltese Islands: *Centro*, 1, 1-20.
- Reuther, C.D., and Eisbacher, G.H., 1985, Pantelleria Rift - crustal extension in a convergent intraplate setting: *Geologische Rundschau*, 74, 585–597.
- Riley, P.R., Goodwin, L.B., and Lewis, C.J., 2010, Controls on fault damage zone width, structure, and symmetry in the Bandelier Tuff, New Mexico: *Journal of Structural Geology*, 32, 766–780.
- Robertson, A.H.F., and Dixon, J.E., 1984, Introduction: Aspects of the geological evolution of the Eastern Mediterranean: *Geological Society Special Publication*, 17, 1–74.
- Roca, E., and Desegaulx, P., 1992, Analysis of the geological evolution and vertical movements in the València Trough area, western Mediterranean: *Marine and Petroleum Geology*, 9, 167–185.
- Rosenbaum, G., and Lister, G.S., 2002, Reconstruction of the evolution of the Alpine-Himalayan orogen - An introduction: *Journal of the Virtual Explorer*, 8, 1–2.
- Rosenbaum, G., Lister, G.S., and Duboz, C., 2002, Reconstruction of the tectonic evolution of the western Mediterranean since the Oligocene: *Journal of the Virtual Explorer*, 8, 107–130.
- Rotevatn, A., and Fossen, H., 2011, Simulating the effect of subseismic fault tails and process zones in a siliciclastic reservoir analogue: Implications for aquifer support and trap definition: *Marine and Petroleum Geology*, 28, 1648–1662.
- Ryan, H., 1994, Ricker, Ormsby; Klander, Butterworth -A Choice of wavelets.
- Saffarzadeh, S., Javaherian, A., Hasani, H., and Sadri, M., 2019, Seismic modelling and its application on designing the seismic survey parameters, a case study of an Iranian oil field: *Exploration Geophysics*, 50, 75–85.
- Scholz, C.H., and Aviles, C.A., 2013, The Fractal Geometry of Faults and Faulting: *Earthquake source mechanics*, 37, 147–155.
- Sheriff, R.E., 1996, Understanding the Fresnel zone: Search and Discovery article #40014: *Geophysical corner, SEG*.
- Shipton, Z.K., and Cowie, P.A., 2001, Damage zone and slip-surface evolution over μm to km scales in high-porosity Navajo sandstone, Utah: *Journal of Structural Geology*, 23, 1825–1844.
- Shipton, Z.K., and Cowie, P.A., 2003, A conceptual model for the origin of fault damage zone structures in high-porosity sandstone: *Journal of Structural Geology*, 25, 333–344.
- Simm, R., and Bacon, M., 2014, *Seismic Amplitude: An interpreter's handbook*: Cambridge University Press.
- Thore, P.D., and Juliard, C., 1999, Fresnel zone effect on seismic velocity resolution:

- Geophysics*, 64, 593–603.
- Tosaya, C., and Nur, A., 1982, Effects of diagenesis and clays on compressional velocities in rocks: *Geophysical Research Letters*, 9, 5–8.
- Townsend, C., Firth, I.R., Westerman, R., Kirkevollen, L., Hårde, M., and Andersen, T., 1998, Small seismic-scale fault identification and mapping: *Geological Society Special Publication*, 147, 1–25.
- Ursenbach, C.P., 2002, Generalized gardner relations: *72nd Annual International Meeting, SEG, Expanded Abstracts.*, 1885–1888.
- Vinje, V., Lie, J.E., Danielsen, V., Dhelie, P.E., Siliqi, R., Nilsen, C.I., Hicks, E., and Camerer, A., 2017, Shooting over the streamer spread: *First Break*, 35, 97–104.
- Walsh, J.J., and Watterson, J., 1993, Fractal analysis of fracture patterns using the standard box-counting technique: valid and invalid methodologies: *Journal of Structural Geology*, 15, 1509–1512.
- Walsh, J.J., Watterson, J., Heath, A., Gillespie, P.A., and Childs, C., 1998, Assessment of the effects of sub-seismic faults on bulk permeabilities of reservoir sequences: *Geological Society, London, Special Publications*, 127, 99–114.
- Wibberley, C.A.J., Yielding, G., and Di Toro, G., 2008, Recent advances in the understanding of fault zone internal structure: A review: *Geological Society, London, Special Publications*, 299, 5–33.
- Willemsse, E.J.M., Peacock, D.C.P., and Aydin, A., 1997, Nucleation and growth of strike-slip faults in limestones from Somerset, U.K.: *Journal of Structural Geology*, 19, 1461–1477.
- Wrona, T., Fossen, H., Lecomte, I., Eide, C.H., and Gawthorpe, R., 2019, Seismic expression of shear zones: insights from 2-D convolution seismic modelling: doi: 10.31223/osf.io/5ypzg.
- Zhang, R., and Castagna, J., 2011, Seismic sparse-layer reflectivity inversion using basis pursuit decomposition: *Geophysics*, 76, 147–158.

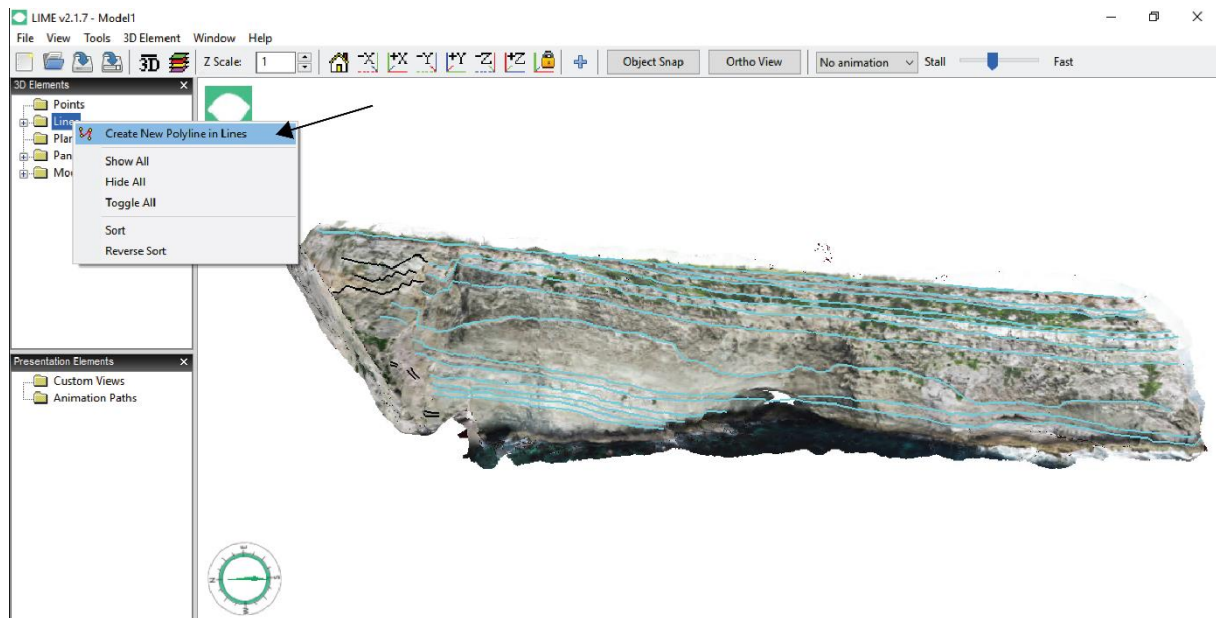
Appendix A

Workflow: from outcrop to 2D synthetic seismic

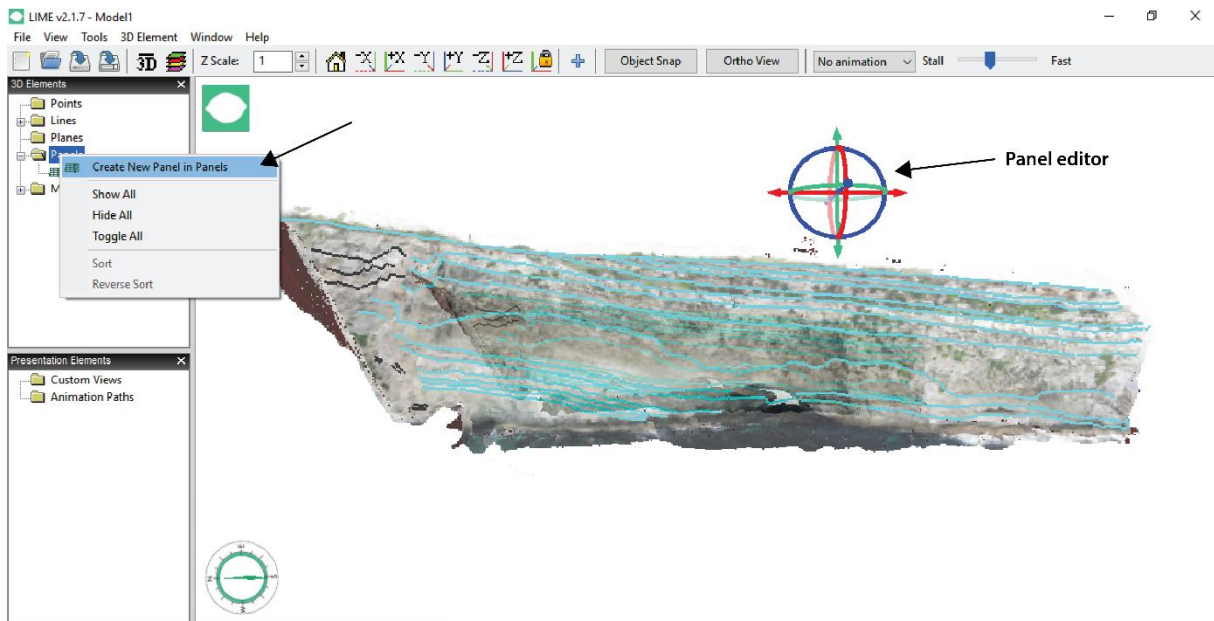
1. Import the 3D virtual outcrop model from AgiSoft Photoscan to LIME.



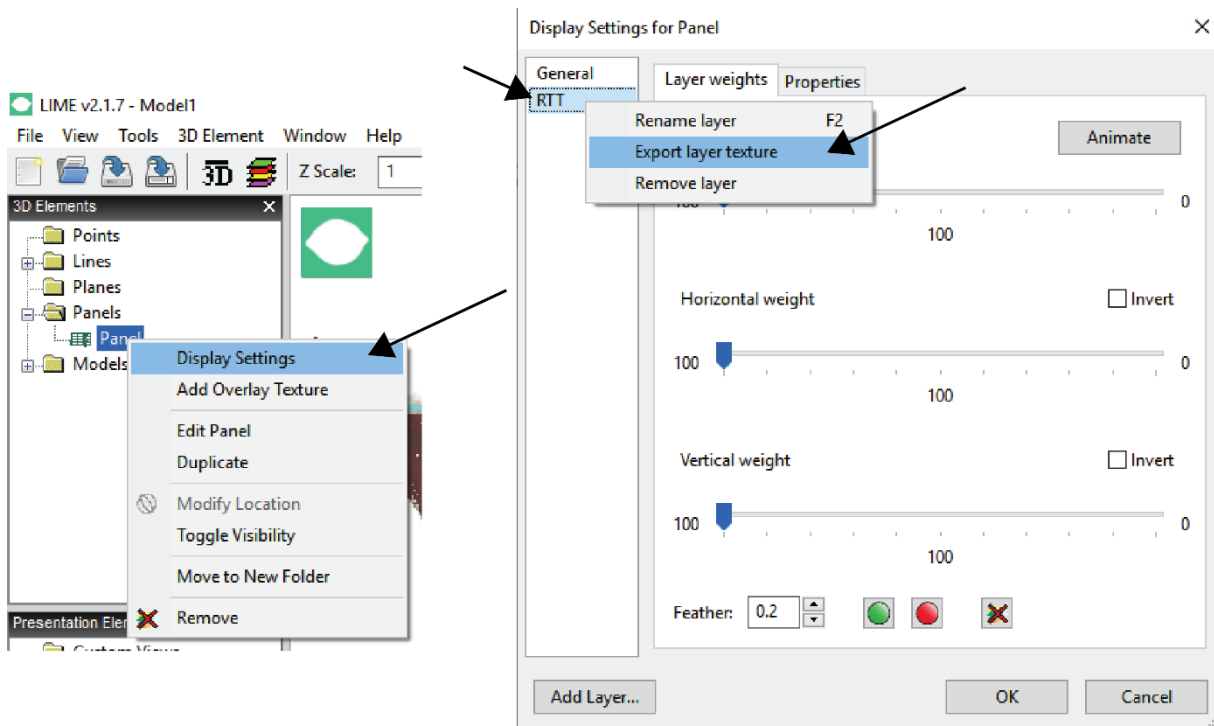
2. Identify and mark the main stratigraphic boundaries and structural features by using the lines tool.



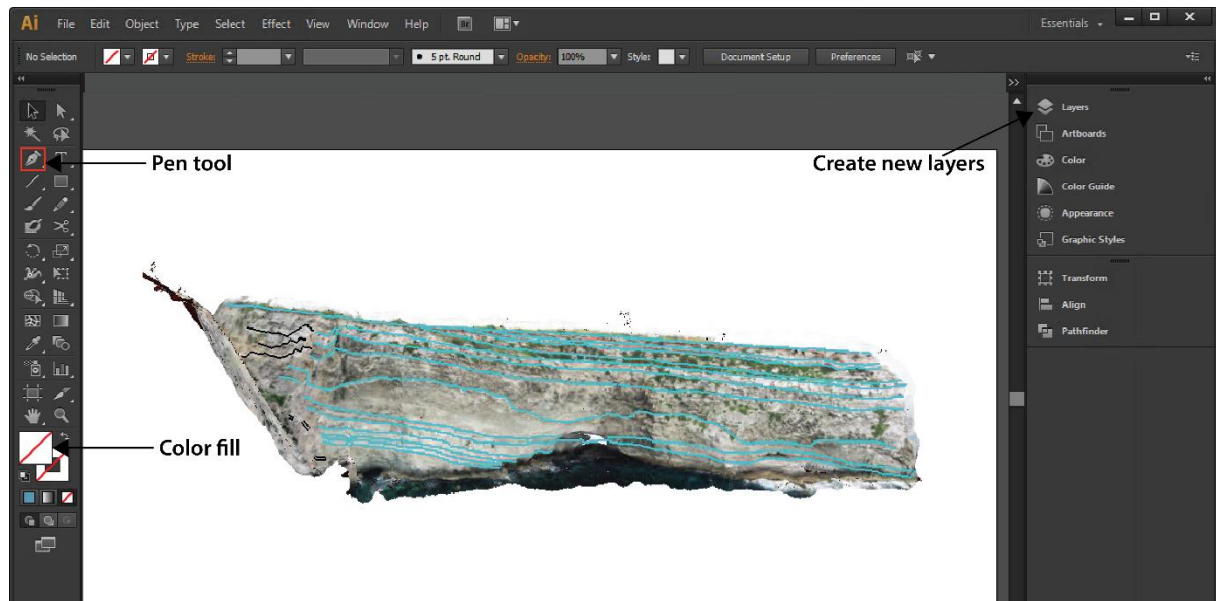
- Project the interpretations onto a 2D panel parallel to the outcrop by using the panels tool.



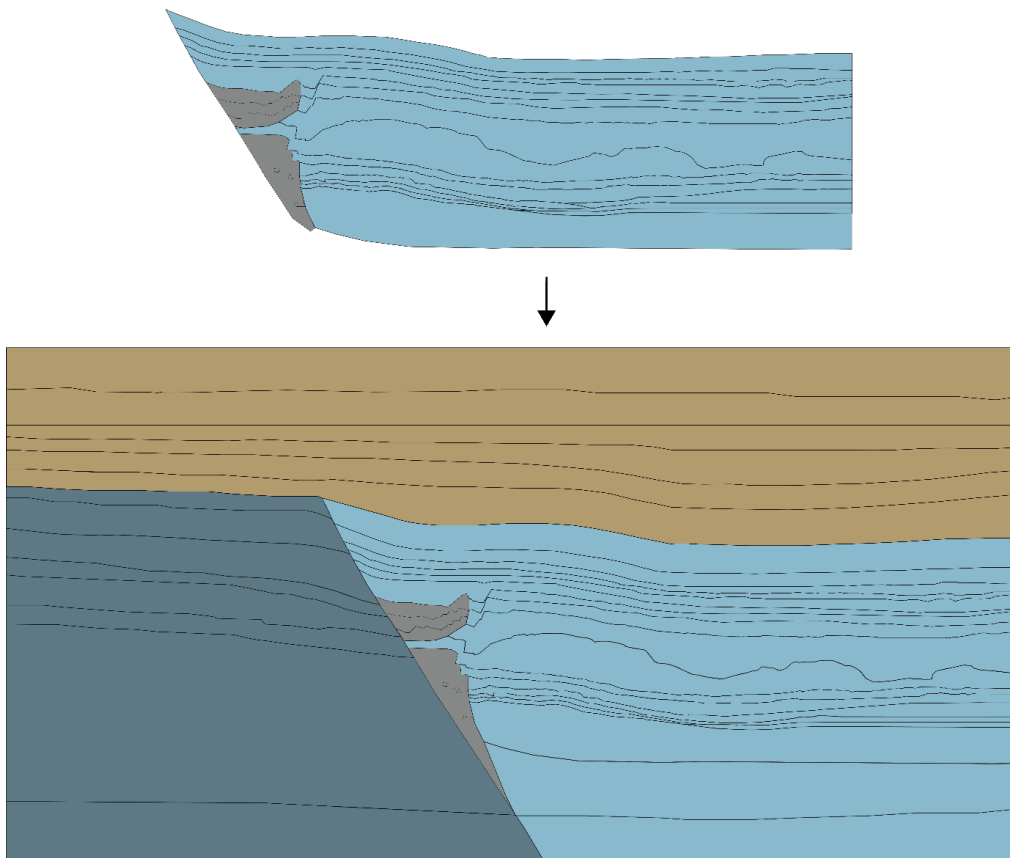
- Export the panel as an image file (.PNG).



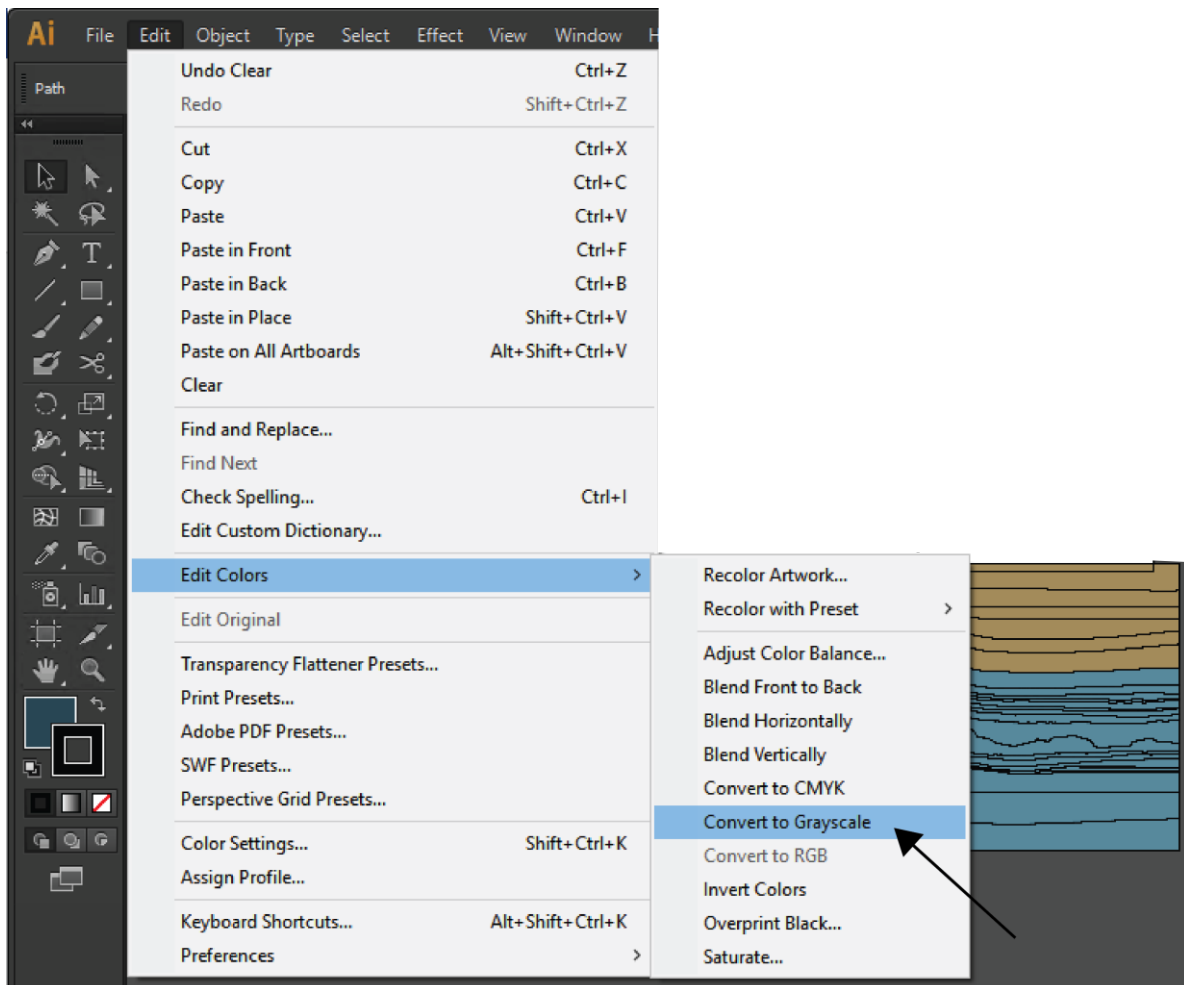
5. Import the 2D panel into a graphics editing software (e.g. Adobe Illustrator).



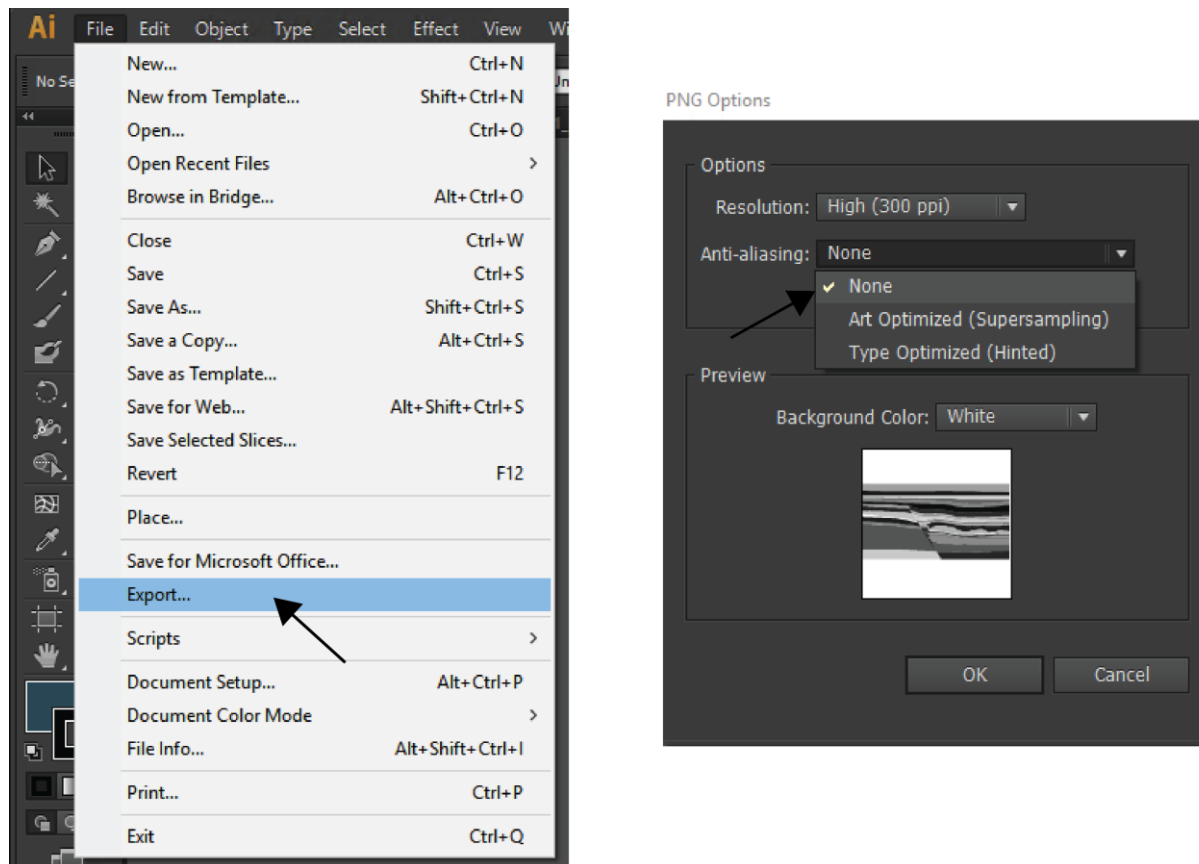
6. Fill each interpreted unit in the model with different colors.
7. Merge the geological model of the footwall with the hanging wall model to create a complete fault zone model.
8. Extrapolate the geological layers with respect to the geometry of the fault and add an over- and underburden in order to form a realistic subsurface model.



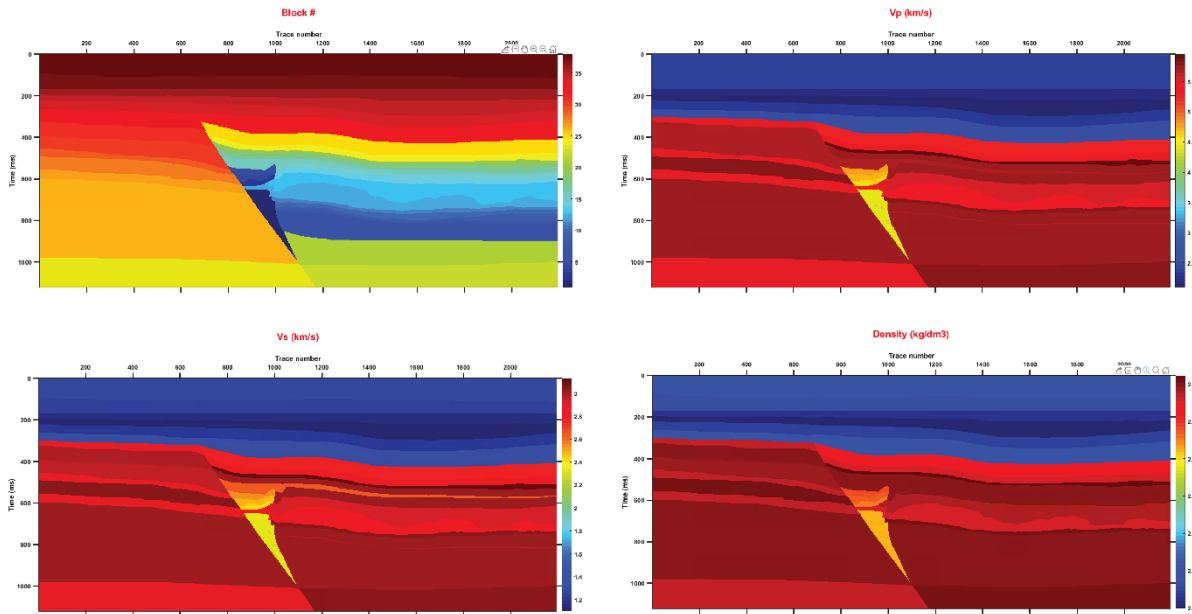
9. Make sure the layer boundaries are sharp with no blank space in between. This is to avoid unidentified colors in the figure that can make the exported model inadequate at a later stage when using Matlab.
10. Convert the model into grey scale colors, which can be mathematically identified by Matlab.



11. Turn off the anti-aliasing function in the drawing software prior to exporting the model as a 32-bit PNG image file.

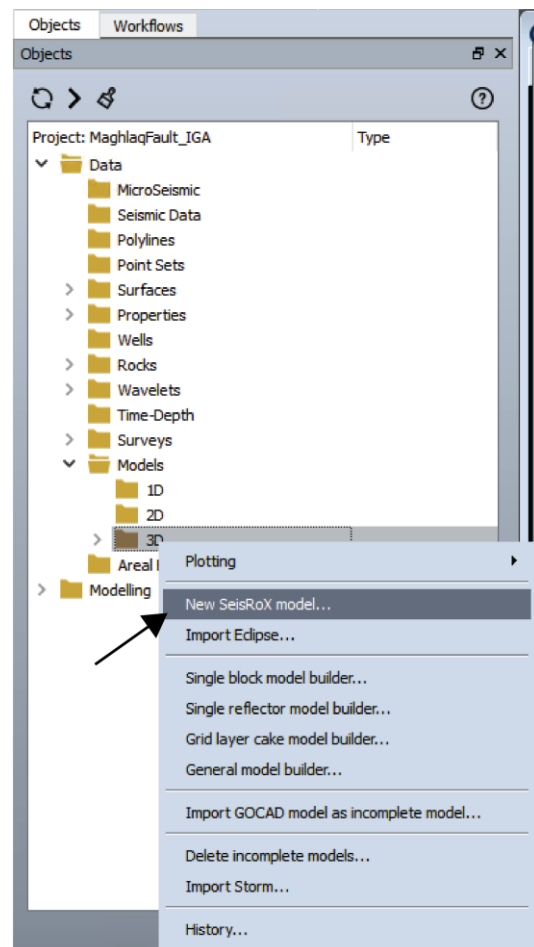
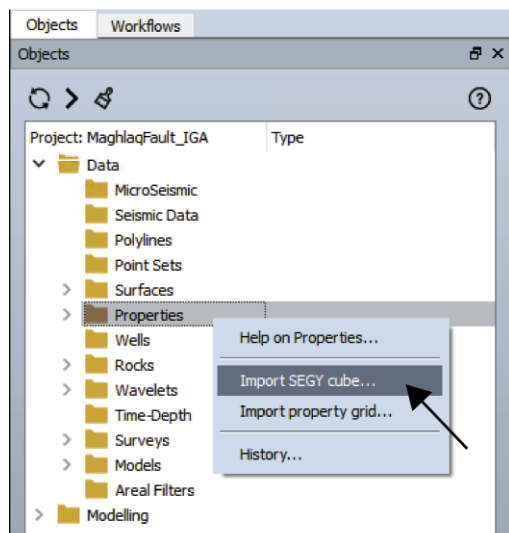


12. Each unit filled with a grey scale color in the 2D model is hereafter referred to as a “block”. The different blocks are assigned elastic properties (V_p , V_s and density), which are needed for generating seismic reflections.
13. Matlab and Seislab 3.02 are used to link the blocks within the geological model to the associated elastic properties. In this process, four SEG-Y-files are created from the PNG-files; “block”, “rho”, “ V_p ” and “ V_s ”, that can be read by SeisRoX Pro – NORSAR Software Suite 2019.

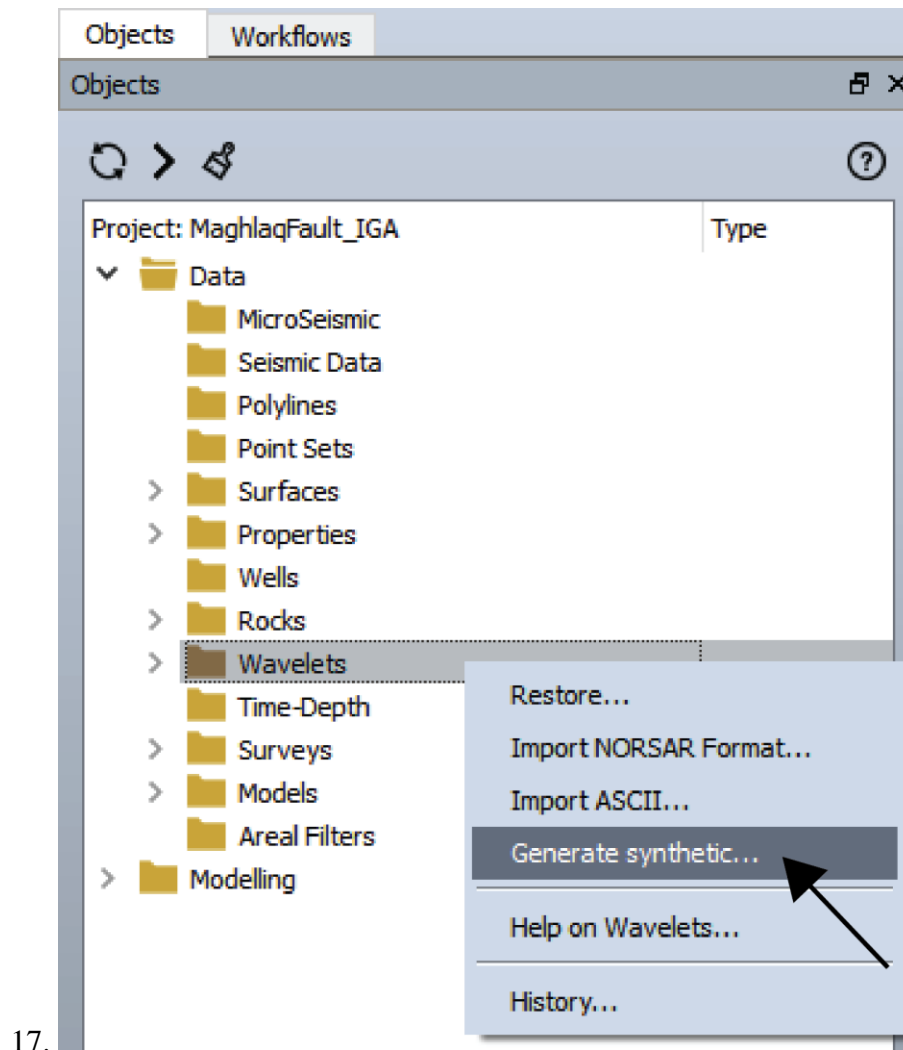


The next steps are performed in SeisRoX:

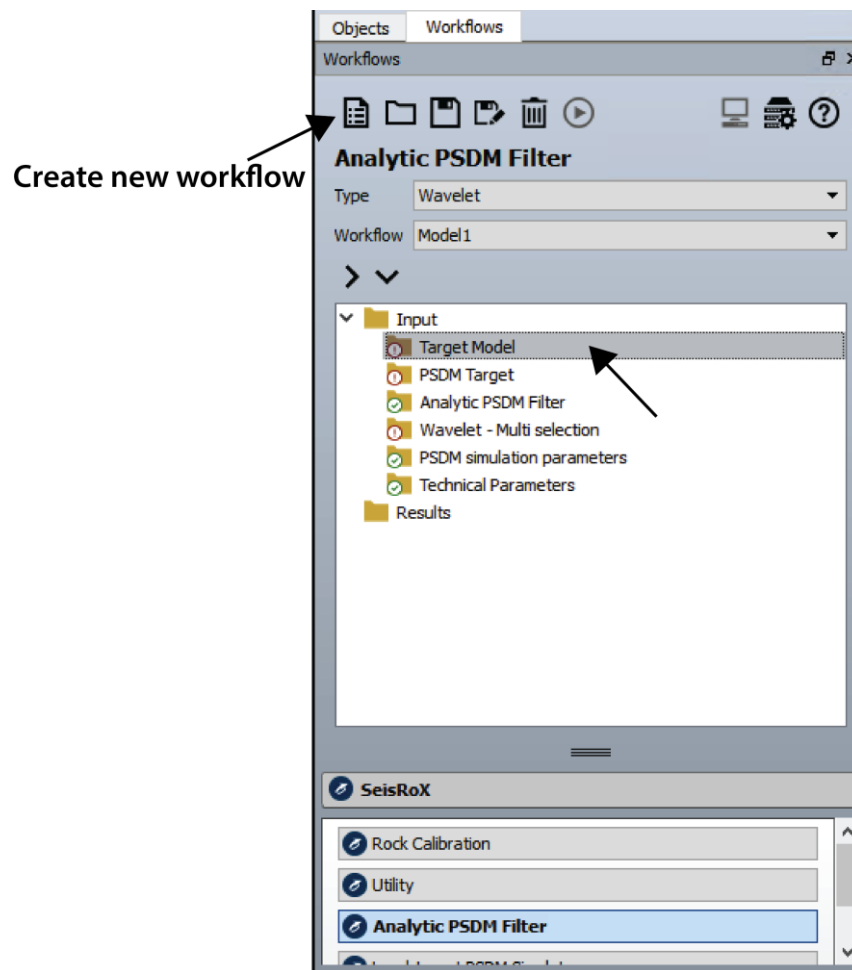
14. Create a new project with a 2D grid size that fits the input model.
15. Import the four SEGY-files to SeisRoX as property cubes in the objects pan and use them to build a 3D target model.



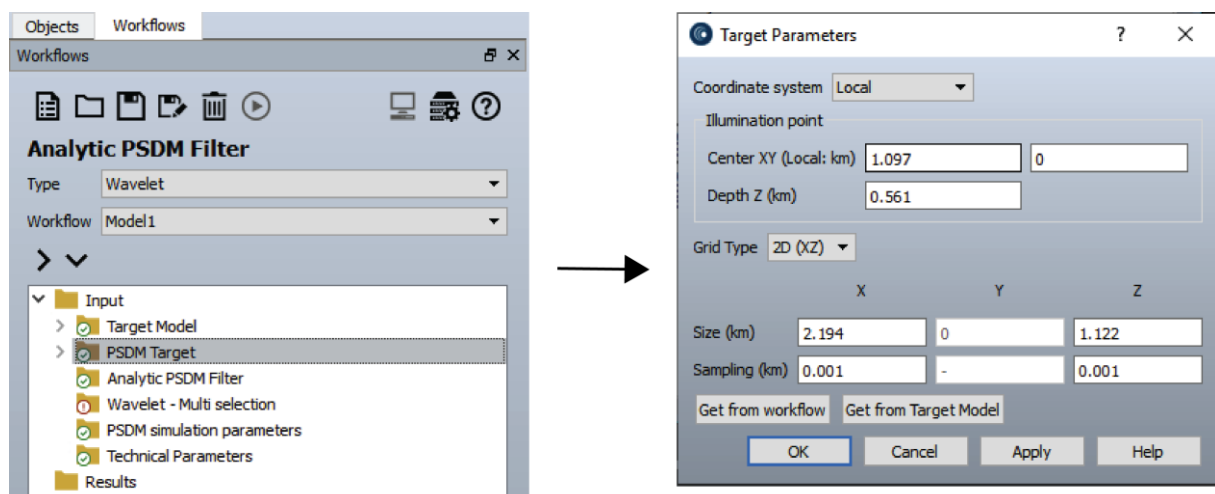
16. Generate synthetic Ricker wavelets of different frequencies. These will be used to simulate synthetic seismic at a later stage in the workflow.



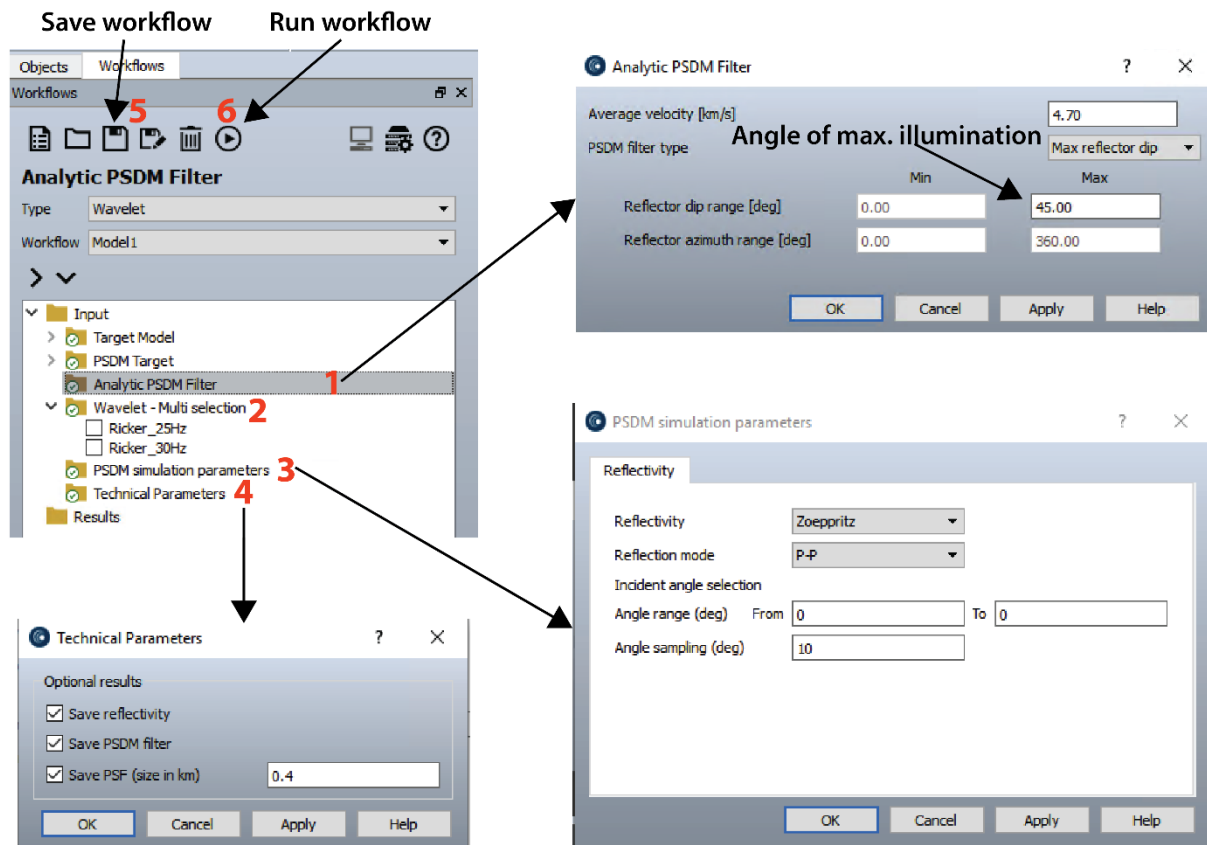
18. Create a PSDM analytical filter in the wavelet workflow in the workflow pan, to allow multi wavelet selection in order to perform modeling with different frequencies.
19. Select the 3D target model created in (15) as the target model for the modeling.



20. Open the Target Parameter settings by double clicking on the PSDM Target. Set the grid type to 2D (XZ), with the center of X and Z at half of the width and length of the target model's size. Y is 0 for the 2D grid. Set the sampling to 0.001 km.



21. Decide values for the average velocity and the angle of maximum illumination within the Analytical PSDM Filter (1).
22. Select one or several wavelets (as generated in 16) under Wavelet – Multi selection (2) and specify the incident angle within the PSDM simulation parameters (3).
23. Toggle on the PSF, the reflectivity and the PSDM filter under Technical Parameters (4) in order to generate the associated parameters with the resulting seismic.
24. Save the workflow (5) and click run (6).



25. View the generated seismic with the associated PSF and the reflectivity model in a 2D viewer.

